

Protein Thermal Stabilization and Delivery via Adsorption onto Porous Silicas

By
© 2022

Nicole Montoya Oyuela

Submitted to the graduate degree program in Chemical and Petroleum Engineering Department
and the Graduate Faculty of the University of Kansas in partial fulfillment of the requirements
for the degree of Master of Science.

Chair: Mark B. Shiflett

David Corbin

Alan Allgeier

Date Defended: 6 May 2022

The thesis committee for Nicole Montoya certifies that this is the approved version of the following thesis:

**Protein Thermal Stabilization and Delivery
via Adsorption onto Porous Silicas**

Chair: Mark B. Shiflett

Date Approved: 6 May 2022

Abstract

The cold chain is a problem that affects the whole pharmaceutical industry: in 2019, 45% of new FDA approved drugs required refrigeration or freezing. It is estimated that biopharma loses around 35 billion dollars every year due to failures in temperature control logistics. Proteins, the main components of vaccines, enzymes and many pharmaceuticals, are sensitive to denaturing and losing their conformational structure when exposed to thermal stress. This is why most pharmaceutical products require a temperature-controlled supply chain to ensure that heat exposure does not disrupt the intermolecular interaction needed to maintain protein structure and activity.

The aim of this study is to develop a more sustainable technology via protein adsorption onto mesoporous silica, in order to improve the protein's thermal stability. Two proteins were investigated: Invasion Plasmid Antigen D (IpaD) and Lactoferrin (Lf). Circular dichroism (CD) confirmed that the adsorbed IpaD and Lf after the heat treatment maintained a native secondary structure rich in α -helical content. In contrast, the unprotected proteins after heat treatment lost their secondary structure. Isotherms modeled using Langmuir, Freundlich and Temkin models demonstrated that the adsorption of IpaD and Lf onto silicas is best fit by the Langmuir model. Silica pore size was determined to be a key factor in protein adsorption. If pores are less than 15 nm, adsorption is negligible. If the pores are between 15-25 nm, then monolayer coverage is achieved and IpaD is protected from thermal denaturing. If pores are larger than 25 nm the adsorption is multilayer coverage and it is easier to remove the protein from the silica due to a less developed hydrogen bond network.

In addition, this work investigates the protein release from silica using non-ionic detergents (Triton X-100, Tween 20, 40 and 80). Lactoferrin desorption tests with non-ionic detergents

showed a trend for increased Lf recovery with increased detergent hydrophobicity. Triton X-100 and Tween 80 were the best detergents for Lf desorption, recovering over 80% of the initial protein. This research provides strong evidence that proteins can be thermally stabilized on mesoporous silica and efficiently released from the silica using non-ionic detergents.

Dedicated to Bella and Esteban for their unconditional loyalty and dedication,

And to my family for their constant love and unwavering support.

Acknowledgments

Above all, thank you Dr. Mark Shiflett, for your mentorship and for always believing I am capable of achieving anything I set my mind to. Thank you for challenging me to push my limits and always having my back every step of the way. I could not have asked for a better advisor. I am also thankful to Dr. David Corbin, Dr. Philip Gao and Dr. Alan Allgeier for their invaluable guidance and support since the very first day.

I am grateful to the entire faculty of the Department of Chemical and Petroleum Engineering at the University of Kansas. Special thanks to Dr. Kevin Leonard, Dr. Susan Williams, Dr. Aaron Scurto, Dr. Stevin Gehrke, Dr. Juan Bravo and Dr. Trung Nguyen. Thank you for sharing your love and passion of chemical engineering with me. This project would not have been possible without the experimental contributions of Kaylee Barr, Rhianna Roth and Elizabeth Funk. Working with you was one of the greatest joys of my time at KU. I would like to recognize Gilbert Ortiz for the design and creation of remarkable graphics for journal cover art. Thank you to my lab mates: Kalin, Abby, Berlyn, Karim, Andrew, Simon, Murillo, Michael, Samir, CJ and Victor, your friendship and support made me walk into work every day with a smile on my face.

Por último, quiero agradecerle a Dios y a mi familia. A mis abuelos: Marta, Nayo, Jorge y Carmen, por su ejemplo de sacrificio, amor y familia. A mis papas, Nelson y Yami, por su amor, cariño y apoyo incondicional. A mis hermanos y primos: Daniel, Sofia, Marito, Isaí, Matilde y Sara por ser mis mejores amigos en este mundo. A mis tías: Irasema, Ana, Nadezda, Alma Delia, Carmen, Lourdes y Jessica, no sería la mujer que soy hoy sin ustedes. A mi tía Mayra: no tengo palabras para agradecer su guía, amor y apoyo en mi vida, gracias por siempre ser mi luz. A Esteban, el amor de mi vida y a Bella, mi alma gemela. Los amo profundamente, este logro es gracias a todos ustedes.

Additional Acknowledgements

Portions of this thesis have been previously published as articles in journals by the American Chemical Society (ACS). The publishers allow the author to reuse published works in the author's thesis which the author writes and is required to submit to satisfy the criteria of degree-granting institutions.

Portions reused from:

1. Montoya, N. A.; Barr, K. E.; Morales, S. V.; Umana, J. E.; Ny, C.; Roth, R. E.; Reyes, E. J.; Kirchhoff, B. C.; Hartman, E. R.; Higgins, L. L., Protein Stabilization and Delivery: A Case Study of Invasion Plasmid Antigen D Adsorbed on Porous Silica. *Langmuir* **2020**.
2. Montoya, N. A.; Roth, R. E.; Funk, E. K.; Gao, P.; Corbin, D. R.; Shiflett, M. B., Review on porous materials for the thermal stabilization of proteins. *Microporous and Mesoporous Materials* **2022**.

Table of Contents

Chapter 1: Introduction	1
1.1 Importance of Protein Thermal Stabilization.....	1
1.2 Review of Inorganic Porous Materials for Protein Immobilization.....	4
1.2.1 Sol-gel Silica.....	5
1.2.2 Porous Silicas.....	9
1.2.3 Porous Activated Carbons.....	13
1.2.4 Aluminum and Iron Oxides	16
1.2.5 Metal Organic Framework.....	19
1.3 Review of Organic Polymer Materials for Protein Immobilization.....	23
1.3.1 Natural Polymers	23
1.3.2 Synthetic Polymers	29
1.4 Primary Objectives.....	30
Chapter 2: Experimental Methods	31
2.1 Materials	31
2.2 IpaD Protein Expression and Purification.....	32
2.3 Physical Characterization.....	33
2.4 Adsorption.....	33
2.5 Heating.....	34
2.6 Desorption.....	34
2.7 TEM Imaging.....	34
2.8 Circular Dichroism Spectropolarimetry.....	35

Chapter 3: Case Study 1-Invasion Plasmid Antigen D (IpaD) Adsorption and Thermal Stabilization	37
3.1 Introduction.....	37
3.2 Physiochemical Characterization.....	38
3.3 Effect of silica pore diameter on IpaD adsorption.....	39
3.4 Langmuir Model Derivation	41
3.5 Langmuir Adsorption Isotherm Modeling.....	42
3.6 Comparing the Langmuir Model to Freundlich and Temkin Models.....	50
3.7 TEM Characterization.....	52
3.8 Desorption.....	55
3.9 IpaD secondary structure	57
3.10 Effect of Silica Size on Equilibrium Constants	63
Chapter 4: Case Study 2-Lactoferrin Thermal Stabilization via Adsorption and Desorption using Non-ionic Detergents	65
4.1 Introduction.....	65
4.2 Adsorption Modeling.....	68
4.3 Lactoferrin Thermal Stability	74
4.4 Desorption Detergents	76
4.5 Lactoferrin Stability in Detergent Solutions.....	78
4.6 Silica and Detergent Interactions	80
Chapter 5: Conclusions and Recommendations	83
5.1 Case Study 1 – IpaD sorption and thermal stabilization on mesoporous silica.....	83
5.2 Case Study 2 - Lf sorption and thermal stabilization on mesoporous silica.....	84

5.3 Recommendations.....	85
References.....	87
Appendix A: TGA Curves of Silica Samples and FTIR of Native IpaD in PBS.....	103
Appendix B: Pore size distributions of silica samples.....	109
Appendix C: Error Calculation on Adsorption Isotherms	114
Appendix D: IpaD Adsorption Isotherms.....	116
Appendix E: Lf Adsorption Isotherms.....	122

List of Figures

Figure 1.1. Classification of porous materials for protein thermal stabilization.....	4
Figure 1.2. Sol-gel silica protein encapsulation (left) vs protein adsorption onto mesoporous silica (right).....	5
Figure 1.3. Protein adsorption onto MOF	20
Figure 3.1. Proposed hydrogen bonds between IpaD residues and mesoporous silica surface ...	38
Figure 3.2. Average percent of IpaD adsorbed to mesoporous silica materials (SA1 to SA7) as a function of average pore diameter (nm).....	40
Figure 3.3 Percent of IpaD adsorbed to silica samples as a function of silica pore volume.....	41
Figure 3.4. Adsorption isotherm for silica sample SA3 using the Langmuir model	43
Figure 3.5. Adsorption isotherms using the Langmuir model for silica gel SA4 (top left), SA5 (top right), SA6 (bottom left) and SA7 (bottom right)	44
Figure 3.6. Linearized adsorption isotherm for silica sample SA3 using the Langmuir model ($R^2=0.994$).....	45
Figure 3.7. IpaD concentration after subsequent washes for sample 1 (triangles), sample 2 (diamonds), sample 3 (squares) and sample 4 (circles). Initial silica masses of samples 1-4 are 8.3 mg, 7.0 mg, 6.3 mg and 3.0 mg, respectively. Initial IpaD concentration is 1.95 mg/mL for all samples, silica is SA7.	47
Figure 3.8. Comparison of the adsorption isotherm for silica sample SA1 (black) and the adsorption isotherm for silica sample SA3 (red). Inset is expanded view of silica sample SA1..	48
Figure 3.9. Adsorption isotherm for silica sample SA2.....	49
Figure 3.10. Comparison of the three types of pores interactions with IpaD, (A) pore size less than 15 nm (e.g. SA1 and SA2), IpaD does not fit into pore, (B) pore size between 15 to 25 nm	

(e.g. SA3, SA4, and SA5), monolayer coverage, hydrogen bonds depicted by solid red line, (C) pore size larger than 25 nm (e.g. SA6 and SA7), multilayer coverage, protein-protein interactions depicted by dotted green line.	50
Figure 3.11. Freundlich adsorption isotherm (left); linearized isotherm for silica sample SA3 using the Freundlich Model ($R^2=0.622$) (right)	51
Figure 3.12. Temkin adsorption isotherm (left); linearized isotherm for silica sample SA3 using the Temkin Model ($R^2=0.856$) (right).....	52
Figure 3.13 A) TEM image for silica sample SA4 as a control to monitor IpaD adsorption; B) TEM image of AuNP average size; C) STEM image of IpaD-AuNP adsorbed in silica sample SA4, blue box is EDX scan location; D) EDX S-K spectral scan of Figure 9C; E) EDX Au-L spectral scan of Figure 9C; F) STEM image of IpaD adsorbed in silica sample SA4; G) STEM image of IpaD in silica sample SA4, blue box is EDX scan location; H) EDX S- K spectral scan of Figure 9G.....	54
Figure 3.14. EDX scan of silica control (SA4)	55
Figure 3.15. EDX scan of IpaD adsorbed on silica SA4.....	55
Figure 3.16. Comparison of adsorption capacity (mg/g) to IpaD released from silica samples during desorption (mg/g) for silica samples SA1-SA7.....	56
Figure 3.17. CD spectra for native unheated IpaD (green), native heated IpaD (red), IpaD removed from silica sample SA4 unheated (black), and IpaD removed from silica sample SA4 (blue) heated to 95 °C for 2 hours.	58
Figure 3.18. CD spectra for heated IpaD on SA3 (blue) and unheated IpaD on SA3 (black).....	58
Figure 3.19. CD spectra for denatured IpaD before (black) and after (red) LDAO addition. LDAO addition does not induce protein refolding	59

Figure 3.20. Comparison of IpaD structure in PBS (blue) and 10% LDAO (green).....	60
Figure 3.21. CD spectra for native IpaD in PBS (green), 10% LDAO (blue), 0.5% LDAO (black) and 3% LDAO (gray)	61
Figure 3.22. CD spectra for native IpaD in LDAO (black) and IpaD adsorbed in silica at room temperature for 6 days (blue).....	62
Figure 3.23. CD spectra for native unheated IpaD (green), native heated IpaD (red), IpaD removed from silica sample SA7 heated to 95 °C for 2 hours (black), and IpaD removed from silica sample SA4 (blue) heated to 95 °C for 2 hours	63
Figure 4.1. Three-dimensional structure of bovine lactoferrin ¹⁸⁵	66
Figure 4.2. Proposed hydrogen bonds between Lf residues and mesoporous silica surface	67
Figure 4.3. Percent of Lf adsorbed to mesoporous silica materials as a function of average pore diameter (nm).....	68
Figure 4.4. Adsorption isotherm of Lf on silica SA5 using the Langmuir model. A decreasing mass of the silica sample results in larger error bars at the highest Lf concentration.	69
Figure 4.5. Linearized adsorption isotherm for Lf on silica SA5 using the Langmuir model (R ² =0.99).....	70
Figure 4.6. Adsorption isotherm for Lf on silica sample SA5 using Langmuir model. Inset is expanded view of silica sample SA1 for comparison.....	72
Figure 4.7. Comparison of the three types of pore interactions with Lf, (A) pore size is too small and Lf does not fit into the pore, (B) pore size is just right “Goldilocks Effect”, monolayer coverage, hydrogen bonds depicted by solid lines, (C) pore size is too large, multilayer coverage, van der Waals forces depicted by dotted lines.....	73

Figure 4.8. Freundlich adsorption isotherm (left); linearized isotherm for silica sample SA5 using the Freundlich Model ($R^2=0.93$) (right)	74
Figure 4.9 Temkin adsorption isotherm (left); linearized isotherm for silica SA5 using the Temkin Model ($R^2=0.98$) (right).....	74
Figure 4.10. CD spectra for native unheated Lf (solid), native heated Lf (dotted), unheated Lf desorbed from silica SA5 (dashed-dotted), and heated Lf desorbed from silica SA5 (dashed). Heat treatment was at 90 °C for 90 min.....	75
Figure 4.11. Recovery (wt%) of Lf from SA5 at various concentrations (0 to 3 vol%) for Tween 20 (circles), Tween 40 (triangles), Tween 80 (diamonds) and Triton X-100 (squares).	77
Figure 4.12. CD Spectra for native Lf in 1XPBS (solid), Lf in 3% Tween 80 (dashed), Lf in 3% Tween 20 (dotted), and Lf in 1% Triton X-100 (dashed-dotted).....	79
Figure 4.13. UV-Vis spectra for lactoferrin (black), Triton X-100 (red) and Tween 80 (blue) ..	80
Figure 4.14. Triton X-100 (1.0 vol%) adsorption (wt%) on silicas SA1, SA3-SA5, SA8-10.....	81
Figure 5.1. Proposed final product concept	86
Figure A.1. TGA curves of weight % (black) and derivative weight (blue) for silica sample SA1	103
Figure A.2. TGA curves of weight % (black) and derivative weight (blue) for silica sample SA2	103
Figure A.3. TGA curves of weight % (black) and derivative weight (blue) for silica sample SA3	104
Figure A.4. TGA curves of weight % (black) and derivative weight (blue) for silica sample SA4	104

Figure A.5. TGA curves of weight % (black) and derivative weight (blue) for silica sample SA5	105
Figure A.6. TGA curves of weight % (black) and derivative weight (blue) for silica sample SA6	105
Figure A.7. TGA curves of weight % (black) and derivative weight (blue) for silica sample SA7	106
Figure A.8. TGA curves of weight % (black) and derivative weight (blue) for silica sample SA8	106
Figure A.9. TGA curves of weight % (black) and derivative weight (blue) for silica sample SA9	107
Figure A.10. TGA curves of weight % (black) and derivative weight (blue) for silica sample SA10	107
Figure A.11. FTIR spectra for IpaD dissolved in PBS (black) and PBS (blue). The most notable peak can be observed at 1653 cm^{-1} corresponding to the alpha helix content in the protein.....	108
Figure B.1. Pore size distribution for silica sample SA1	109
Figure B.2. Pore size distribution for silica sample SA2	109
Figure B.3. Pore size distribution for silica sample SA3	110
Figure B.4. Pore size distribution for silica sample SA4	110
Figure B.5. Pore size distribution for silica sample SA5	111
Figure B.6. Pore size distribution for silica sample SA6	111
Figure B.7. Pore size distribution for silica sample SA7	112
Figure B.8. Pore size distribution for silica sample SA8	112

Figure B.9. Pore size distribution for silica sample SA9	113
Figure B.10. Pore size distribution for silica sample SA10	113
Figure D.1. Linearized adsorption isotherm for silica sample SA4 using the Langmuir model ($R^2=0.992$).....	116
Figure D.2. Linearized isotherm for silica sample SA4 using the Freundlich Model ($R^2=0.365$)	116
Figure D.3. Linearized isotherm for silica sample SA4 using the Temkin Model ($R^2=0.297$) .	117
Figure D.4. Linearized adsorption isotherm for silica sample SA5 using the Langmuir model ($R^2=0.991$).....	117
Figure D.5. Linearized isotherm for silica sample SA5 using the Freundlich Model ($R^2=0.908$)	118
Figure D.6. Linearized isotherm for silica sample SA5 using the Temkin Model ($R^2=0.845$) .	118
Figure D.7. Linearized adsorption isotherm for silica sample SA6 using the Langmuir model ($R^2=0.982$).....	119
Figure D.8. Linearized isotherm for silica sample SA6 using the Freundlich Model ($R^2=0.975$)	119
Figure D.9. Linearized isotherm for silica sample SA6 using the Temkin Model ($R^2=0.973$) .	120
Figure D.10. Linearized adsorption isotherm for silica sample SA7 using the Langmuir model ($R^2=0.824$).....	120
Figure D.11. Linearized isotherm for silica sample SA7 using the Freundlich Model ($R^2=0.821$)	121

Figure D. 12. Linearized isotherm for silica sample SA7 using the Temkin Model ($R^2=0.750$)	121
Figure E.1. Adsorption isotherm of Lf on silica SA7 using the Langmuir model.....	122
Figure E.2. Linearized adsorption isotherm for silica sample SA7 using the Langmuir model ($R^2=0.98$).....	122

List of Tables

Table 1.1. Studies of protein thermal stability in sol-gel material	7
Table 1.2. Studies of protein thermal stability adsorbed onto mesoporous silica (MPS) materials	10
Table 1.3 Studies of protein thermal stability adsorbed onto porous activated carbon materials	14
Table 1.4. Studies of protein thermal stability adsorbed onto porous aluminum oxide metals ...	17
Table 1.5. Studies of protein thermal stability on Metal Organic Framework.....	20
Table 1.6. Studies of protein thermal stability on natural polymers	24
Table 1.7. Studies of thermal stability on synthetic polymers	29
Table 3.1. BJH physicochemical characterization of selected mesoporous silica materials (Samples SA1- SA10). Pore size distributions can be found in Appendix B.	39
Table 3.2. Comparing nitrogen BJH surface area and Langmuir modeling IpaD surface area for silica samples SA3-SA5.....	45
Table 3.3. Comparing nitrogen BJH surface area and pore volume to Langmuir modeling IpaD surface area and pore volume for silica samples SA6 and SA7. Langmuir plots for silica samples SA6 and SA7 are provided in Appendix D.....	46
Table 3.4. Effect of pore size on protein adsorption equilibrium constant	64
Table 4.1. Nitrogen BJH surface area (N_2 -SA) and pore volume (N_2 -PV) compared with Lf surface area (Lf-SA) and pore volume (Lf-PV) calculated using the Langmuir model for silica sample SA7. Langmuir plots for SA6 are provided in Appendix E.	71
Table 4.2. Detergent hydrophile-lipophile balance values ^{205, 206}	78

Chapter 1: Introduction

1.1 Importance of Protein Thermal Stabilization

Combined, the global protein therapeutics and enzyme market are valued at \$149 billion.^{1, 2} In 2019, the global vaccine market was \$46.88 billion, and it is projected to increase up to \$104.87 billion by 2027.³ The Covid-19 pandemic is one of the key reasons for the significant increase in the forecasted vaccine market value since the Covid-19 vaccine market alone is estimated to be worth \$25 billion by 2024.⁴ Protein therapeutics, enzymes, and vaccines are all made up of proteins and these three industries have a common problem: most proteins are subject to denaturing if exposed to high temperatures. The efficiency of protein therapeutics, enzymes, and vaccines is highly dependent on protein secondary and tertiary structure and heat exposure disrupts the intermolecular interactions needed to maintain structure.

Every year, between 2 and 3 million lives are saved because of global immunization practices.⁵ National immunization programs, however, face delivery challenges due to necessary cold chain storage requirements. According to the World Health Organization (WHO), the vaccine cold chain consists of transporting and storing vaccines at the correct temperature (generally 2-8 °C) from manufacturing to delivery site.⁶ Some of the primary issues that limit cold chain performance are: (1) inadequate cold chain capacity, (2) lack of functioning cold chain equipment, and (3) poor vaccine temperature monitoring and maintenance systems. In low-income and lower-middle income countries only 2% of all cold chain equipment is utilizing optimal technology. Furthermore, 14% of all cold chain equipment is completely non-functional and 41% is not operating properly.⁷ Even when the cold chain equipment is functional, the required maintenance is not always performed.⁸

One of the most important risks associated with poorly operating equipment is the possibility of freezing and damaging the stored vaccines. GAVI (Global Alliance for Vaccines and Immunizations) is a public-private global partnership that seeks to increase access to immunization by supporting the governments of low-income countries. In large part due to GAVI's efforts, over 80% of infants around the world receive at least three doses of routine infant vaccines.⁸ The total annual cost for immunization in GAVI-supported countries is estimated to reach \$4 billion in 2020.⁹ If a technique were available to thermally stabilize vaccines without substantially increasing the cost of manufacturing, the annual immunization cost could be reduced by \$125-150 million.⁹

More than 500 commercial products are synthesized using enzymes¹⁰ because of their valuable properties such as low toxicity, high substrate specificity, and fast and effective activity at low concentrations.¹¹ Enzymes are used in a wide range of processes, including detergent, agricultural, food, pharmaceutical, and cosmetic industries.¹¹ Most animal-based enzymes denature at temperatures above 40 °C and must be stored at even lower temperatures than vaccines, between -20 °C to -80 °C.¹²

Protein pharmaceuticals have become much more common in the past few decades. By the late 1980s, only three protein therapeutics existed in the market (including human insulin). Currently, there are over 150 approved protein-based pharmaceuticals.¹³ Most small chemical drugs are taken orally; however, protein instability is one of the main reasons why protein pharmaceuticals are usually administered through injection.¹⁴ Protein therapeutics are sensitive to thermal denaturation since the loss of secondary and/or tertiary structure may cause a decrease in protein activity and elicit an undesired immune response. Furthermore, in most cases, thermal denaturation is irreversible since the unfolded proteins can rapidly aggregate.¹³

Lyophilization of proteins is currently the primary commercial method to maintain protein structure while reducing the need of a cold chain. The lyophilization process involves two main steps: freezing the protein in solution and then drying the frozen protein under vacuum.¹⁴ Although, many proteins are able to retain their structure and activity during both freezing and drying, some proteins are unable to tolerate freezing and drying to different degrees. Many enzymes (lactate dehydrogenase, β -galactosidase, L-asparaginase, and phosphofructokinase), proteins (recombinant hemoglobin), and monoclonal antibodies lose some if not all of their activity during the lyophilization process.¹⁴ Furthermore, lyophilized vaccines are still sensitive to heat exposure. For example, measles vaccines can only tolerate exposure to 40 °C for 2 days and exposure to 37 °C for six days.¹⁵ In addition, lyophilized vaccines after reconstitution must be administered immediately. Because of all the limitations of lyophilization, the enzyme, protein-therapeutics, and vaccine industries are interested in finding alternative ways to thermally stabilize proteins.

Protein immobilization is an attractive alternative to lyophilization. Physical immobilization consists of adsorbing or encapsulating a protein within a support material to lock it in place (via hydrogen bonding, van der Waals interactions, and in some cases covalent bonding) in order to protect the protein's structure from denaturing when exposed to thermal stress. Classification of porous materials for protein stabilization are shown in Figure 1.1. Two of the most common techniques for protein immobilization are sol-gel encapsulation and adsorption onto inorganic porous materials (e.g., silica, activated carbon, aluminum oxide, iron oxide, and metal organic frameworks). Similarly, porous polymers (natural and organic) can be used to covalently or ionically immobilize proteins.

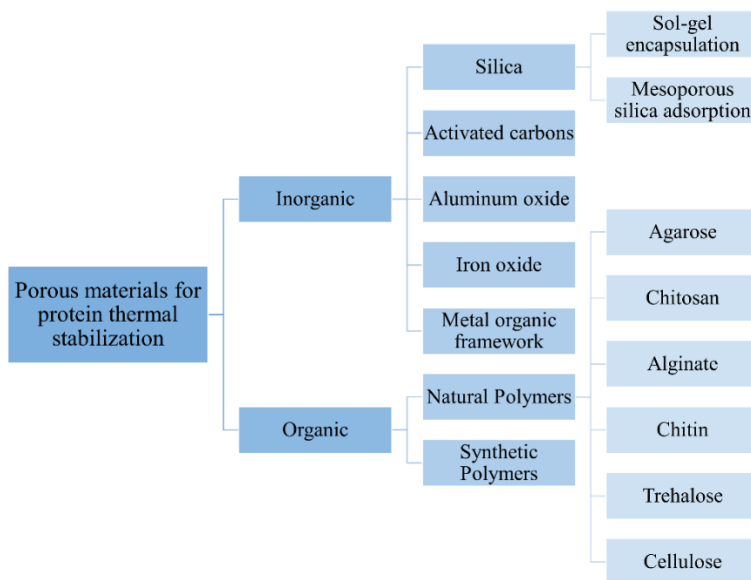


Figure 1.1. Classification of porous materials for protein thermal stabilization

Physical immobilization of enzymes has a key advantage in comparison to the immobilization of vaccines and protein pharmaceuticals. Once enzymes are bound to their support, there may be no need to desorb or separate them from said support. Enzymes can still catalyze reactions while adsorbed on porous materials. However, since vaccines and protein therapeutics are intended to be administered *in vivo*, the reagent may have to be desorbed, released, and separated from the stabilization support. Protein desorption is challenging and only a few groups have successfully reported releasing proteins from the stabilization supports without damaging the protein structure.

1.2 Review of Inorganic Porous Materials for Protein Immobilization

According to the IUPAC denomination, mesoporous materials are materials with pore sizes between 2-50 nm in diameter.¹⁶ Microporous materials have pores smaller than 2 nm in diameter, and macroporous materials have pores larger than 50 nm in diameter. Mesoporous materials have the optimal pore size range for protein adsorption; however, macroporous materials with larger pore sizes may be necessary for vaccine immobilization since vaccines are usually composed of

multiple proteins, surfactants, and additives. Some of the most common types of mesoporous materials for protein stabilization are mesoporous silicas, activated carbons, and aluminum oxides. Regarding mesoporous silicas, two routes are possible: sol-gel protein encapsulation and protein adsorption onto mesoporous silicas as shown in Figure 1.2. Sol-gel chemistry is the typical method to synthesize mesoporous silicas, using surfactant molecules as a template. The condensation of a hydrolyzed silica precursor around the surfactant molecules forms the mesoporous silica network.¹⁶ The surfactant is then removed, resulting in the desired mesoporous silica material. After the mesoporous silica has been synthesized protein is adsorbed (protein adsorption onto mesoporous silica). However, it is possible to use proteins instead of surfactants in the sol-gel process to create a silica network directly around the protein (silica sol-gel protein encapsulation).

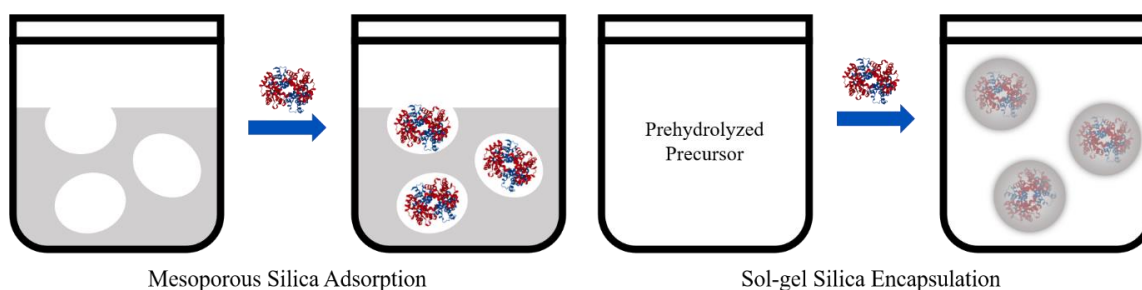


Figure 1.2. Sol-gel silica protein encapsulation (left) vs protein adsorption onto mesoporous silica (right)

1.2.1 Sol-gel Silica

Sol-gel silica is a porous and amorphous material that is synthesized at low temperatures and mild pHs.¹⁷ The sol-gel encapsulation process begins with hydrolysis and condensation reactions of a precursor to form an aqueous sol.¹⁸ The precursors usually involve tetraalkoxysilanes, tri-alkyl alkoxy silanes, di-alkyl alkoxy silanes, or mono-alkyl alkoxy silanes. Two of the most common sol precursors are tetraethyl orthosilicate (TEOS) and tetramethyl orthosilicate (TMOS). Once the precursor is hydrolyzed, it is mixed with an aqueous protein solution that also contains additives,

catalysts, polymers, and templating agents. A polymerization reaction begins the gelation of the sol and consequently encapsulates the protein.

It is possible to modify the surface structure in order to improve protein-sol interactions. A transesterification reaction with glycerol additives can follow the hydrolyzation reaction in order to produce poly(glyceryl silicates), a more biocompatible alternative in comparison to alkoxysilanes.¹⁹ To manipulate more extensive material characteristics, organically modified silanes can be added to TEOS or TMOS based precursors resulting in the ability to change ionic, hydrogen bonding, hydrophilic, and hydrophobic material properties.²⁰

The possibility of surface modification is just one of the major advantages to the sol-gel entrapment technique. Sol-gel derived silicate materials also have a tunable pore size, which can enable a range of different sized proteins to be ensilicated and thermally stabilized. Furthermore, the sol-gel encapsulated protein can be used to develop biosensors since the sol-gel silicates can be made optically transparent.

The first attempt at a sol-gel protein entrapment procedure was published in 1955;²¹ however, it was not until the 1990s when two groups (Avnir²² and Zink²³) began widely using the procedure did the method become established. Over 50 different proteins and enzymes have been successfully immobilized using the sol-gel method.¹⁸ Table 1.1 summarizes the studies that have tested protein thermal stability in sol-gel materials.

The studies shown in Table 1.1 achieve different degrees of thermal stability. In some cases, protein in sol-gel denatured at an average of 10-15°C higher than the unprotected protein,^{17, 24, 25} indicating an improvement in thermal stability, but not full stability at higher temperatures. One of the possible causes for loss of protein structure in gel-embedded proteins may be trace amounts

of alcohol in the sol-gel. Siloxane condensation forms alcohol and even though multiple washes are typically performed, it is possible trace amounts remain in the gel.¹⁷

Table 1.1. Studies of protein thermal stability in sol-gel material

Biomolecule	Sol Precursor/ Desorbing Agent	Thermal Stability	Reference
α -chymotrypsin	TEOS + sarcosine or sorbitol / No desorption	Thermal stability of encapsulated enzyme does not improve unless additives are added. Thermal stability (CD melt) increases only as concentration of sarcosine increases (sorbitol has no effect).	25
α -lactalbumin	TMOS / No desorption	Encapsulated α -lactalbumin did not denature after heating to 95 °C, unprotected protein denatured approximately at 70 °C (CD melt).	24
Ag85b antigen	TEOS / NaF	Some sign of degradation after heating to 95 °C for 2 h but ensilicated sample retained its structure better than free sample.	26
Avidin	TMOS / natural release through diffusion and erosion	Encapsulated avidin unfolds at a moderate less extent than unprotected protein (CD melt).	17
Bovine serum albumin (BSA)	TMOS / natural release through diffusion and erosion	Encapsulated BSA unfolds at a significantly less extent than unprotected protein (CD melt).	17
Hemoglobin	TEOS / NaF	Secondary structure (CD) is conserved after heating to 100°C for 2 h.	27
Hemoglobin	TMOS / PEG	95% of hemoglobin retained native structure at room temperature for 33 days (unprotected hemoglobin denatured).	28
Lysozyme	TMOS / No desorption	Encapsulated lysozyme unfolds at a less extent than unprotected protein (CD melt).	24
Lysozyme	TEOS / NaF	75-100% activity was retained after heating to 100 °C for 5 hr (lysozyme activity assay). 3-year storage at room temperature does not affect protein stability (ELISA).	27 29
Sbi-III-IV-Ag85b vaccine conjugate	TEOS / NaF	Majority of functional activity is retained after heating to 95 °C for 2 h.	26
Tetanus toxin C fragment (TTCF)	TEOS / NaF	Antigen binding capacity (ELISA) and secondary structure (CD) was unaffected after heating to 80 °C for 2 h. In vivo study: mice injected with ensilicated, heated and released TTCF showed same immune response as mice injected with native TTCF.	27 30
Ribonuclease-A	TMOS / natural release through diffusion and erosion	Encapsulated ribonuclease-A unfolds at a slightly less extent than unprotected protein (CD melt).	17
RNAase T1	TEOS + sarcosine or sorbitol / No desorption	Thermal stability of encapsulated enzyme does not improve unless additives are added. Thermal stability (CD melt) increases as concentration of sarcosine and sorbitol increases.	25

It is important to note that these three studies were published in the early 2000s and more recent studies have shown continued success achieving an increased degree of thermal stability. The group of van den Elsen and coworkers have made the most contributions to the sol-gel biomolecule immobilization field in the past decade.^{26, 27, 29, 30} The group proved that lysozyme, hemoglobin, TTCF, and Sbi-III-IV-Ag85b vaccine conjugate are able to retain structural stability after exposure to extreme heat stress (100 °C for lysozyme and hemoglobin, 80 °C for TTCF, and 95 °C for Sbi-III-IV-Ag85b vaccine conjugate).

The group also was the first to conduct *in vivo* experiments, injecting mice with native TTCF, ensilicated and released TTCF, and ensilicated, heated (80 °C), and released TTCF.³⁰ The results from this study are extremely promising: the anti-TTCF IgG immune response as (evidenced by ELISA) of mice injected with the ensilicated and released TTCF or the ensilicated, heated, and released TTCF was consistent with the immune response of the mice injected with native TTCF.³⁰ Dilute sodium fluoride was used by van den Elsen et al. to desorb the proteins from the sol-gel matrix. The optimal pH of 4.0 was determined where protein activity was still intact during the desorption process; however, alternative release protocols would be necessary for a biological application. A important issue is the fluoride in solution is toxic, resulting in gastrointestinal distress at doses between 100-150 mg.³¹

Clearly, the release of proteins from sol-gels is a critical issue that makes the process difficult to adapt in clinical conditions. Most sol-gel procedures use a high concentration of silica precursor, between 30-50% that is the primary reason protein desorption is so complicated. Recently, Boylan and coworkers developed a new sol-gel route where a protein solution is exposed to TMOS vapors.²⁸ The TMOS hydrolyzes and then diffuses into the aqueous protein solution, encapsulating the protein.²⁸ This new sol-gel route allows for much lower concentrations of silica precursor

(TMOS) to be used. By using a 1% TMOS sol-gel it is possible to use polyethylene glycol (PEG) to recover up to 91% hemoglobin protein. However, in order to conserve hemoglobin's native structure during heating protocols, a 5% concentration of TMOS is necessary. This method has great potential for clinical applications, but an optimal TMOS concentration has to be determined in order to maximize both protein recovery and thermal stability.

1.2.2 Porous Silicas

Porous silicas have demonstrated the ability to retain protein structure and functionality.^{27, 32} Some of the most relevant advantages of using silica for protein adsorption include: (1) high thermal stability, (2) useful porosity range for proteins, (3) simple chemistry, (4) mild pH, (5) tunable surface chemistry, and (6) encapsulated biomolecular samples that retain high activity. Furthermore, it is possible to create a customized mesoporous silica material for any desired protein by tuning the pore size, pore shape, and silica surface chemistry.

Protein amino acids are able to attach to the surface of the silica via hydrogen bonding, van der Waals interactions, and electrostatic interactions;³³ therefore, it is possible to adsorb biomolecules using silicas and lock the protein into place for increasing thermal stability. Even though silicas are "Generally Recognized as Safe" (GRAS) by the FDA,³⁴ the silica-immobilized vaccines or protein therapeutics would be desorbed from the silica prior to patient administration using a drug delivery device. In some cases for orally administered vaccines, the mass of silica for each administered dose would be <5 mg and negligible in comparison to the reported toxic dose for silica of 500 mg/kg.³⁵

The first solid mesoporous silicas were first synthesized in 1992 by Mobil Research and Development Corporation and were named MCM-41 (Mobil Crystalline Materials or Mobil

Composition of Matter).¹⁶ MCM silicas have pore diameters ranging between 2.5 to 6 nm. The University of California, Santa Barbara was the second to synthesize a solid mesoporous silica, calling their material Santa Barbara Amorphous type material (SBA). SBA silicas have larger pore sizes, between 4.6 to 30 nm, and are extremely ordered with thicker silica walls.³⁶ Another type of mesoporous silica is the folded sheet mesoporous material (FSM), which uses a quaternary ammonium surfactant for the template and layered polysilicate kanemite for its synthesis.¹⁶ MCM and SBA silica types are highly organized and have a fairly uniform pore size. However, many mesoporous silica materials (MPS) have a range of pore sizes, from micro to mesopores. For protein adsorption onto mesoporous silica research, it is possible to commercially purchase a wide array of mesoporous silicas or to synthesize it if there is not a silica commercially available for a specific protein. More than 30 proteins including small protein therapeutics and enzymes have been immobilized on mesoporous silicas.¹⁶ Table 1.2 summarizes only the studies that have tested protein thermal stability in mesoporous silica (MPS) materials.

Table 1.2. Studies of protein thermal stability adsorbed onto mesoporous silica (MPS) materials

Biomolecule	Silica Type / Surface Modification	Thermal Stability	Reference
α -L-arabinofuranosidase	MPS Organosilica (MPS / HPNO ^f)	Thermal stability of adsorbed enzyme on MPS does not improve in comparison to unprotected enzyme. Thermal stability of adsorbed enzyme on organosilica moderately improves in comparison to unprotected enzyme.	³⁷
β -galactosidase (from <i>Bacillus circulans</i>)	MPS / CTAB ^a and GPTMS ^b	Adsorbed enzyme on glyoxyl silica retained over 90% activity over 24 h and increased half-life from 1 h (unprotected) to 18 h.	³⁸
β -galactosidase (from <i>Bacillus circulans</i>)	MPS / CTAB ^a and GPTMS ^b	At 60 °C, half-life of adsorbed enzyme was about 11 h, half-life of unprotected enzyme was about 1 h.	³⁹
β -galactosidase (from <i>Aspergillus oryzae</i>)	MPS / CTAB ^a and GPTMS ^b	At 55 °C, half-life of adsorbed enzyme was about 14 h, half-life of unprotected enzyme was about 2 h.	³⁹
Alcalase 2T	MPS / APTES ^c	Adsorbed enzyme retains over 90% activity when heated to 50 °C for 2 h (unprotected enzyme retains about 55% activity).	⁴⁰

		Adsorbed enzyme loses most of its activity when heated to 60 °C for 2 h (unprotected enzyme also lost most of its activity).	
Amylase	MPS / agarose gel	At 80°C, adsorbed enzyme retained 93% activity, unprotected enzyme retained 38% activity.	41
Cellulase	Silica / polyamidoamine dendrimer	After heating to 70 °C for 3 h, adsorbed enzyme retained 53% activity, unprotected enzyme retained 22% activity.	42
Cytochrome C + peroxidase	Porous silicon microparticles (PSi) and biogenic porous silica (BSiO ₂) / No modification	Adsorbed enzyme on Psi did not improve thermal stability after heating to 50 °C for 4 h. Adsorbed enzyme on BSiO ₂ showed an increase in thermal stability in comparison to unprotected enzyme after heating to 50°C for 4 h.	43
Invasion Plasmid Antigen D (IpaD)	MPS / No modification	Adsorbed IpaD retains α -helical structure while unprotected IpaD completely denatured (CD) after heating to 95 °C for 2 h.	44
Laccase (from <i>Aspergillus</i>)	MPS / glutaraldehyde	The half-life of adsorbed enzyme was slightly lower than that of unprotected enzyme at temperatures between 55-70 °C.	45
Lipase (from <i>Alcaligenes</i>)	MPS / CTAB ^a and GPTMS ^b	At 55 °C, half-life of adsorbed enzyme was about 12 h, half-life of unprotected enzyme was about 3 h.	39
Lipase (from <i>Acaligenes</i>)	Glyoxyl silica (MPS / CTAB ^a and GPTMS ^d) Octyl silica (MPS / CTAB ^a and OTMS ^e) Octyl-Glyoxyl silica (MPS / GTMS and OTMS)	At 60 °C, half-life of adsorbed enzyme on glyoxyl silica was 566 h, half-life of unprotected enzyme was 0.97 h. At 60 °C, half-life of adsorbed enzyme on octyl silica was 7.9 h, half-life of unprotected enzyme was 0.97 h. At 60 °C, half-life of adsorbed enzyme on octyl-glyoxyl silica was 7.9 h, half-life of unprotected enzyme was 0.97 h.	46
Lipase (from <i>Candida antarctica B</i>)	MPS / CTAB ^a and GPTMS ^b	At 55 °C, half-life of adsorbed enzyme was about 9 h, half-life of unprotected enzyme was less than 1 h	39
Lipase B (from <i>Candida antarctica</i>)	MPS / TCT ^c	At 50 °C, half-life of adsorbed enzyme was 24 h, half-life of unprotected enzyme was 0.5 h.	47
Lipase (from <i>Candida antarctica</i>)	MPS / octyltriethoxysilane	At 60 °C, half-life of adsorbed enzyme was 2 h, half-life of unprotected enzyme was about 0.5 h.	48
Lipase (from <i>Pseudomonas stutzeri</i>)	Glyoxyl silica (MPS / CTAB ^a and GPTMS ^d) Octyl silica (MPS/ CTAB ^a and OTMS ^e) Octyl-Glyoxyl silica (MPS / CTAB, GTMS and OTMS)	At 60 °C, half-life of adsorbed enzyme on glyoxyl silica was 12.6 h, half-life of unprotected enzyme was 0.8 h. At 60 °C, half-life of adsorbed enzyme on octyl silica was 13 h, half-life of unprotected enzyme was 0.8 h. At 60 °C, half-life of adsorbed enzyme on octyl-glyoxyl silica was 153 h, half-life of unprotected enzyme was 0.8 h.	46
Lipase (from <i>Phycomyces nitens</i>)	FSM / CTAB ^a coating after adsorption	Adsorbed lipase on FSM-CTAB retained full activity after thermal treatment at 58 °C for 120 min. FSM only was not enough to stabilize protein.	49

Methemoglobin	FSM / Swelling Agent	Adsorbed enzyme retained 73% absorbance intensity of Soret peak compared to unprotected enzyme that only retained 34% intensity (CD) at 75 °C. Adsorbed enzyme was stabilized while unprotected enzyme unfolded and denatured at 85 °C.	50
---------------	----------------------	--	----

^a CTAB: cetyltrimethylammonium bromide, ^b GPTMS: glycidyoxypropyltrimethoxysilane, ^c APTES: 3-aminopropyltriethoxysilane, ^d TCT: trichlorotriazine, ^e OTMS: trimethoxy(octyl) silane, ^f HPNO: 2-hydroxypyridine 1-oxide

Surface modification is crucial for protein stabilization as shown in Table 1.2. It is also important to note that all the proteins listed in Table 1.2 except for IpaD (which is a sub-unit protein) are all enzymes. For the most part, physical adsorption is not enough to thermally stabilize enzymes, and therefore covalent binding is necessary.⁵¹ For enzymes to bond covalently to mesoporous silica materials, the surface must be modified. This can be achieved by grafting different functional groups, such as amino or carboxyl groups, onto the surface of the silica. Another option is using a cross-linking agent, such as glutaraldehyde for derivatization.⁵¹ Table 1.2, the surface modification agents used to promote covalent bonding are CTAB, APTES, TCT, glutaraldehyde and HPNO.

Another useful type of surface modification is to make the silica surface more hydrophilic or more hydrophobic. OTMS and octyltriethoxysilane can be used to add silane groups and lead to a more hydrophobic silica surface. For some enzymes, adsorption did not occur without OTMS treatment.⁴⁸ On the other hand, GTMS is a solvent used to add more glyoxyl groups onto the silica and consequently the surface becomes more hydrophilic. Glyoxyl groups are very reactive with non-ionized amine groups, are extremely stable at alkaline pHs, and are highly reactive with non-ionized amine groups and thus are a great functional group candidate to improve protein stabilization.⁵² The amine groups in the enzyme attach to a monolayer of moderately separated aldehyde groups on the surface of the silica (glyoxyl silica). It has been shown that as concentration of glyoxyl groups increases, the protein thermal stability increases.³⁸

1.2.3 Porous Activated Carbons

Activated carbon is a form of carbon that is porous, has a large internal surface area, and has relatively high mechanical strength.⁵³ Porous activated carbons (AC) are widely used industrially as adsorbents, catalyst supports, and for chemical separation or purification processes.⁵⁴ Activated carbon is an expensive material, and therefore alternative, cost effective raw materials for the production of AC are of great interest. Commercial AC is typically produced from coal and agricultural byproducts of lignocelluloses. Agricultural wastes and biomasses, including coconut shells, fruit stones, rice husk, peanuts, tamarind wood, bamboo, bagasse, oil palm waste, and agricultural residues from sugarcane are excellent choices for carbon precursors.⁵³

Some raw agricultural biomasses can be used as adsorbents without the need for activation; however, the activation process is meant to improve the adsorption capacity. It is important to note that different activation conditions may be necessary for different biomass sources since the ash composition varies from source to source.⁵⁵ Evidently, the nature of the carbon precursor (meaning the content of ash, moisture, lignin, cellulose, and hemicellulose) and the activation method have a significant influence on the pore structure and surface chemistry of the AC.

There are two key steps in the production of AC, carbonization, and activation. There are two ways to go about the carbonization and activation processes: chemical activation and physical activation. In chemical activation, the precursor lignocellulosic material is impregnated with dehydrating agents at temperatures, between 400 °C and 900 °C. The carbonization and activation steps occur simultaneously. Some of the chemical agents used for the activation process include: ZnCl_2 , KOH , NaOH , H_2PO_4 , and K_2CO_3 .^{54, 55} In physical activation, the carbonization and activation steps are performed separately. First, the precursor material is carbonized and then it is activated at high

temperatures, between 800 °C and 1100 °C using a gas flow of CO₂ or H₂O.⁵⁴ Overall chemical activation is preferred due to the lower operating temperature.

Table 1.3 Studies of protein thermal stability adsorbed onto porous activated carbon materials

Biomolecule	Carbon Material	Thermal Stability	Ref.
Acidic Lipase (from <i>Pseudomonas gessardii</i>)	Mesoporous activated carbon (MAC)	After heating to 50 °C for 24 h, unprotected enzyme retained 52% activity, immobilized retained 79% activity.	56
Acidic Lipase (from <i>Pseudomonas gessardii</i>)	Functionalized mesoporous activated carbon (FMAC) ¹	After heating to 50 °C for 24 h, unprotected enzyme retained 38% activity, enzyme immobilized on MAC retained 69% activity, enzyme immobilized on FMAC retained 92% activity.	57
Acid protease	Highly porous activated carbon (HPAC)	After heating to 80 °C, unprotected enzyme retained 40% activity, immobilized enzyme retained 64% activity.	58
Acid protease	Functionalized mesoporous activated carbon (FMAC) ¹	After heating to 80 °C, unprotected enzyme retained 40% activity, immobilized enzyme retained 69% activity.	59
Catalase	Porous activated carbon (AC) + gelatin (Gel) coating	After heating to 60 °C for 2 h, unprotected enzyme retained 10% activity, enzyme immobilized on AC retained 44% activity and enzyme immobilized on AC + Gel retained 57% of activity.	60
Laccase (from <i>Aspergillus</i>)	Activated carbon fibers (ACF) Activated carbon fibers functionalized with dopamine (DA-ACF)	After heating to 70 °C for 5 h, unprotected enzyme retained 10% activity, enzyme immobilized on ACF retained 40% activity, enzyme immobilized on DA-ACF retained 50% activity.	61
Laccase (from <i>Bacillus</i>)	Functionalized activated carbon nanotubes (ACNT) (with glutaraldehyde)	After heating to 80 °C for 5 h, unprotected enzyme retained 50% of activity, immobilized enzyme retained 65% of activity.	62
Lipase (from <i>Candida rugosa</i>)	Activated carbon	At 70°C, unprotected enzyme retained 45% activity, immobilized carbon retained 78% activity.	63
Lipase (from porcine pancreas)	Activated carbon from yellow mombin fruit stones	After heating to 50 °C for 180 min, immobilized enzyme retained 76% activity.	54
Lysozyme	Biomass charcoal powder (BCP) from adzuki bean	After heating to 90 °C for 30 min, immobilized enzyme retained 51% activity, unprotected enzyme lost all activity.	64
Papain	Multi-walled carbon nanotubes (MWCNT) + silica coating (TMOS)	After heating to 60 °C for 4 h, unprotected enzyme retained 30% activity, enzyme immobilized on MWCNT retained 70% activity and enzyme immobilized on silica coated MWCNT retained 94% activity.	65
Pectinase (from <i>Aspergillus ibericus</i>)	Functionalized nanoporous activated carbon (FNAC) ¹	After heating to 60 °C, unprotected enzyme retained 36% activity, immobilized enzyme retained 47% activity.	66

¹ Functionalized using ethylenediamine (EDA) and glutaraldehyde

When comparing the thermal stability of lysozyme immobilized in mesoporous activated carbon and that of lysozyme encapsulated in silica sol-gel, it is evident that the sol-gel methodology has a far higher degree of stability (Table 1.3 vs Table 1.1). Over 75% of the enzyme's activity is conserved while it is encapsulated in silica-sol gel and heated to 100 °C for 5h,²⁷ while only 51% of the enzyme's activity is retained when it is immobilized on BCP and heated to 90 °C for 30 min.⁶⁴ On the other hand, activated carbon provides much better thermal stability for laccase (from *Aspergillus*) than mesoporous silica. Adsorption of laccase onto mesoporous silica does not improve thermal stability,⁴⁵ but immobilization on functionalized activated carbon fibers significantly improves thermal stability.⁶¹ This may be attributed in part to the dopamine surface modification of the activated carbon fibers, increasing the hydrophilicity of the support. The report goes on to show that there is not one superior material that will successfully thermally stabilize every single type of protein.

As with mesoporous silica materials, functionalization is also important for porous activated carbon materials. Sekaran and coworkers have immobilized acidic lipase and acidic protease in both mesoporous activated carbon (MAC) and in functionalized activated mesoporous activated carbon (FMAC).^{56-59, 66} The enzymes adsorbed on MAC were stabilized via physical adsorption and those adsorbed on FMAC were stabilized through covalent interactions. The functionalization by Sekaran and coworkers is two-fold: first, ethylenediamine is used to add amino groups to the MAC surface, then second, glutaraldehyde is used to activate the amino groups on the support.⁵⁷ In every case, immobilization by enzyme covalent bonding to the activated carbon shows a significant increase in thermal stability in comparison to physical adsorption.

Another reason covalent bonding is preferred to physical adsorption for the thermal stabilization of enzymes is that in industrial catalytic procedures, enzymes tend to leach from AC. Porous

activated carbon materials have also been coated with silica and gelatin through sol-gel procedures to promote covalent bonding over physical adsorption.^{60,65} Catalase immobilized on gelatin coated AC showed a higher degree of thermal stability than immobilization in non-functionalized AC, since gelatin has carboxyl, amino, and hydroxyl functional groups that induce covalent bonding.⁶⁰ A two-step silica (TMOS) coating process provides one of the highest retained activities reported for enzyme immobilization on activated carbon materials. First, multiwalled carbon nanotubes were functionalized with amines, then, papain was adsorbed onto the MWCNT. TMOS was hydrolyzed and the papain-MWCNT conjugates were added to the TMOS solution and the gel consequently was formed. This double stabilization method (immobilization on AC followed by sol-gel encapsulation) results in approximately 94% activity retention of papain after heating to 60° C for 4 h.⁶⁵

There has been remarkable success with protein thermal stabilization using carbon paste, a non-porous carbon material. Polyphenol oxidase entrapped in carbon paste retained 95% activity after heating to 80 °C for 6 h, while the unprotected enzyme lost all activity after 30 min of heating.⁶⁷ Immobilization in carbon paste may be an attractive alternative for enzymes that cannot be stabilized in porous silica and carbon materials.

1.2.4 Aluminum and Iron Oxides

Silicon dioxides (silicas) are the most common class of metal oxide studied and applied to the stabilization of biomolecules. This is because silica is a benign and non-toxic oxide, and even though it is “Generally Recognized as Safe” by the FDA, it is not approved in injectable drugs. However, aluminum oxide (alumina) is already an FDA approved adjuvant in most high-volume vaccinations and injected both subcutaneously and intramuscularly.⁶⁸ Furthermore, alumina is the most common metal oxide used industrially for catalyst immobilization.⁶⁹ Iron oxide (magnetite)

is another attractive metal oxide for protein immobilization. Magnetite is approved in multiple parenteral administrations into the human body: as a component in magnetic resonance imaging and for the treatment of anemia and chronic liver failure.⁷⁰ An important advantage of magnetite as a drug carrier is that due to the magnetic property, these materials can deliver drugs to any desired, targeted location if the patient is under an external magnetic field.

The most common structure of crystalline alumina has oxygen ions in a closely packed, nearly hexagonal structure, and the aluminum ions occupy approximately two-thirds of the octahedral interstices. The crystal structure of aluminum oxide is thermally stable, making it an attractive support for enzymes. Also, the surface of alumina has both basic and acidic areas, which in turn help different basic and acidic amino acid residues anchor to the surface. Finally, the porosity is appropriate for enzymes, and is of nanometric scale, but still large enough for large substrates to fit. Even though the pore size of alumina is convenient for enzymes, it is possible larger and more complex molecules (i.e., vaccines and large proteins) will not fit into aluminum oxide's nanopores.

Table 1.4. Studies of protein thermal stability adsorbed onto porous aluminum oxide metals

Biomolecule	Metal Oxide Material	Thermal Stability	Reference
Acid Phosphatase	Sol-gel magnetite nanoparticles	Denaturation temperature of the entrapped enzyme increases by 22 °C (DSC).	70
Acid Phosphatase	Sol-gel boehmite nanoparticles	Entrapped enzyme retained secondary structure up to 90 °C, unprotected enzyme lost structure starting at 40 °C (CD melt).	68
Asparaginase	Sol-gel boehmite nanoparticles	Entrapped enzyme retained secondary structure up to 90 °C, unprotected enzyme lost structure starting at 65 °C (CD melt).	68
Bovine Carbonic Anhydrase	Sol-gel magnetite nanoparticles	Denaturation temperature of the entrapped enzyme increases by 30 °C (DSC).	70
Bovine Serum Albumin	Sol-gel boehmite nanoparticles	Denaturation temperature of the entrapped enzyme increases by 50 °C (DSC).	71
Catalase (from <i>Bacillus</i>)	Functionalized alumina pellets (silane + glutaraldehyde)	At 70 °C entrapped enzyme retained 28% activity, unprotected enzyme retained 8% activity.	72
Chondroitinase ABCI	Magnetite nanoparticles	At 40 °C, immobilized enzyme retained 44% activity, unprotected enzyme retained 8% activity.	73

Horseradish Peroxidase	Sol-gel boehmite nanoparticles	Entrapped enzyme retained secondary structure up to 90 °C, unprotected enzyme lost structure starting at 65 °C (CD melt).	68
Horseradish Peroxidase	Sol-gel magnetite nanoparticles	Denaturation temperature of the entrapped enzyme increases by 25 °C (DSC).	70
Human Serum Albumin	Sol-gel boehmite nanoparticles	Denaturation temperature of the entrapped enzyme increases by 26 °C (DSC).	71
Lipase (from <i>Rhizomucor miehei</i>)	Nanoporous anodic aluminum oxide membranes	At 60 °C, immobilized enzyme retained 95% activity, unprotected enzyme retained 78% activity.	74
Ovalbumin	Sol-gel boehmite nanoparticles	Denaturation temperature of the entrapped enzyme increases by 30 °C (DSC).	71
Ovalbumin	Sol-gel magnetite nanoparticles	Denaturation temperature of the entrapped enzyme increases by 10 °C (DSC).	70
Papain	Functionalized alumina (organic phosphates)	Thermal stability of entrapped enzyme was slightly lower than that of the unprotected enzyme between 35 °C-90 °C.	75
Proteinase	Sol-gel boehmite nanoparticles	Entrapped enzyme retained secondary structure up to 90 °C, unprotected enzyme lost structure starting at 35 °C (CD melt).	69
Proteinase	Sol-gel magnetite nanoparticles	Denaturation temperature of the entrapped enzyme increases by 27 °C (DSC).	70
Xylanase	Sol-gel boehmite nanoparticles	Entrapped enzyme retained secondary structure up to 90 °C, unprotected enzyme lost structure starting at 51 °C (CD melt).	69
Xylanase	Functionalized alumina pellets (glutaraldehyde)	After heating to 75 °C for 2 h, entrapped enzyme retained 8% activity, unprotected enzyme lost all activity.	76
Xylanase	Sol-gel magnetite nanoparticles	Denaturation temperature of the entrapped enzyme increases by 21 °C (DSC).	70

As evidenced on Table 1.4, there has been little success achieving a high degree of thermal stabilization of enzymes onto mesoporous aluminum oxide materials. Even with glutaraldehyde and silane surface functionalization, there is only about a 20% increase in retained enzyme activity in the best of cases. However, Vinogradov and coworkers have had much better results when using the sol-gel encapsulation method. When comparing the results of xylanase entrapped in a sol-gel matrix and xylanase adsorbed onto functionalized alumina pellets, the former retained all of its secondary structure up to 90 °C and the latter was only able to conserve 8% activity at 75 °C.^{69, 76} Vinogradov and coworkers used aluminum isopropoxide and ultrasonic energy to prepare the boehmite nanoparticles sol.⁶⁹ The enzymes were then added to the alumina sol in glycine-NaOH

or glycine-HCl buffer solutions and placed under vacuum at room temperature for 24 hours to produce the gel.⁶⁸ A similar process using iron (II) chloride tetrahydrate, iron (III) chloride hexahydrate, and ammonia was executed to produce the magnetite nanoparticles sol.⁷⁰ In general, the thermal stability of ovalbumin, horseradish peroxidase, acid phosphatase, xylanase, and proteinase is better in alumina than in magnetite.⁶⁸⁻⁷¹ Overall, the sol-gel alumina method for the thermal stability of proteins shows very promising results since this technology has been successful with at least eight different enzymes.^{68, 69, 71} Nonetheless, if the protein delivery benefits from magnetic maneuverability, magnetite may be the better support candidate over alumina.

Vinogradov and coworkers have not published data on the protein release from the boehmite and magnetite nanoparticles, which is crucial for their technology to be used in a clinical setting. Alemzadeh and coworkers have proven the thermal stability and release of chondroitinase ABCI (cABCI) in magnetite particles. The enzyme was desorbed from the magnetite particles in phosphate buffer. After one hour, 52% of cABCI was released and a remaining 42% cABCI was released over the next six hours.⁷³

1.2.5 Metal Organic Framework

A metal organic framework (MOF) is a three dimensional crystalline porous structure composed of metal or metal oxide vertices interconnected by organic ligands. It is analogous to a three-dimensional interconnected system of coordination compound. The preservation mechanism of a protein within a MOF is accredited to the coordination interactions between the MOF and the protein, resulting in a tightly packed encapsulation.⁷⁷ There are two main types of strategies for protein immobilization inside a MOF. In the presynthetic method, the biomolecule is soaked in a buffered solution with the mesoporous MOF, encapsulating the enzyme into the pores of the mesoporous MOF (much like protein adsorption onto mesoporous silica, see Figure 1.3). The de

novo approach consists of the enzymes co-precipitating with the MOF precursor to form a lattice structure around the enzyme (much like protein encapsulation in sol-gel silica).

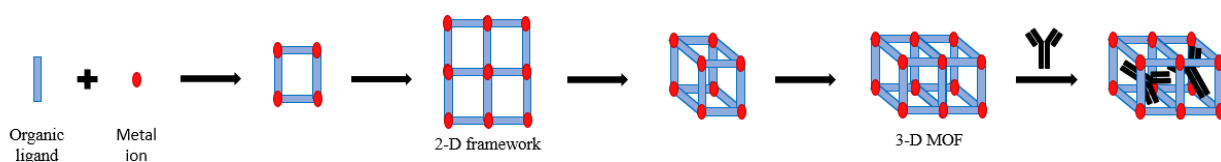


Figure 1.3. Protein adsorption onto MOF

MOFs are ideal for a wide range of applications, including drug delivery, enzyme immobilization, chemical sensors, and catalysis. Some of the relevant properties include- tunable surface chemistry and porosity, large surface area, rich organic functionality, and of course, excellent thermal stability.⁷⁸ In theory, a MOF can be customized to any desired size, shape symmetry, and chemical functionality by interchanging organic linkers and metal ions.⁷⁹ Using MOFs for protein stabilization has only become popular within the past five years, but the promising results guarantee MOFs have a lot of potential in the field of biomolecule thermal stabilization and delivery.

Table 1.5. Studies of protein thermal stability on Metal Organic Framework

Biomolecule	MOF / Desorbing agent	Thermal Stability	Reference
α -amylase	Functionalized ZIF-8 with glutaraldehyde	At 70 °C, encapsulated enzyme retained 87% activity, unprotected enzyme retained 20% activity.	80
Alcohol Dehydrogenase	PCN-333	After heating to 80 °C for 5 min, encapsulated enzyme retained 66% activity, unprotected enzyme retained 57% activity.	79
Alkaline phosphatase	DNA functionalized magnetic particles + ZIF-8	After heating to 55 °C for 90 min, encapsulated enzyme retained 83% activity.	81
Catalase	Silica nanoflowers (SNF) + ZIF-8	After heating to 65 °C for 3 h, encapsulated enzyme retained 68% activity, unprotected enzyme retained 7% activity.	82
Cutinase	Isoreticularly expanded MOF-74 (IRMOF-74)	At 227 °C, encapsulated enzyme conserved 50% α -helical content, unprotected enzyme conserved 30% α -helical content.	83
Cytochrome C	DNA functionalized magnetic particles + ZIF-8	After heating to 55 °C for 90 min, encapsulated enzyme retained 91% activity.	81
Cytochrome C	ZIF-8	After heating to 70 °C for 6 h, encapsulated enzyme increased activity up to 450%.	84

Hemoglobin	ZIF-8	After heating to 153 °C for 1 h, encapsulated hemoglobin retained 80% activity, unprotected hemoglobin lost all activity.	85
Horseradish Peroxidase	DNA functionalized magnetic particles + ZIF-8	After heating to 60 °C for 90 min, encapsulated enzyme retained 92% activity, unprotected enzyme retained 18% activity.	81
Horseradish Peroxidase	ZIF-8	After heating to 50 °C for 6 h, encapsulated enzyme retained 90% activity, unprotected enzyme retained 40% activity.	84
Insulin	Zeolitic imidazolate framework-8 (ZIF-8)	After one-week storage at 60 °C, encapsulated insulin retained 75% activity, unprotected insulin retained less than 30% activity.	86
Lipase (from <i>Candida antarctica</i>)	ZIF-8	After heating to 40 °C for 6 h, encapsulated enzyme retained 90% activity, unprotected enzyme retained 63% activity.	84
Penicillin G acylase	Silica nanoflowers (SNF) + ZIF-8	After heating to 55 °C for 3 h, encapsulated enzyme retained 52% activity, unprotected enzyme retained 8% activity.	82
Trypsin	DNA functionalized magnetic particles + ZIF-8	After heating to 55 °C for 90 min, encapsulated enzyme retained 95% activity.	81

By far, zeolitic imidazolate framework-8 (ZIF-8) is the most widely studied MOF for protein thermal stabilization. ZIFs are a type of MOF with large pores and small apertures, and the same topology as inorganic zeolites with sodalite.⁸⁷ ZIF-8 is made up of 2-methylimidazole ligands and zinc- forming a framework that has high thermal and chemical stability and a uniform porosity. ZIF-8-protein complexes are produced by mixing enzyme, zinc nitrate hexahydrate, and 2-methylimidazole water solutions and stirring at room temperature. It is not a surprise that so many proteins can be adsorbed and stabilized within ZIF-8. In comparison to other thermal stabilization methods discussed previously, MOFs have proven to be one of the most successful. Most of the experiments summarized in Table 1.5 show over 75% enzyme activity retention after exposure to heat stress.

A few of the publications in Table 1.5 used a combination of stabilization materials along with MOFs. Yang and coworkers developed a multi-step pre-immobilization and post encapsulation method consisting of DNA-directed enzyme immobilization on magnetic particles followed by encapsulation on ZIF-8 of the DNA-enzyme-magnetic particle conjugates.⁸¹ DNA was used as a

cross-linker in a similar way amino and carboxyl functional groups are added to silicas and activated carbons to promote covalent bonding. Furthermore, the DNA's phosphate groups can help the surface potential be more negative, which in turn can facilitate the formation of the ZIF-8 network.⁸¹ Yang and coworkers achieved over 80% retention of activity at high temperatures for cytochrome c, horseradish peroxidase, alkaline phosphatase, and trypsin, demonstrating the versatility and efficiency of the multi-step process across a range of different enzymes.

Yiang and coworkers also employed a multi-step system consisting of adsorption on nanoflower silica and encapsulation of ZIF-8 to thermally stabilize penicillin G acylase and catalase.⁸² Silica nanoflowers have relevant advantages, such as high surface area and high thermal stability, but the channel structure of the nanoflowers is too open and could result in enzyme leeching. ZIF-8 is used as a second level of protection to ensure the enzyme stays safely in place. Yiang and coworkers obtained promising results with penicillin G acylase and catalase; however, it may be possible to achieve an even higher level of thermal stability by using a more compact and functionalized mesoporous silica (for covalent bonding to avoid leeching) in combination with a MOF.

Singamaneni and coworkers successfully thermally stabilized insulin in ZIF-8 and also released the protein from the ZIF-8 network in one minute.⁸⁶ Ethylenediaminetetraacetic acid (EDTA) was used as the desorbing agent that works by breaking down the coordination bonds between zinc and 2-methylimidazole to release the stabilized insulin. However, there is some risk for EDTA to damage the protein structure, so in the future different detergents may need to be tested to ensure safe protein desorption.

1.3 Review of Organic Polymer Materials for Protein Immobilization

1.3.1 Natural Polymers

Natural polymers are by far the materials that have been studied the most for proteins stabilization. They are excellent candidates for enzyme immobilization due to the abundance of functional groups on their surfaces that are able to form covalent bonds with the enzyme. In the case of natural polymers, immobilization is typically through covalent bonding instead of physical adsorption, but there are some cases of immobilization through reversible ionic bonding. Agarose is a linear polysaccharide isolated from seaweed that consists of alternating D-galactose and 3,6-anhydro-L-galactopyranose units.⁸⁸ The polymer forms flexible fibers that create a web of channels with diameters ranging between 30 nm and 200 nm. The pore size of the agarose gel is highly dependent on the agarose concentration. Agarose beads with 6% agarose have a pore size of about 30 nm, but agarose beads with 2% agarose have a pore size of about 150 nm.⁸⁹ Agarose contains reactive hydroxyl groups that are able to form aldehydes when reacting with glutaraldehyde.⁹⁰ These aldehydes groups on the surface of the polymer can form covalent bonds with the amine groups of the enzyme to immobilize it.

Chitosan is another linear polysaccharide, which derived from the chitin shells of crustaceans such as shrimp. It is an attractive natural polymer for protein stabilization not only because of its biocompatible, biodegradable, hydrophilic and antibacterial features, but it is also derived from chitin, the second most abundant natural polymer after cellulose.⁹¹ Chitosan is made up of randomly alternating D-glucosamine and N-acetyl-D-glucosamine units. The pore size of chitosan matrices is larger than that of agarose, ranging between 50 to 200 μm . Chitosan is not only the most widely used polymer, but also the most widely used material for enzyme thermal stabilization, largely in part because it contains amino groups on its surface, greatly facilitating the

formation of covalent bonds between proteins and the chitosan surface. Besides agarose and chitosan, alginate (from seaweed extract), chitin (from crustacean shells), cellulose (from plant cell walls) and trehalose (synthesized by animals, bacteria, plants and fungi as a source of energy) are other natural polymers that have been studied for protein immobilization.

Table 1.6. Studies of protein thermal stability on natural polymers

Biomolecule	Natural Polymeric Material	Thermal Stability	Ref.
Agarose			
α -Chymotrypsin	Glyoxyl-agarose	After storing at 37 °C for 5 days, immobilized enzyme retained 19% activity, unprotected enzyme lost all activity.	92
β -glucosidase	Amine-epoxy agarose PEI agarose Glutaraldehyde agarose Amino-glutaraldehyde	After heating to 65 °C for 2h, enzyme immobilized on PEI-agarose retained 25% activity, enzyme immobilized on glutaraldehyde agarose retained 46% activity, enzyme immobilized on amino-glutaraldehyde agarose retained 47% activity, enzyme immobilized on amine-epoxy agarose retained 95% activity.	93
β -glucosidase	Amine agarose (EDA)	After heating to 53 °C for 10 h, immobilized enzyme retained 90% activity, unprotected enzyme retained 48% activity.	94
Alcalase	Glyoxyl agarose Glutaraldehyde agarose	After heating to 50 °C for 30 h, enzyme immobilized on glyoxyl-agarose retained 90% activity, enzyme immobilized on glutaraldehyde agarose retained 20% activity, unprotected enzyme lost all activity.	95
Amylase (from <i>Aspergillus carbonarius</i>)	Glutaraldehyde-agarose Polyglutaraldehyde-agarose Glycidol-agarose Non-activated agarose	After heating to 60 °C for 2 h, enzyme immobilized on glutaraldehyde-agarose retained 82% activity, enzyme immobilized on polyglutaraldehyde-agarose retained 88% activity, enzyme immobilized on glyceryl-agarose retained 96% activity, enzyme immobilized on non-activated agarose retained 97% activity.	90
Amylase (from sweet potato)	Glutaraldehyde-agarose	At 80 °C, immobilized enzyme retained 70% activity, unprotected enzyme retained 22% activity.	96
Angiotensin-converting enzyme	Glyoxyl agarose	After heating to 60 °C for 2.5 h min, immobilized enzyme retained 40% activity, unprotected enzyme lost all activity.	97
Ficin extract	Glutaraldehyde agarose	After heating to 55 °C for 4 h, immobilized enzyme retained 50% activity, unprotected enzyme retained 40% activity.	98
Glucoamylase (aminated with EDA)	Glyoxyl-agarose	After heating to 45 °C for 20 h, immobilized aminated enzyme retained 78% activity, immobilized non-aminated enzyme retained 36% activity, unprotected enzyme retained 14% activity.	99
Laccase	Antibody linked Sepharose	At 90 °C, immobilized enzyme retained 45% activity, unprotected enzyme retained 20% activity.	100
Lipase (from <i>Rhizomucor miehei</i>)	Octyl-glyoxyl agarose in CaCl ₂ buffer	After heating to 60 °C for 2 h, immobilized enzyme in CaCl ₂ retained 47% activity, immobilized enzyme retained 35% activity, unprotected enzyme lost all activity.	101
Lipase B (from <i>Candida antarctica</i>)	Octyl agarose modified with polyethyleneimine (PEI)	After heating to 80 °C for 5 h, enzyme immobilized on octyl agarose-PEI retained 50% activity, enzyme immobilized on octyl agarose retained 38% activity.	102
Lipase B (from <i>Candida antarctica</i>)	Glycidol-agarose Glutaraldehyde-agarose Epichlorohydrin-agarose	At 50 °C. half-life of enzyme on glycidol-agarose was 3.7 h, on glutaraldehyde-agarose was 4.3 h, on epichlorohydrin-agarose was 2.9 h.	103
Lipase (from <i>Rhizomucor miehei</i>)	Octyl agarose coated with PEI	After heating to 60 °C for 4 h, immobilized enzyme retained 93% activity, unprotected enzyme retained 8% activity.	104

Lipase (from <i>Pseudomonas fluorescens</i>)	Glyoxyl-octyl agarose	After heating to 75 °C for 2h, enzyme immobilized on glyoxyl-octyl agarose retained 40% activity, enzyme immobilized on octyl agarose retained 19% activity.	105
Lipase (from <i>Candida rugosa</i>)	Divinyl sulfone activated-octyl agarose (DSAOC) Octyl agarose (OC)	After heating to 70 °C for 6h, enzyme immobilized on DSAOC retained 75% activity, enzyme immobilized on OC retained 12% activity.	106
Lipase (from <i>Thermomyces lanuginosus</i>)	Glyoxyl agarose	After heating to 70 °C for 20h, immobilized enzyme retained 50% activity, unprotected enzyme lost all activity.	107
Penicillin G acylase	Agarose (formaldehyde modification)	At 25 °C for 4 h, immobilized and modified enzyme retained 60% activity, immobilized (but not modified) enzyme and unprotected enzyme retained 10% activity.	108
Ribonuclease A	Antibody linked Sepharose	At 80 °C, immobilized enzyme retained 50% activity, unprotected enzyme retained 24% activity.	109
Xylanase	Glyoxyl-agarose Agarose-glutaraldehyde Agarose-amino-epoxy	Thermal stability of enzyme immobilized in all three supports was inferior to that of the unprotected enzyme.	110
Chitosan			
α -Amylase (soybean)	Glutaraldehyde-chitosan	At 80 °C, immobilized enzyme retained 65% activity, unprotected enzyme retained 35% activity.	111
α -Amylase (mung bean)	Glutaraldehyde-chitosan	At 85 °C, immobilized enzyme retained 68% activity, unprotected enzyme retained 36% activity.	91
α -galactosidase	Glutaraldehyde-chitosan	At 80 °C, immobilized enzyme retained 80% activity, unprotected enzyme retained 28% activity.	112
β -galactosidase	Glutaraldehyde-chitosan	At 80 °C, immobilized enzyme retained 80% activity, unprotected enzyme retained 24% activity.	112
β -galactosidase	Glutaraldehyde-chitosan macroparticles Glutaraldehyde-chitosan nanoparticles	After heating to 50 °C for 2 h enzyme immobilized on macroparticles retained 62% activity, enzyme immobilized on nanoparticles retained 21% activity.	113
β -galactosidase	Chitosan-coated magnetic nanoparticles	At 75 °C, immobilized enzyme retained 53% activity, unprotected enzyme retained 8% activity.	114
β -glucosidase (from <i>Aspergillus oryzae</i>)	Glutaraldehyde-chitosan Epichlorohydrin-chitosan (EC)	After heating to 60 °C for 100 min, GC immobilized enzyme retained 17% activity, EC immobilized enzyme retained 25% activity, unprotected enzyme retained 10% activity.	115
Alcalase	Glutaraldehyde-chitosan (GC) Glyoxyl-chitosan (GlyC) Divinyl sulfone-chitosan (DVSC)	After heating to 60 °C for 2.5 h, DVSC immobilized enzyme retained 39% activity, GlyC and GC immobilized enzyme retained 31% activity.	116
Alcalase	Glutaraldehyde-chitosan-coated magnetic nanoparticles	After heating to 50 °C for 2.5 h, immobilized enzyme retained 90% activity, unprotected enzyme retained 44% activity.	117
Alcohol dehydrogenase	Glutaraldehyde-chitosan-coated magnetic nanoparticles	At 50 °C, immobilized enzyme retained 68% activity, unprotected enzyme retained 45% activity.	118
Alliinase	N-succinyl-chitosan	At 50 °C, immobilized enzyme retained 90% activity, unprotected enzyme retained 52% activity.	119
Xylanase	Glutaraldehyde-chitosan (GC) Glyoxyl-chitosan Epoxy-chitosan	Enzymes immobilized on GC and epoxy-chitosan have a slightly better thermal stability than the unprotected enzyme.	110
Catalase (from bovine liver)	Chitosan	After heating to 40 °C for 2 h, immobilized enzyme retained 60% activity, unprotected enzyme retained 40% activity.	120
Catalase (from bovine liver)	Glutaraldehyde-chitosan with copper	Thermal stability was not improved by immobilizing enzyme.	121
Catalase (from bovine liver)	Chitosan	At 60 °C, immobilized enzyme retained 53% activity, unprotected enzyme retained 40% activity.	122
Catalase (from bovine liver)	Chitosan-poly(itaconic acid)-Fe(III) polymer	After heating to 55 °C for 2h, immobilized enzyme retained 88% activity, unprotected enzyme retained 67% activity.	123

Catalase (from bovine liver)	Glutaraldehyde-chitosan	At 65 °C, immobilized enzyme retained 73% activity, unprotected enzyme retained 28% activity.	124
Catalase (from bovine liver)	Chitosan-2-hydroxyethyl methacrylate (HEMA)-Cu(II)	After heating to 45 °C for 6 h, immobilized enzyme retained 67% activity, unprotected enzyme retained 50% activity.	125
Catalase (from bovine liver)	Chitosan Cibacron blue F3GA-chitosan	Thermal stability was not significantly improved by immobilizing enzyme.	126
Cellulase	Glutaraldehyde-chitosan-coated magnetic nanoparticles	After heating to 60 °C for 2h, immobilized enzyme retained 66% activity, unprotected enzyme retained 61% activity.	127
Glucoamylase	Glutaraldehyde-chitosan-coated magnetic nanoparticles	After heating to 65 °C for 2 h, immobilized enzyme retained 89% activity, unprotected enzyme retained 63% activity.	128
Invertase (from yeast)	Glutaraldehyde-chitosan	At 70 °C, immobilized enzyme retained 78% activity, unprotected enzyme retained 7% activity.	129
Invertase (from yeast)	Glutaraldehyde-chitosan	Thermal stability was not significantly improved by immobilizing enzyme.	130
Keratinase (from <i>Bacillus licheniformis</i>)	β -Cyclodextrin (β -CD) chitosan Chitosan	After heating to 60 °C for 2 h, enzyme immobilized on chitosan retained 90% activity, enzyme immobilized on β -CD chitosan retained 87% activity, unprotected enzyme retained 70% activity.	131
Laccase (from <i>Trametes versicolor</i>)	Glutaraldehyde-Chitosan/PVA nanofibrous membranes	At 55 °C. immobilized enzyme retained 58% activity, unprotected enzyme retained 45% activity.	100
Laccase (from <i>Trametes versicolor</i>)	Chitosan/CeO ₂ microspheres	After heating to 50 °C for 2.5h, immobilized enzyme retained 77% activity, unprotected enzyme retained 45% activity.	132
Laccase	Glutaraldehyde-chitosan-coated magnetic nanoparticles	At 70 °C, immobilized enzyme retained 100% activity, unprotected enzyme retained 73% activity.	133
Lipase (from <i>Candida rugosa</i>)	Glutaraldehyde +carboxyl groups chitosan	At 60 °C, immobilized enzyme retained 23% activity, unprotected enzyme retained 12% activity.	134
Lipase (from <i>Candida rugosa</i>)	Carbodiimide hydrochloride (EDC) activated chitosan	At 60 °C, immobilized enzyme retained 56% activity, unprotected enzyme retained 21% activity.	135
Lipase (from <i>Candida rugosa</i>)	EDC activated chitosan-poly(acrylonitrile-co-maleic acid) (PANCMA)	At 55 °C, immobilized enzyme retained 80% activity, unprotected enzyme retained 55% activity.	136
Lipase B (from <i>Candida antarctica</i>)	Butyl-chitosan (BC) Octyl-chitosan (OC) Dodecyl-chitosan (DC)	After heating to 35 °C for 50 h, BC and OC immobilized enzymes retained 80% activity, DC enzyme retained 100% activity, unprotected enzyme retained 93% activity.	137
Lipase (from <i>Rhizomucor miehei</i>)	Butyl-chitosan (BC) Octyl-chitosan (OC) Dodecyl-chitosan (DC)	After heating to 35 °C for 100 h, BC immobilized enzyme retained 37% activity, OC immobilized enzyme retained 59% activity, DC enzyme retained 90% activity, unprotected enzyme retained 42% activity.	137
Lipase B (from <i>Candida antarctica</i>)	Glycidol-EDA-glutaraldehyde chitosan Glutaraldehyde-chitosan (GC) Glutaraldehyde-chitosan-alginate (GCA)	After heating to 60 °C for 3 h, Gly-EDA-GC immobilized enzyme retained 53% activity, GC immobilized enzyme retained 38% activity, GCA immobilized enzyme retained 32% activity, unprotected enzyme retained 2% activity.	138
Lipase B (from <i>Candida antarctica</i>)	Glycidol-chitosan Glutaraldehyde-chitosan Epichlorohydrin-chitosan	At 50 °C. half-life of enzyme on glycidol chitosan was 1.8 h, on glutaraldehyde-chitosan was 4.9h, on epichlorohydrin-chitosan was 0.4 h.	103
Lipase (from <i>Candida rugosa</i>)	Chitosan/poly(vinyl alcohol) (PVA) nanofibrous membranes	At 50 °C, immobilized enzyme retained 82% activity, unprotected enzyme retained 46% activity.	139
Lipase (from <i>Candida rugosa</i>)	EDC-chitosan-coated magnetic nanoparticles	At 60 °C, immobilized enzyme retained 77% activity, unprotected enzyme retained 21% activity.	140
Pepsin (porcine)	Chitosan	At 50 °C, immobilized enzyme retained 100% activity, unprotected enzyme retained 60% activity.	141
Procerain B	Glutaraldehyde-chitosan	At 70 °C, immobilized protein retained 88% activity.	142

Trypsin	Glutaraldehyde-chitosan	At 60 °C, immobilized enzyme retained 80% activity, unprotected enzyme retained 10% activity.	143
Trypsin	Glutaraldehyde-chitosan (GC) Epoxy-chitosan (EC)	After heating to 70 °C for 20 min, enzyme immobilized on GC retained 45% activity, enzyme immobilized on EC retained 83% activity.	144
Urease (from pigeonpea)	Glutaraldehyde-chitosan	At 77 °C, immobilized enzyme retained 99% activity, immobilized enzyme retained 50% activity.	145
Urease (from soybean)	Chitosan	At 85 °C, immobilized enzyme retained 30% activity, unprotected enzyme retained 10% activity.	146
Alginate			
β -galactosidase	Alginate-carboxymethyl cellulose gel	After heating to 60 °C for 1 h, immobilized enzyme retained 43% activity, unprotected enzyme retained 8% activity.	147
γ -glutamyltranspeptidase	Calcium alginate-k-carrageenan	At 60 °C, immobilized enzyme retained 62% activity, unprotected enzyme retained 40% activity.	148
<i>Araujia</i>	Calcium alginate	After heating to 70 °C for 2 h, immobilized enzyme retained 53% activity, unprotected enzyme retained 12% activity.	149
Neutrase	Glutaraldehyde-alginate	After heating to 60 °C for 1 h, immobilized enzyme retained 50% activity, unprotected enzyme retained 2% activity.	150
Urease (from soybean)	Alginate	At 85 °C, immobilized enzyme retained 57% activity, unprotected enzyme retained 10% activity.	146
Alginate-Chitosan			
β -galactosidase	Calcium alginate-chitosan Barium alginate-chitosan	After heating to 37 °C for 24h, enzyme immobilized in Ca alginate-chitosan retained 32% activity, enzyme immobilized on Ba alginate chitosan retained 44% activity, unprotected enzyme retained 28% activity.	151
Alcohol dehydrogenase	Glutaraldehyde-alginate-chitosan	At 70 °C, immobilized enzyme retained 50% activity, unprotected enzyme lost all activity.	152
Trehalose			
β -glucanase	Trehalose hydrogel	At 90 °C, immobilized enzyme retained 99% activity, unprotected enzyme retained 44% activity.	153
Insulin	Trehalose-polyethylene glycol (PEG)-boronic acid hydrogel	After heating to 90 °C for 30 min, immobilized insulin retained 74% activity, unprotected enzyme retained 2% activity.	154
Phytase	Trehalose hydrogel	At 90 °C, immobilized enzyme retained 100% activity, unprotected enzyme retained 39% activity.	155
Xylanase	Trehalose hydrogel	At 90 °C, immobilized enzyme retained 107% activity, unprotected enzyme retained 15% activity.	153
Chitin			
Invertase (modified with chitosan)	Sodium alginate coated-chitin	After heating to 65 °C for 10 min, immobilized enzyme retained 95% activity, unprotected enzyme lost all activity.	156
Invertase (modified with chitosan)	Pectin coated-chitin	After heating to 65 °C for 30 min, immobilized enzyme retained 92% activity, unprotected enzyme retained 5% activity.	157
Cellulose			
Insulin	Cellulose hydrogel	After incubating at 37 °C for 28 days, the immobilized enzyme retained secondary protein structure (CD).	158
Lipase (from <i>Candida rugosa</i>)	Cellulose-PEG hydrogel	At 60 °C, immobilized enzyme retained 100% activity, unprotected enzyme retained 40% activity.	159

As shown in Table 1.6, for almost every protein immobilization case, the surface of the natural polymer must be modified. In most industrial catalysis applications, once the enzyme is stabilized, it should stay in place so that the production process can run uninterrupted for an extended period

of time. Therefore, protein release or leeching is never desired, and immobilization via covalent bonding is preferred. Most agarose, chitosan, and alginate polymers use glutaraldehyde due to its many advantages. Glutaraldehyde is a crosslinking agent, but it can also be used to activate amino groups and when added to agarose it reacts with the hydroxyl groups to form aldehyde groups (glyoxyl groups).^{91, 98} Glyoxyl groups can also be added to natural polymers using an epoxide reactant, such as glycidol, that similarly to glutaraldehyde, react with the hydroxyl groups to produce aldehyde groups.¹⁴⁴ Epichlorohydrin works like glycidol, but it is more reactive, causing a higher concentration of glyoxyl activation.¹⁰³ Formaldehyde and polyglutaraldehyde are other crosslinking agents that have been used in place of glutaraldehyde.¹⁰⁸ The addition of amino, hydroxyl, dodecyl, butyl, octyl, and vinyl sulfone groups and antibodies have also been shown to improve thermal stability. Ethylenediamine adds amino groups to improve covalent bonding. Carbodiimide hydrochloride activates hydroxyl groups to increase hydrophilicity.¹³⁵ On the other hand, dodecyl, butyl, and octyl groups are added as hydrophobic ligands on polymeric support.¹³⁷ Divinyl sulfone adds vinyl sulfone groups that are able to form bonds with amino, hydroxy, imidazole, and thiol groups on the protein.¹⁰⁶ Antibodies add cysteine amino acids that covalently bond to the labile region of the enzyme and protects this sensitive region from unfolding and denaturing.¹⁰⁹

Although covalent protein stabilization is effective, it is mostly irreversible. For biomedical vaccine and drug delivery applications, reversible immobilization is necessary. Ion-exchangers, hydrophobic polymer gels, and metal chelated supports can be used to promote reversible protein immobilization.¹²³ Reversible immobilization relies on strong, multipoint ionic attachment as a result of high protein adsorption onto the support surface. The most commonly used ionic exchange group is polyethyleneimine, but poly(itaconic acid), CeO₂, and HEMA-Cu(II) have also

been used in combination with chitosan.^{123, 125, 132} The addition of other synthetic polymers, such as β -CD, PVA, PANCMA, and N-succinyl typically have the purpose of increasing mechanical strength and thermal stability of the organic polymers.^{100, 119, 136} Regarding protein desorption, Fernandez-LaFuente and coworkers designed a octyl-agarose with PEI polymer capable of desorbing stabilized lipases using low concentrations of Triton X-100.¹⁰² Maynard and coworkers developed a trehalose-PEG-boronic acid hydrogel for the thermal stabilization and smart release of insulin. Glucose breaks down the boronate ester bonds that hold the trehalose and boronic acid bonds together, in turn releasing insulin.¹⁶⁰

1.3.2 Synthetic Polymers

Protein immobilization on a polymer depends on chemical (covalent or ionic) bonds between the protein's amino acid residues and functional groups on polymers. Natural polymers are attractive options because of the hydroxyl (agarose) and amino (chitosan) groups on their surfaces. However, synthetic polymers are rarely used for protein stabilization because of the lack of functional groups. Nonetheless, there are many advantages to synthetic polymers, especially the biocompatibility, inertness to microbial attack, and molecular tailorability.¹⁶¹ Overall, there has been some success to thermally stabilize proteins on synthetic polymers, but natural polymers have been investigated more extensively for this purpose. Table 1.7 summarizes studies that have used synthetic polymers for protein thermal stability.

Table 1.7. Studies of thermal stability on synthetic polymers

Biomolecule	Polymer	Thermal Stability	Ref
β -galactosidase	Poly (ethylene glycol)	After incubating at 60 °C for 2 weeks, immobilized enzyme retained 72% activity, unprotected enzyme retained 3% activity	¹⁶²
β -glucosidase	Polystyrene based diazonium salt (PS-DAS) - Polyethylene	After heating to 60 °C for 40 min, immobilized enzyme retained 72% activity, unprotected retained 22% activity	¹⁶¹
Alkaline Phosphatase	Poly (ethylene glycol)	After heating to 85 °C for 1 h, immobilized enzyme retained 58% activity, unprotected enzyme retained 10% activity	¹⁶²

Lipase (from <i>Candida rugosa</i>)	Poly(N-methololacrylamide)	After heating to 50 °C for 1 h, immobilized enzyme retained 70% activity, unprotected enzyme retained 12% activity	¹⁶³
Lysozyme	Poly (ethylene oxide)	After heating to 85 °C for 70 min, secondary structure was conserved (CD)	¹⁶⁴
Pullulanase	Butylacrylate-acrylic acid	At 40 °C, immobilized enzyme retained 40% activity, unprotected enzyme lost all activity	¹⁶⁵

1.4 Primary Objectives

The main objectives of this research thesis are:

- To establish a porous silica material “toolbox” with respective property database for detailed correlation between the physico-chemical properties of porous silica supports and protein adsorption (Chapter 3),
- To develop a robust and reproducible method to thermally stabilize IpaD and Lf in porous silica (Chapters 3 and 4),
- To model protein adsorption on porous silica using the Langmuir, Temkin and Freundlich isotherm models (Chapters 3 and 4),
- To determine the ideal non-ionic detergent to safely and effectively release protein from silica support (Chapter 4).

Chapter 2: Experimental Methods

2.1 Materials

The mesoporous silicas were obtained commercially: Sample 1 (SA1), Silica Gel 100-200 Mesh (Nominal), was acquired from EMD Millipore. Sample 2 (SA2) is the Silica Alumina Harshaw AL-1602 1/8" Pellet, silica-alumina (6%SiO₂/94%Al₂O₃) from Harshaw. Sample 3 (SA3) was acquired from Grace Chemical and is referred to as Davicat 57. Sample 4 (SA4) is Davison Silica Gel Grade 57 from Davison Chemical. Sample 5 (SA5) is a Silica Gel Catalyst from Davison Chemical. Samples 6-7 (SA6-SA7) are from PQ Corporation and are MS-3040 and MS-3030 Silica Support, respectively. Sample 8 (SA8) is Syloid 63 Micron Size Silica Gel from Grace Chemical. Sample 9 (SA9) is Silica Gel 100-200 Mesh from Fischer Scientific. Sample 10 (SA10) was obtained from Alfa Products and is known as Silica Gel Large Pore 58 Micron.

Phosphate Buffered Saline (PBS, 10X) solution was purchased from Fisher Scientific, and then diluted to 1X PBS (137 mM NaCl, 2.7 mM KCl, 8 mM Na₂HPO₄, 2 mM KH₂PO₄) with a pH of 7.4. *N-N*-dimethyldodecylamine *N*-oxide solution (LDAO, 30% in water) was purchased from Millipore Sigma, and it was diluted to 10% LDAO concentration with DI water. Tween 20, 40, and 80 and Triton X-100 were purchased from Sigma Aldrich and were diluted to either 3 vol%, 2 vol%, 1 vol%, or 0.5 vol% using DI water.

IpaD with a 6His tag was prepared essentially as described using standard immobilized metal affinity chromatography (IMAC).¹⁶⁶ Buffer exchange was carried out to prepare IpaD in 1×PBS solution, and SDS-PAGE gel was performed to assess protein purity. Bovine lactoferrin was obtained from Sigma Aldrich as a lyophilized powder and was diluted to 1-1.5 mg/mL in PBS.

2.2 IpaD Protein Expression and Purification

A single colony of *E. coli* expression cells Tuner (DE3) (Novagen) harboring the plasmid pET15b-His-IpaD was inoculated in 50 mL conical tubes containing 10 mL LB (lysogeny broth) media + 100 µg/mL ampicillin and grew overnight at 37 °C with shaking at 250 rpm. The overnight culture was transferred to a shaker flask containing 2 liters of TB (Terrific Broth) media + 100 µg/mL ampicillin and shook at 200 rpm at 37 °C until OD 600 nm reached about 0.7. The protein translation was induced with 0.4 mM IPTG at 37 °C for 3 hours. Cells were pelleted at 3500 relative centrifugal force (rcf) for 10 min and resuspended in Buffer A containing 50 mM Tris-HCl (pH 8.0) and 500 mM NaCl. Resuspended cells were frozen at -80 °C.

Frozen cells were thawed at room temperature and sonicated until resuspension was no longer viscous using the following cycle parameters: amplitude: 50%, pulse length: 30 sec, number of pulses: 12, while incubated on ice for >1 min between pulses. A soluble fraction was obtained by centrifuging the cell lysate at 45450 rcf 30 minutes at 4 °C. The soluble lysate was loaded to a 5 ml HisTrap™ High Performance pre-packed column from GE HealthCare on an AKTA Xpress chromatography system. Protein was eluted with a gradient of Buffer B (Buffer A+ 500 mM imidazole) from 10% to 100%. Elution peak fractions were pooled and applied to a Superdex S75 Increase10/300 GL column equilibrated with PBS on an AKTA Pure. Protein concentration was determined either by Bradford assay or using the extinction coefficient of 0.95 g/L for each unit of absorbance at 280 nm. The yield of 10 to 20 mg of protein was obtained for each protein preparation. The purified protein was concentrated to 1.0 to 1.5 mg/mL, flash frozen in liquid nitrogen, and stored in a -80 °C freezer.

2.3 Physical Characterization

A Micromeritics ASAP 2020 Plus instrument was used to measure the accessible specific surface area (SSA), pore volume (PV), and the pore size distribution (PSD) of samples SA8 to SA10 (*vide infra*) via N₂ adsorption at -196 °C. Samples were degassed under vacuum for 12 hours at 150 °C prior to analysis. The sample assembly was composed of the sample tube, filler rod, and for analysis, an isothermal jacket that controlled liquid N₂ level. Forty-six, equally spaced, adsorption and desorption measurements were taken between $0.05 < P/P_0 < 0.994$ to define the full isotherm. Adsorption data were analyzed using the Barrett-Joyner-Halenda (BJH) method.¹⁶⁷ The BJH method used the Kelvin equation with a cylindrical pore model assumption and the Harkins and Jura thickness equation. The average pore diameter was computed using a weighted average. The accessible PV and SSA data exclude contributions from pores below 50 Å that are not accessible by IpaD and Lf for adsorption.

2.4 Adsorption

Silica particles were crushed and sieved to a particle size of 90 to 150 µm. A 0.7 mL sample of Lf or IpaD (1.5 mg/mL in 1×PBS buffer) was added to 30.0 mg of mesoporous silica in a round bottom, 2 mL microcentrifuge tube. The solution was mixed on a ThermoMixer® at 950 rpm and 25 °C for 20 hours. The samples were centrifuged at 14,800 rpm for 4 minutes at ambient temperature (20-21 °C) to separate the silica-protein complex from the supernatant. The solution depletion method was utilized to determine the amount of protein transferred from the solution to the mesoporous silica so that the supernatant concentration could be used to determine the amount of protein adsorbed. The concentration of the supernatant was measured using a Nanodrop™ 2000 UV-Vis spectrophotometer at a wavelength of 280 nm with an extinction coefficient of 36900 M⁻¹

$^1\text{cm}^{-1}$ and $99415 \text{ M}^{-1}\text{cm}^{-1}$ for IpaD and Lf, respectively.¹⁶⁸ The difference in initial and supernatant concentrations of Lf were used to quantify the percent adsorption using Equation 2.1:

$$\text{Percent adsorption} = \left(1 - \frac{\text{Supernatant IpaD concentration}}{\text{Initial IpaD concentration}}\right) * 100 \quad (2.1)$$

2.5 Heating

The silica samples with adsorbed protein were placed on a ThermoMixer® at $95 \text{ }^\circ\text{C}$ for 2 hours. A sample of native protein in 1X PBS was heated at the same temperature for 2 hours for a denatured control. The samples were allowed to cool to room temperature ($20\text{-}21 \text{ }^\circ\text{C}$) for at least 30 minutes before desorption was initiated.

2.6 Desorption

To detach the proteins from the silica, 0.6 mL of a desorbing agent was added to each sample. The desorbing agent consisted of different percentages, between 0.5-3 vol %, of Tween 20, Tween 40, Tween 80, and Triton X-100 or 10% LDAO in DI water. The volume percent (vol %) was defined as the volume of detergent divided by the total volume of solution (detergent + water). When diluting the detergents to the desired concentrations, the detergents and DI water were filtered using a $250 \text{ }\mu\text{m}$ sterile filter. Next, the samples were mixed at 950 rpm and $25 \text{ }^\circ\text{C}$ for 24 hours. Finally, the samples were centrifuged at 14,800 rpm for 1 minute and the percent protein recovery was calculated using Equation 2.2:

$$\text{Percent recovery} = \left(\frac{\text{Mass of desorbed Lf}}{\text{Initial mass of Lf}}\right) * 100 \quad (2.2)$$

2.7 TEM Imaging

A TECNAI FT20 Field Emission Transmission Electron Microscope (TEM) equipped with a 200 kV electron source and a charge-coupled device (CCD) was used to image the silica. An energy

dispersive X-ray spectroscopy (EDX) detector was used to investigate the IpaD adsorption on mesoporous silica materials. Before analysis, IpaD was immobilized on either a mesoporous silica sample or on gold nanoparticles (AuNP), which were subsequently deposited on to a silica sample and dried under vacuum. The AuNP were synthesized via the procedures described in the literature.¹⁶⁹ All controls were treated under the same conditions. Samples were cast on carbon-coated copper grids from aqueous suspensions and analyzed on a cryogenic stage.

2.8 Circular Dichroism Spectropolarimetry

A Jasco J-1500 Circular Dichroism Spectrophotometer instrument was used to evaluate the secondary structure of chiral protein samples at a temperature of 15 °C over a wavelength range of 190-260 nm. Before CD measurements were performed, the samples desorbed from silica were diluted to 0.2-0.5 mg/mL in the respective detergent, which is within the required concentration range. The denatured protein sample was analyzed in CD using 1X PBS, while the native protein and samples removed from silica were analyzed in the detergent solution. The nitrogen flowrate was set at 30 standard cubic feet per hour (scfh). A 1.0 cm path length quartz cuvette was cleaned using 2% Hellmanex[®] II solution to remove any remaining biological specimen from previous runs. The cuvettes were thoroughly washed with milli-Q[®] water before purging with nitrogen to remove any remaining moisture. The cuvettes were filled with 250 μ L of sample and placed in the instrument. The raw data from CD was reported in Q (mdeg). This was converted to molar ellipticity to account for the concentration of the sample and protein properties using Equation 2.3

$$\theta = \frac{Q \cdot 100 \cdot MW}{C \cdot l \cdot n \cdot 1000} \quad (2.3)$$

MW is the molecular weight of the protein sample and n is the number of amino acids. For IpaD, these values are 38825.29 Da and 352, respectively. For bovine Lf, these values are 75181.79 Da

and 681, respectively. The concentration (C) of the sample in mg/mL was measured at 280 nm using UV-Vis absorbance spectrophotometry. The length (l) of the quartz cuvette is 1.0 cm for the J-1500 instrument.

Chapter 3: Case Study 1-Invasion Plasmid Antigen D (IpaD) Adsorption and Thermal Stabilization

3.1 Introduction

Shigellosis (bacillary dysentery) is a gastrointestinal disease that causes over a million deaths annually,¹⁷⁰ especially in developing countries and among children.¹⁷¹ *Shigella flexneri*, the bacteria that causes Shigellosis, is spread through the fecal-oral route and only a very low dose is required for infection.¹⁷² *S. flexneri* is acid-tolerant, and once it reaches the large intestine, it is transcytosed through M cells.^{170,173} At this point, the bacteria induces apoptosis in macrophages and invades epithelial cells using a type-III secretion system (T3SS).¹⁷⁴ Invasion plasmid antigen D (IpaD) has a crucial role in T3SS, as it controls the secretion of IpaB and IpaC. All three Ipa proteins must be released for epithelial cell invasion.¹⁷⁵ Currently, there is no existing vaccine for shigellosis¹⁷⁶ despite extensive attempts to formulate a vaccine^{177,178,179} and previously developed vaccines have shown high reactogenicity in human trials.¹⁸⁰ IpaD is a promising target for shigellosis vaccine development since it has already been demonstrated that IpaD antibodies are present in serum from infected patients.^{181,182}

IpaD has 352 residues and a molecular weight of 38825.29 Da.¹⁶⁸ Circular dichroism (CD) and Fourier transform infrared (FTIR) spectroscopy have shown that IpaD is predominantly an α -helical protein and this was later confirmed from its crystal structure.^{174,183} IpaD has a high thermal stability with denaturing occurring above 80 °C.

Approximately 13% of IpaD is made up of serine amino acids as the most abundant residue,³³ which are able to form hydrogen bonds via their hydroxymethyl groups at the surface of the silica as shown in Figure 3.1. Furthermore, 9.1% of IpaD is composed of asparagine and 7.7% is threonine. Asparagine can accept or donate two hydrogen bonds with its amide group, and threonine can form one hydrogen bond with its hydroxyl group. Due to the negative surface of

silica at neutral pH, it is expected that the arginine and lysine positively charged residues will further stabilize IpaD in the pores and surface of the silica with electrostatic interactions. Our working hypothesis is that amino acids with hydrogen bonding capability are primarily responsible for the adsorption interactions of IpaD within mesoporous silica and prevent the protein from denaturing.

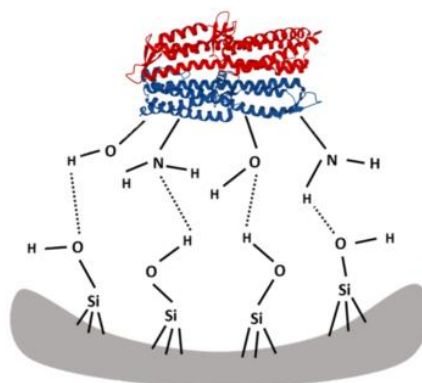


Figure 3.1. Proposed hydrogen bonds between IpaD residues and mesoporous silica surface

3.2 Physicochemical Characterization

The physicochemical properties of seven mesoporous silica materials were characterized to generate a “tool box” with a range of physicochemical properties. The material selection criteria for the immobilization of IpaD was based on the physico-chemical properties of the support (average pore diameter, accessible pore volume and surface area, and surface chemistry (i.e. functional groups)) with those of the IpaD protein. The physico-chemical properties of selected mesoporous silica materials used as supports for the protein thermal-stabilization studies are provided in Table 3.1. The thermogravimetric analysis curves for each silica and FTIR spectra for IpaD are provided in Appendix A. The most relevant results can be observed between 190-400 °C, where the results are consistent with a decrease in the level of surface hydroxylation, while the isolated singles, geminals, and vicinal silanol groups are still present. Silicas with higher percent weight loss during have a higher degree of hydroxylation at room temperature; therefore, these

silicas have a higher affinity for hydrogen bonding and hydrophilic interactions during the adsorption process.

Table 3.1. BJH physicochemical characterization of selected mesoporous silica materials (Samples SA1- SA10). Pore size distributions can be found in Appendix B.

Silica Sample	Average Pore Diameter (nm)	Pore Volume (cm³/g)	Surface Area (m²/g)
Silica Sample 1 (SA1)	3.9 ± 1.5	0.07 ± 0.01	67.4 ± 3.3
Silica Sample 3 (SA3)	15.0 ± 1.5	1.28 ± 0.01	333.2 ± 3.3
Silica Sample 4 (SA4)	17.7 ± 1.5	1.41 ± 0.01	319.3 ± 3.3
Silica Sample 5 (SA5)	24.2 ± 1.5	2.18 ± 0.01	370.7 ± 3.3
Silica Sample 6 (SA6)	30.2 ± 1.5	3.78 ± 0.01	300.0 ± 3.3
Silica Sample 7 (SA7)	36.3 ± 1.5	2.87 ± 0.01	286.1 ± 3.3
Silica Sample 8 (SA8)	2.34 ± 1.5	1.18 ± 0.01	911.1 ± 3.3
Silica Sample 9 (SA9)	5.29 ± 1.5	3.03 ± 0.01	2673 ± 3.3
Silica Sample 10 (SA10)	8.21 ± 1.5	1.42 ± 0.01	672.7 ± 3.3

3.3 Effect of silica pore diameter on IpaD adsorption

After improving the protocol to adsorb IpaD onto various silica materials, the material properties with the most impact on the adsorption efficiency of IpaD were investigated. Our results show that the successful adsorption of IpaD protein is strongly influenced by the pore diameter of the silica material (Figure 3.2). The dimensions of IpaD are ~3 nm in diameter and ~8 nm in length;¹⁷³ therefore, accessible pores were defined to be just larger than the diameter of IpaD at ≥ 5 nm to allow for the possibility of IpaD travelling into silica pores lengthwise. The percent IpaD adsorbed

is defined as the amount of IpaD that was adsorbed onto the silica over the total IpaD added in solution.

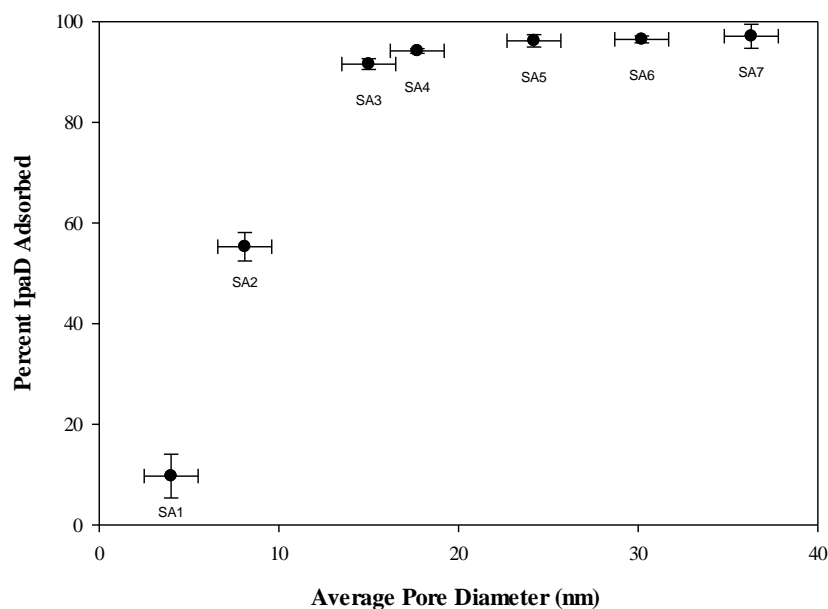


Figure 3.2. Average percent of IpaD adsorbed to mesoporous silica materials (SA1 to SA7) as a function of average pore diameter (nm)

The adsorption process is governed by electrostatic interactions and hydrogen bonding between the hydroxyls on the silica surface and the functional groups of the amino acid side chains on IpaD.³³ The most abundant amino acid in IpaD is serine, which makes up 13% of the structure. This creates the potential for a high level of hydrogen bonding between serine residues and the silica surface. There is a strong correlation between the average pore diameter of the silica to the percent of IpaD adsorbed (Figure 3.2). For example, silica sample SA3 has a pore diameter of 15 nm and adsorbs an average of 91.6% IpaD, while silica sample SA1 has a pore diameter of 3.9 nm and adsorbs an average of 9.7% IpaD. Silicas with a pore diameter greater than 15 nm are expected

to adsorb more than 90% IpaD (Figure 3.2). The pore volume of the silica materials followed a similar trend to the average pore diameter as shown in Figure 3.3.

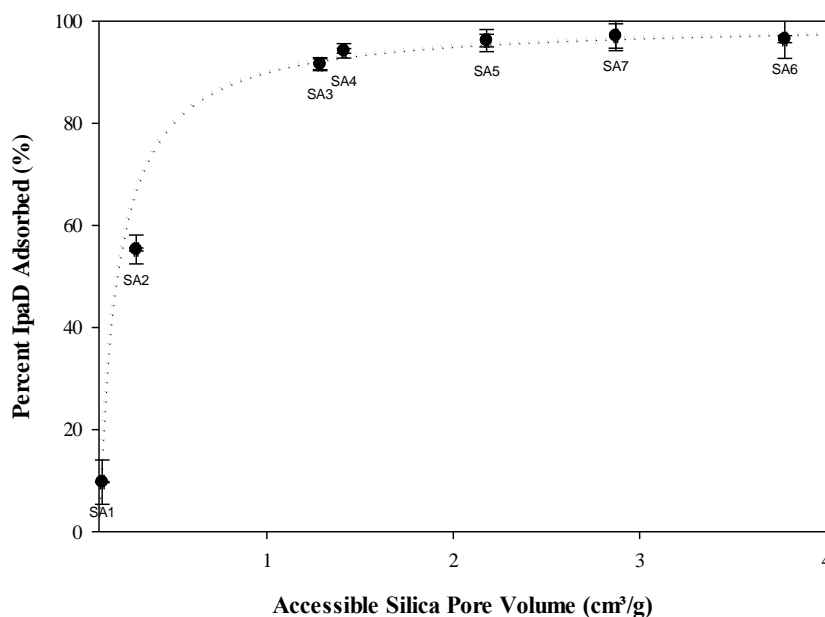


Figure 3.3 Percent of IpaD adsorbed to silica samples as a function of silica pore volume

Therefore, silicas with larger pore diameters and pore volumes tend to adsorb more IpaD. This indicates that the proteins are not only adhering to the external surface of the silica, but also being adsorbed into the interior of the larger silica pores. The enhanced thermostability of IpaD when it is attached to silica during heating further supports the hypothesis that IpaD is confined within the pores during adsorption.

3.4 Langmuir Model Derivation

The Langmuir adsorption isotherm assumes that all surface sites are the same, that all adsorption occurs on vacant sites, that the adsorbate-adsorbate interactions are negligible, and that all sites are either vacant or occupied.¹⁸⁴ Furthermore, the Langmuir adsorption model assumes

monolayer chemisorption. To derive the Langmuir model, the adsorption equation is written out in Equation 3.1:



S refers to an empty site and IpaD-S refers to the adsorbed IpaD. The rate of adsorption is as follows in Equation 3.2:

$$R_{ads} = k_{ads}C_{IpaD,free}C_s - k_{des}C_{IpaD,ads} \quad (3.2)$$

If K is defined by Equation 3.3 and equilibrium is assumed (Equation 3.4):

$$K = \frac{k_{ads}}{k_{des}} \quad (3.3)$$

$$0 = k_{ads}C_{IpaD,free}C_s - k_{des}C_{IpaD,ads} \quad (3.4)$$

$$KC_{IpaD,free}C_s = C_{IpaD,ads} \quad (3.5)$$

A site balance is performed to determine an expression for C_s .

$$C_m = C_s + C_{IpaD,ads} \quad (3.6)$$

C_m is the total number of sites, or the maximum monolayer coverage. Solving for C_s :

$$C_s = C_m - C_{IpaD,ads} \quad (3.7)$$

Substituting $C_{IpaD,ads}$ from Equation 3.5 into Equation 3.7:

$$C_s = C_m - KC_{IpaD,free}C_s \quad (3.8)$$

Solving for C_s :

$$C_s = \frac{C_m}{1+KC_{IpaD,free}} \quad (3.9)$$

Plugging in C_s from Equation 3.9 into Equation 3.5 results in the Langmuir adsorption equation.

$$C_{IpaD,ads} = \frac{KC_mC_{IpaD,free}}{1+KC_{IpaD,free}} \quad (3.10)$$

3.5 Langmuir Adsorption Isotherm Modeling

The experimentally determined adsorption capacity for silica sample SA3 was found using

$$q = \frac{(C_i - C_f)}{S} \times V \quad (3.11)$$

where q (mg/g) is the adsorption capacity of silica with respect to IpaD at equilibrium, C_i and C_e are the initial and final concentration (mg/mL) of IpaD in PBS solution, respectively, S is the mass silica adsorbent used (g), and V is the volume of solution (mL). To determine the maximum IpaD adsorption on a mesoporous silica, the IpaD adsorption isotherm was fit using the Langmuir adsorption model. The experimental data and Langmuir model were plotted (Figure 3.4) using Equation 3.10. Appendix C includes details on the error calculation for all adsorption isotherms.

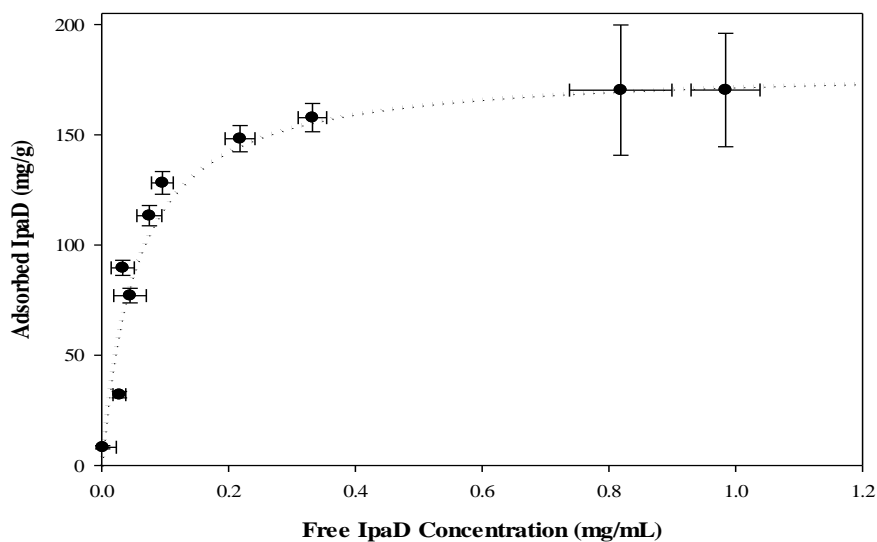


Figure 3.4. Adsorption isotherm for silica sample SA3 using the Langmuir model

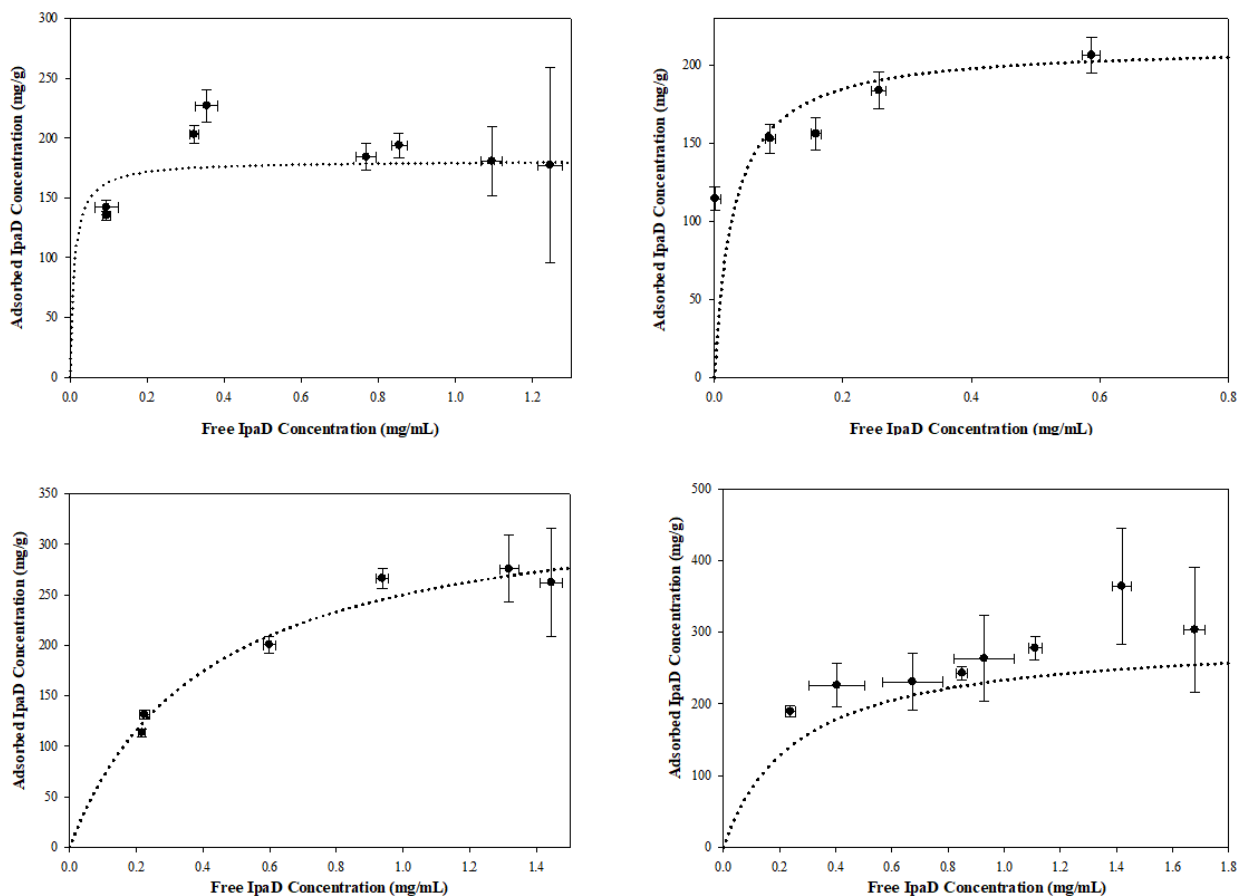


Figure 3.5. Adsorption isotherms using the Langmuir model for silica gel SA4 (top left), SA5 (top right), SA6 (bottom left) and SA7 (bottom right)

Linearizing Equation 3.10, to obtain Equation 3.12:

$$\frac{C_{IpaD,ads}}{C_{IpaD,free}} = \frac{1}{KC_m} + \frac{C_{IpaD,free}}{C_m} \quad (3.12)$$

The linearized form of the Langmuir model was plotted (Figure 3.6), and the maximum monolayer coverage was determined to be 181 mg/g and the equilibrium rate constant was determined to be 18 mL/mg.

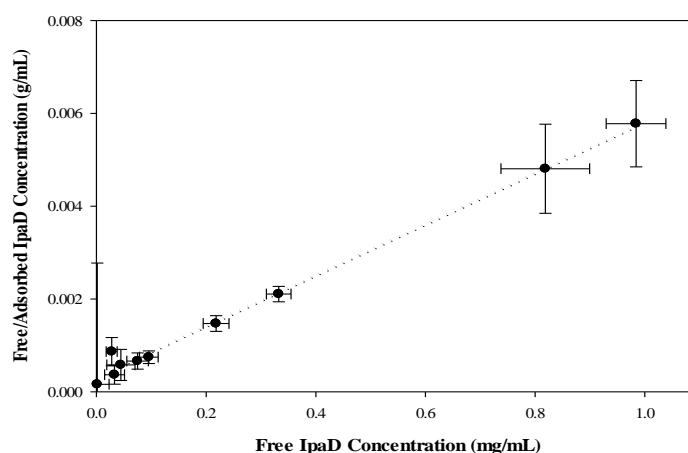


Figure 3.6. Linearized adsorption isotherm for silica sample SA3 using the Langmuir model ($R^2=0.994$)

From the close fit of the experimental data to the Langmuir model, it is possible to deduce that the adsorption of IpaD onto mesoporous silicas is occurring as a monolayer adsorption mechanism (Figure 3.6). Using a unit surface area for IpaD of $112.8 \text{ nm}^2/\text{protein}$ (based on using the largest two-unit cell parameters of 10.07 and 11.28 nm)¹⁸⁵ and a molecular weight of 39 kDa it is possible to convert the maximum monolayer coverage from mg IpaD/g silica to $\text{m}^2 \text{ IpaD/g silica}$.

$$\frac{181 \text{ mg IpaD}}{\text{g silica}} \times \frac{\text{mol IpaD}}{3.9 \times 10^7 \text{ mg}} \times \frac{6.02 \times 10^{23} \text{ proteins}}{1 \text{ mol}} \times \frac{112.8 \text{ nm}^2}{\text{protein}} \times \frac{(1 \text{ m})^2}{(1 \times 10^9 \text{ nm})^2} = \frac{316 \text{ m}^2 \text{ IpaD}}{\text{g silica}} \quad (3.13)$$

The maximum monolayer coverage value of $316.3 \pm 8.9 \text{ m}^2/\text{g}$ calculated from the Langmuir modeling to the accessible surface area of $333.2 \pm 3.3 \text{ m}^2/\text{g}$ (Table 3.1) obtained from BJH measurements are in good agreement, as are the values for silica samples SA4 and SA5 (Table 3.2).

Table 3.2. Comparing nitrogen BJH surface area and Langmuir modeling IpaD surface area for silica samples SA3-SA5.

Silica Sample	N_2 Surface Area (m^2/g)	IpaD Surface Area (m^2/g)
SA3	333.2 ± 3.3	316.3 ± 8.9
SA4	319.2 ± 3.3	316.6 ± 11.4
SA5	370.2 ± 3.3	371.9 ± 20.2

For silicas with larger pore diameters (SA6 and SA7) the maximum monolayer coverage calculated from the Langmuir model is significantly different than the BJH accessible surface area (Table 3.3). However, if the IpaD unit cell volume is used instead of the IpaD unit cell surface area in Equation 3.13, it is possible to calculate the maximum coverage in terms of volume.

$$\frac{294 \text{ mg IpaD}}{\text{g silica}} \times \frac{\text{mol IpaD}}{3.9 \times 10^7 \text{ mg}} \times \frac{6.02 \times 10^{23} \text{ proteins}}{1 \text{ mol}} \times \frac{630.0 \text{ nm}^3}{\text{proteins}} \times \frac{(1 \text{ cm})^3}{(1 \times 10^7 \text{ nm})^3} = \frac{2.87 \text{ cm}^3 \text{ IpaD}}{\text{g silica}} \quad (3.14)$$

Table 3.3. Comparing nitrogen BJH surface area and pore volume to Langmuir modeling IpaD surface area and pore volume for silica samples SA6 and SA7. Langmuir plots for silica samples SA6 and SA7 are provided in Appendix D.

Silica Sample	N ₂ Accessible Surface Area (m ² /g)	IpaD Surface Area	N ₂ Volume (cm ³ /g)	IpaD Volume (cm ³ /g)
SA6	300.0 ± 3.3	603.4 ± 43.5 m ² /g	3.78 ± 0.01	3.49 ± 0.23
SA7	286.1 ± 3.3	514.2 ± 46.8 m ² /g	2.87 ± 0.01	2.87 ± 0.26

The IpaD surface area for these two silicas is greater than the nitrogen surface area, suggesting that multilayer adsorption may be occurring rather than monolayer adsorption. IpaD volume measurements are in good agreement with the nitrogen BJH volume measurements, supporting the hypothesis that adsorption is multilayer (i.e. bilayer) in the silicas with pore sizes larger than 25 nm. When performing the washing step on silica samples SA6 and SA7, the IpaD concentration in the supernatant varied considerably (Figure 3.7). This behavior is not observed with silicas with smaller pore sizes (SA3, SA4, and SA5), where the IpaD concentration in the wash supernatant is negligible. The hypothesis is multiple IpaD molecules are adsorbed in the larger pores and there are fewer hydrogen bonds between the silica and IpaD; therefore, the interaction is weaker and the IpaD is removed by washing.

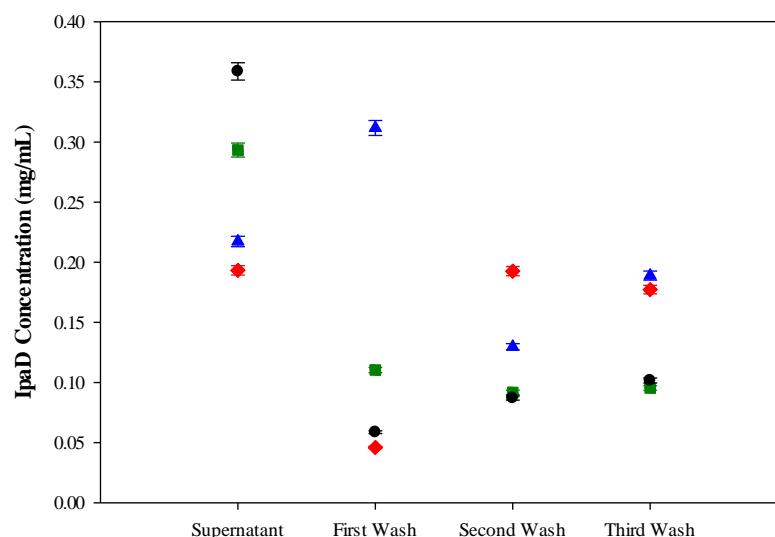


Figure 3.7. IpaD concentration after subsequent washes for sample 1 (triangles), sample 2 (diamonds), sample 3 (squares) and sample 4 (circles). Initial silica masses of samples 1-4 are 8.3 mg, 7.0 mg, 6.3 mg and 3.0 mg, respectively. Initial IpaD concentration is 1.95 mg/mL for all samples, silica is SA7.

The solution depletion method measures the adsorbed IpaD concentration by subtracting the amount of IpaD in the supernatant (i.e. wash) from the original IpaD concentration. Comparing the Langmuir isotherm of silica sample SA3 to the corresponding isotherm for silica sample SA1 (pore diameter of 3.9 nm), it is evident that the adsorbed IpaD concentration for SA1 is essentially negligible in comparison to the adsorbed IpaD concentration for SA3 (Figure 3.8). The behavior displayed by SA1 is expected, since its pore diameter is smaller (3.9 nm) than IpaD's external dimensions (largest two-unit cell parameters of 10.07 and 11.28 nm), which limits IpaD adsorption. If IpaD was adhering to the surface of SA1 then the adsorbed IpaD (mg IpaD/g sample) would be significantly higher than shown in Figure 3.8. This confirms that the IpaD is primarily adsorbed (99+%) in the pores and not on the surface of the silica. Silica sample SA2 (pore diameter of 8.1 nm) followed the same behavior as silica sample SA1 and the adsorption isotherm for silica sample SA2 is shown in Figure 3.9.

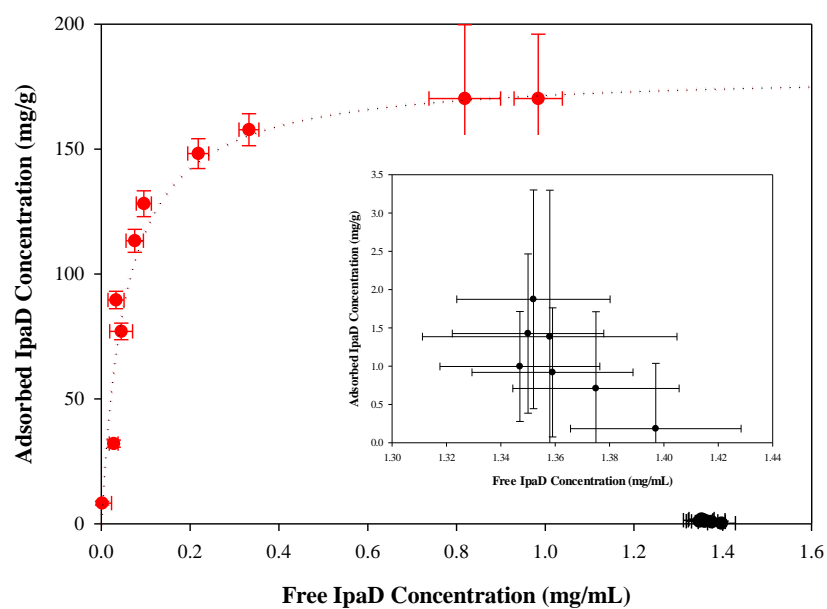


Figure 3.8. Comparison of the adsorption isotherm for silica sample SA1 (black) and the adsorption isotherm for silica sample SA3 (red). Inset is expanded view of silica sample SA1.

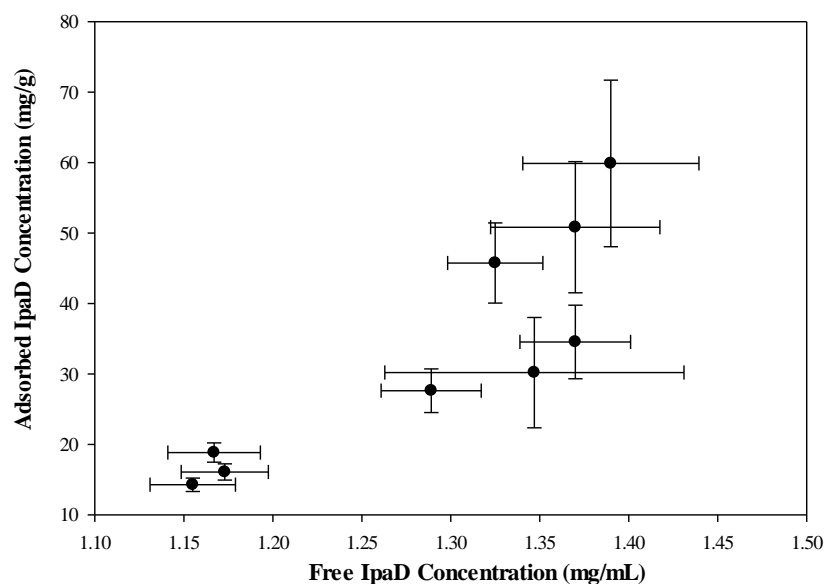


Figure 3.9. Adsorption isotherm for silica sample SA2

Overall, if the average pore size is less than about 15 nm, the IpaD cannot physically fit inside the pore and the adsorption is negligible (SA1 and SA2). If the average pore sizes are approximately 15 to 25 nm then monolayer coverage is achieved and the IpaD cannot be removed via washing with PBS due to the hydrogen bond network formed with the silica surface (SA3, SA4, and SA5). If the average pore size is larger than about 25 nm the adsorption is multilayer coverage and the IpaD can be easily removed via washing with PBS due to a less developed hydrogen bond network (SA6 and SA7). Figure 3.10 provides a schematic of the three types of pore interactions with IpaD.

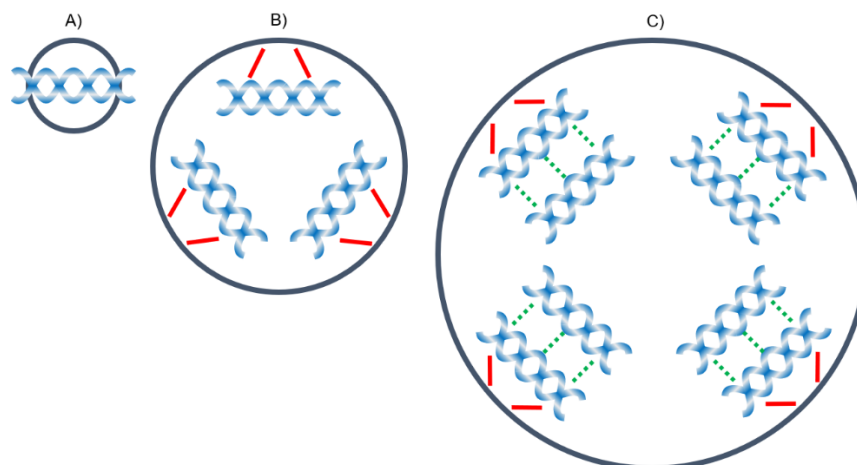


Figure 3.10. Comparison of the three types of pores interactions with IpaD, (A) pore size less than 15 nm (e.g. SA1 and SA2), IpaD does not fit into pore, (B) pore size between 15 to 25 nm (e.g. SA3, SA4, and SA5), monolayer coverage, hydrogen bonds depicted by solid red line, (C) pore size larger than 25 nm (e.g. SA6 and SA7), multilayer coverage, protein-protein interactions depicted by dotted green line.

3.6 Comparing the Langmuir Model to Freundlich and Temkin Models

The adsorption data were also compared to both Freundlich and Temkin adsorption models. The Freundlich model assumes multilayer adsorption, interactions among adsorbed molecules, and reversible adsorption. The linearized form of the Freundlich model is as follows:

$$\log C_{IpaD,ads} = \log K_F + \frac{1}{n} \log C_{IpaD,free} \quad (3.15)$$

where K_F is the adsorption capacity (L/mg) and $1/n$ is the adsorption intensity.

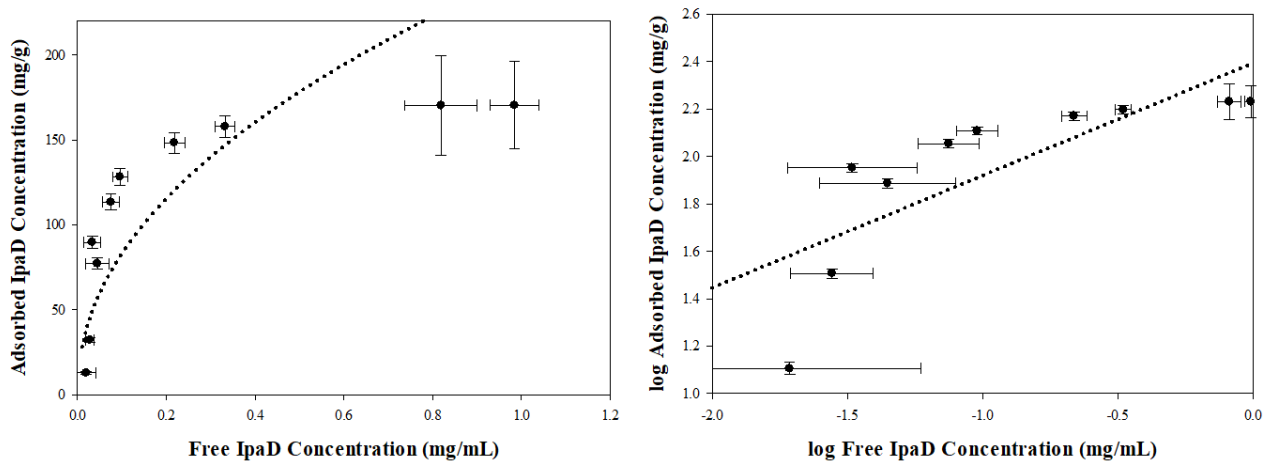


Figure 3.11. Freundlich adsorption isotherm (left); linearized isotherm for silica sample SA3 using the Freundlich Model ($R^2=0.622$) (right)

The Freundlich and Temkin models assume multilayer adsorption and considers the effects of adsorbate interactions. The Temkin model also assumes that the heat of adsorption of molecules in a layer has a linear decrease as surface coverage increases. The linearized form of the Temkin model is as follows:

$$C_{IpaD,ads} = \frac{Rt}{b} \ln K_T + \frac{RT}{b} \ln C_{IpaD,free} \quad (3.16)$$

where b and K_T are Temkin constants.

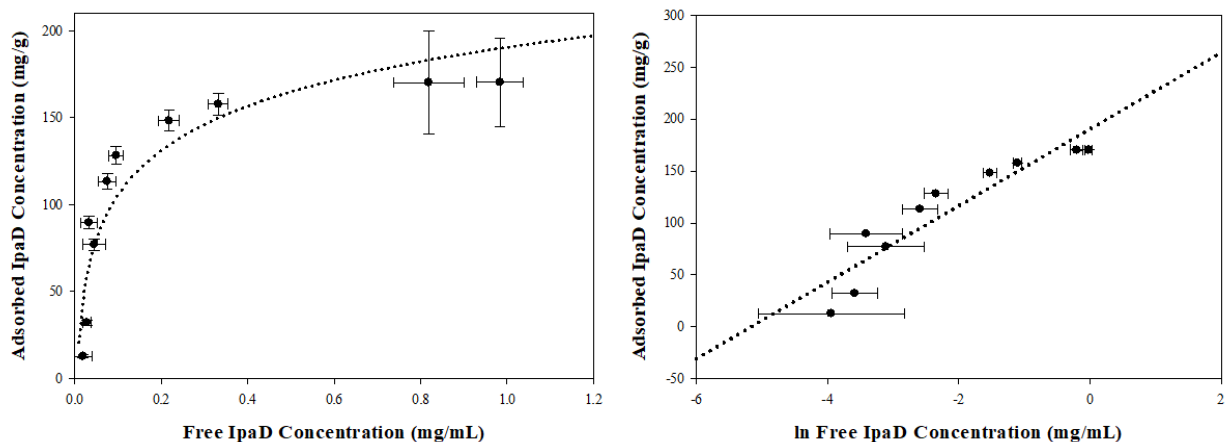


Figure 3.12. Temkin adsorption isotherm (left); linearized isotherm for silica sample SA3 using the Temkin Model ($R^2=0.856$) (right)

Based on the Langmuir, Freundlich, and Temkin models (Figures 3.4, 3.5, 3.6, 3.11 and 3.12), it is evident that the Langmuir model is the best fit of the experimental data. The R^2 value for the Langmuir model is 0.994, almost a perfect fit, while the R^2 values for the Freundlich and Temkin models are 0.622 and 0.856, respectively. From the evaluation and comparison of the different models, it is possible to conclude that adsorption is indeed monolayer, irreversible adsorption. Freundlich and Temkin plots for silica samples SA4-SA7 are provided in Appendix D.

3.7 TEM Characterization

The distribution of IpaD on silica sample SA4 was characterized using TEM/EDX. A TEM image of the silica control (Figure 3.13A), revealed a random structure and evidence of Si, O, C, and Cu, from the porous silica and the C-Cu grid. Furthermore, there was no detectable sulfur content in the silica control, such that any sulfur detected in the IpaD-silica complex comes from the single cysteine and methionine residues in IpaD.

IpaD was conjugated to AuNP in a 1:1 ratio before adsorbing IpaD-AuNP on silica sample SA4. The cysteine residue in IpaD has a high affinity towards gold, which makes it an ideal location for gold nanoparticle attachment.¹⁸⁶ AuNPs possess adjuvant properties that reduce toxicity, enhance

the immunogenic activity, and provide stability during storage.¹⁸⁷ In addition, gold is a heavy metal that easily deflects electron beams in TEM, making IpaD attached to gold simpler to locate in a silica sample. The average AuNP size was determined to be ca. 19.5 nm (Figure 3.13B). The AuNP-IpaD complex adsorbed on silica sample SA4 is shown in a STEM image (Figure 3.13C). The blue area was characterized using EDX elemental scans for sulfur (Figure 3.13D) and gold (Figure 3.13E). Significant overlap in the EDX S and Au maps is consistent with the 1:1 S-Au linkage.

A STEM was also performed without gold nanoparticle attachment for the adsorbed IpaD in silica sample SA4. The lighter imaged material may be evidence of IpaD on the surface and in the pores. To verify this hypothesis, an EDX elemental scan was obtained for sulfur (Figure 3.13G). The molecular formula of IpaD is $C_{1686}H_{2682}N_{474}O_{557}S_{10}$. The EDX sulfur content in this sample area was consistent with the atomic composition of sulfur in IpaD, which confirms the presence of IpaD on the surface of the silica, even in the absence of AuNP. The even distribution of sulfur in the EDX (Figure 3.13H) is evidence that IpaD is evenly distributed in the adsorption process. Langmuir modeling also suggests that an even monolayer distribution of IpaD is present across the surface and in the pores. Figure 3.14 and Figure 3.15 include EDX data for the control silica (without IpaD) and the silica-IpaD complex to confirm the sulfur count comes solely from the IpaD and there is no sulfur content in the silica.

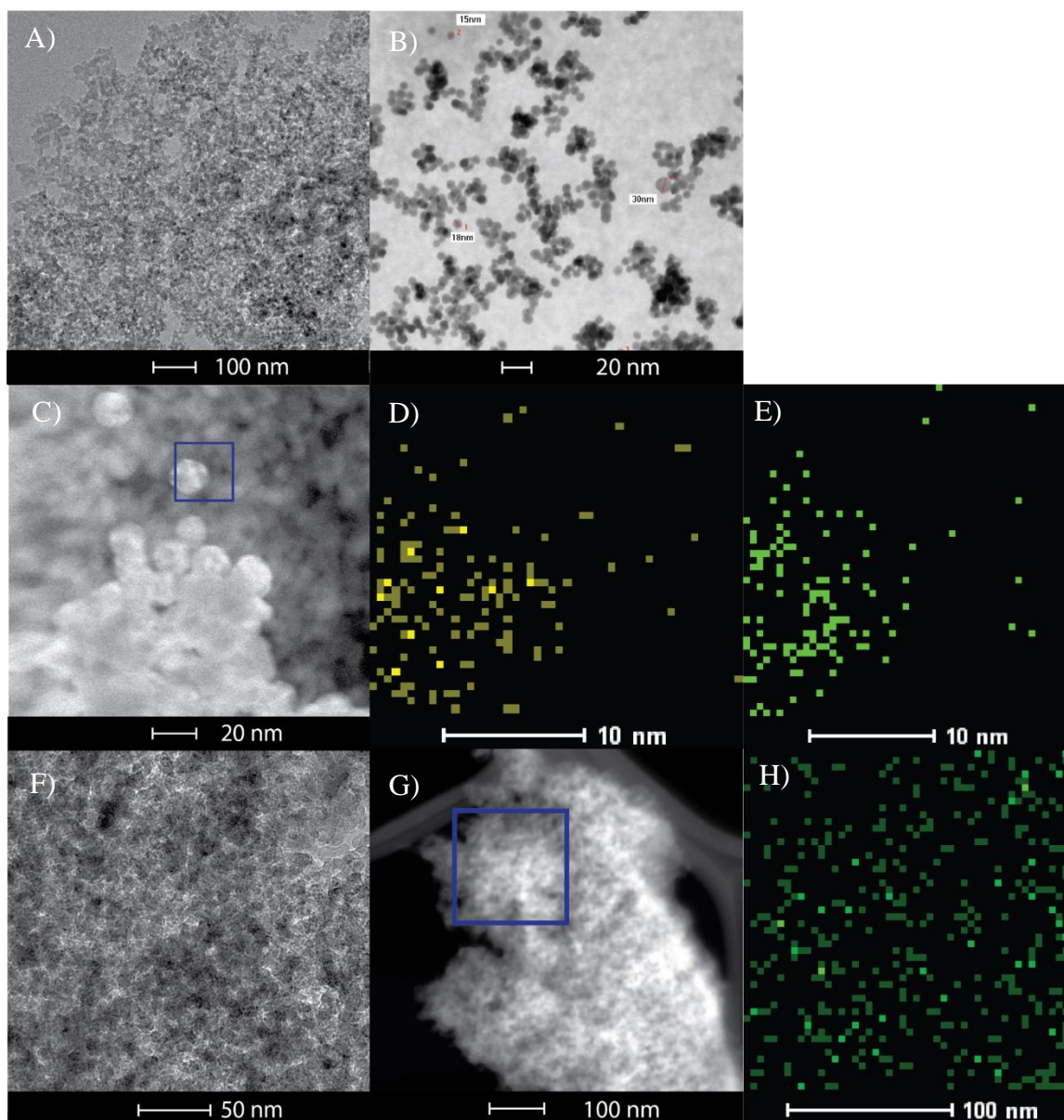


Figure 3.13 A) TEM image for silica sample SA4 as a control to monitor IpaD adsorption; B) TEM image of AuNP average size; C) STEM image of IpaD-AuNP adsorbed in silica sample SA4, blue box is EDX scan location; D) EDX S-K spectral scan of Figure 9C; E) EDX Au-L spectral scan of Figure 9C; F) STEM image of IpaD adsorbed in silica sample SA4; G) STEM image of IpaD in silica sample SA4, blue box is EDX scan location; H) EDX S- K spectral scan of Figure 9G.

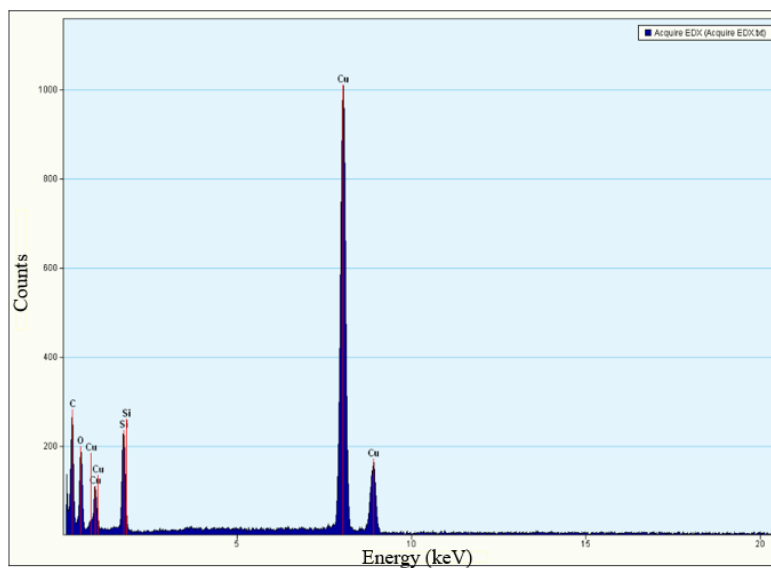


Figure 3.14. EDX scan of silica control (SA4)

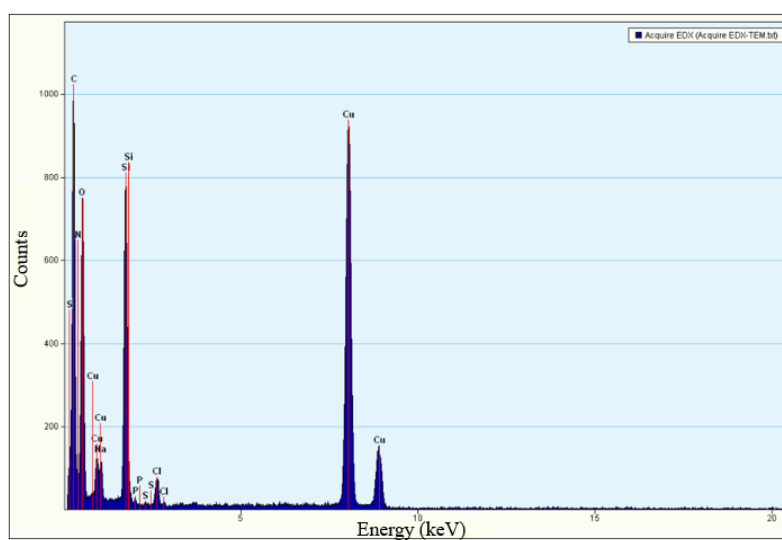


Figure 3.15. EDX scan of IpaD adsorbed on silica SA4

3.8 Desorption

For each of the characterized silica samples, the amount of IpaD desorbed in LDAO solution was compared with the original IpaD adsorbed (Figure 3.16).

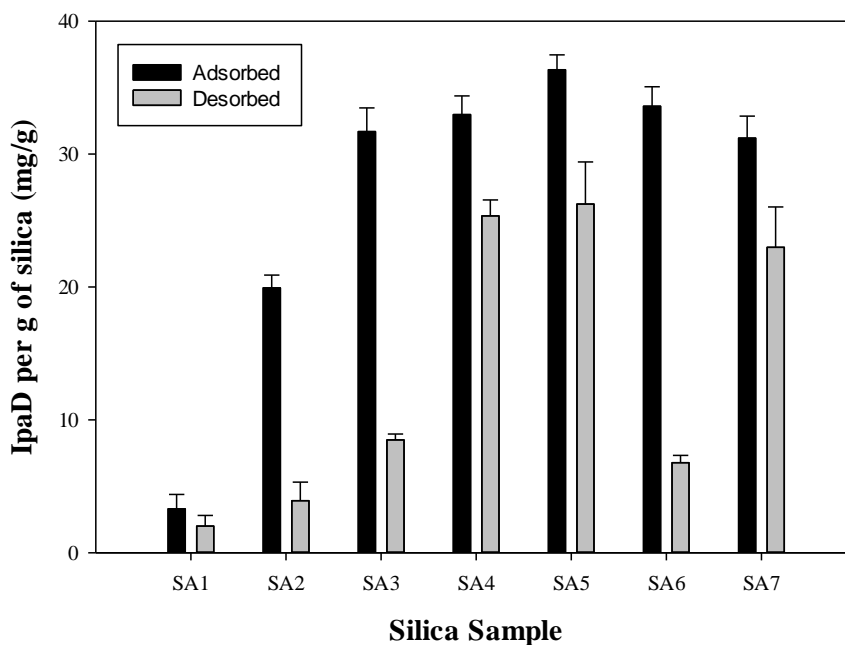


Figure 3.16. Comparison of adsorption capacity (mg/g) to IpaD released from silica samples during desorption (mg/g) for silica samples SA1-SA7

In general, silicas that had a larger pore diameter and pore volume tended to release more of the adsorbed proteins upon the desorption process. However, silica sample SA6 does not follow this trend. This could be due to SA6 having the largest accessible pore volume of $3.78 \pm 0.01 \text{ cm}^3/\text{g}$ with a high surface area of $300.0 \pm 3.3 \text{ m}^2/\text{g}$, which could be linked to increased hydrogen bonding, resulting in less IpaD removal with LDAO. While strong binding affinity is important for protein immobilization during transportation of a vaccine, the protein must also be easy to release in solution for a high vaccine delivery. For this reason, silica samples SA4, SA5, and SA7 make desirable candidates for vaccine transportation and delivery due to these desorption studies.

LDAO is a strong surfactant with a dodecyl alkyl tail and a zwitterionic tail. It is highly hydrophilic and forms hydrogen bonds with water molecules that are stronger than hydrogen bonding of water molecules themselves with an energy of 50 kJ/mol .¹⁸⁸ Due to these properties, LDAO can easily

break the hydrogen bonds that attach IpaD to the surface of a silica. It is possible that LDAO could form micelles around IpaD during the desorption process with its zwitterionic head.

3.9 IpaD secondary structure

To assess whether the adsorption into silica-based supports protects the protein against high temperatures, the IpaD adsorbed onto the silica sample SA4 was heated to 95 °C for 2 h, desorbed from the support, and then analyzed by CD. Non-adsorbed (native) IpaD that was not heated was used as control. The CD analyses demonstrate that the adsorbed IpaD after the heat treatment displays similar double minima (208 and 222 nm) in the CD spectrum as seen in the native unheated IpaD and is indicative of a substantial α -helical component.

The purpose of this study was to demonstrate that mesoporous silica materials improve the thermostability of IpaD. It is evident (Figure 3.17) that the presence of silica during heating enables IpaD to maintain its α -helical structure as shown by the characteristic double minima in its CD spectrum. The IpaD in solution completely denatures during heating, and the IpaD heated on silica has a small decrease in molar ellipticity from that of the native IpaD. This small decrease in molar ellipticity should not reduce IpaD's efficacy in a vaccine. CD spectra for silica sample SA3 can be found in Figure 3.18. Figure 3.19 shows that the addition of LDAO is not responsible for the refolding of the protein, as the CD spectra for denatured IpaD, and denatured IpaD after LDAO addition are both flat lines.

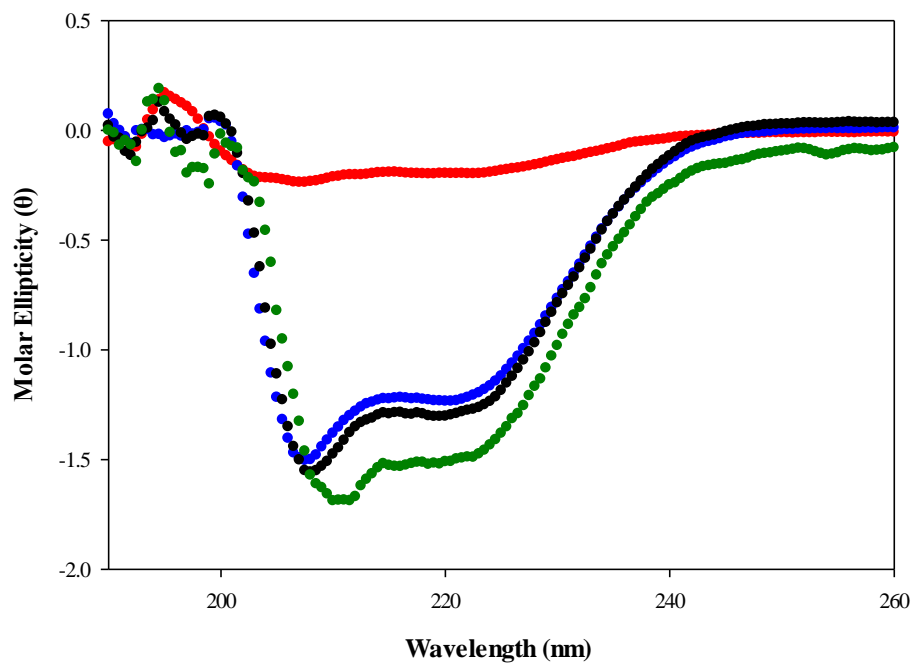


Figure 3.17. CD spectra for native unheated IpaD (green), native heated IpaD (red), IpaD removed from silica sample SA4 unheated (black), and IpaD removed from silica sample SA4 (blue) heated to 95 °C for 2 hours.

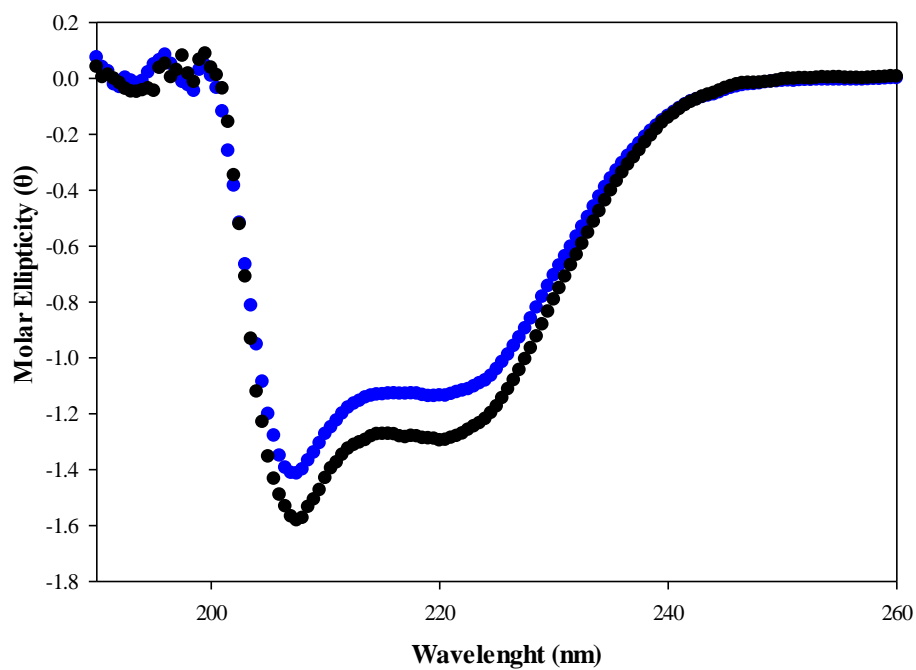


Figure 3.18. CD spectra for heated IpaD on SA3 (blue) and unheated IpaD on SA3 (black)

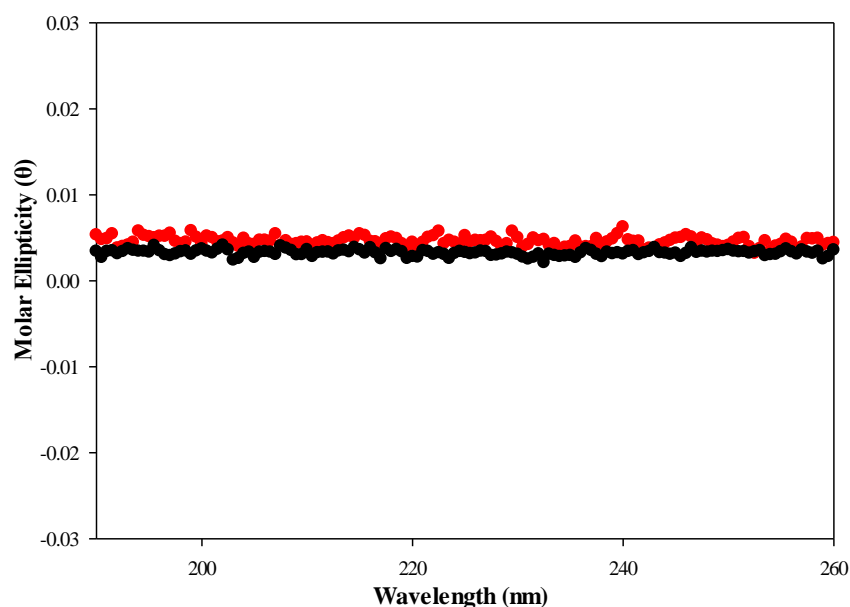


Figure 3.19. CD spectra for denatured IpaD before (black) and after (red) LDAO addition. LDAO addition does not induce protein refolding

The source of the loss in structure for the IpaD heated on silica is not necessarily due to heating. It has been commonly reported that proteins lose some of their conformational structure upon adsorption to a solid surface.^{189,190,191,192} Another possible explanation for this decrease in signal strength is the effects of LDAO on IpaD. This zwitterionic detergent is used at a high concentration to remove IpaD from the silica in these studies. One potential problem is that LDAO increases the high tension (HT) voltage due to the high detergent concentration (10% LDAO). During CD analyses, it was observed that the HT voltage is above the recommended value of 600 V at wavelengths below 200 nm. This indicates that the sample is absorbing too much light, which means it is over concentrated. This effect creates noise in the CD wavelength range of 190-200 nm, which eliminates the expected Cotton effect peak at 195 nm that is seen in the native IpaD sample in 1X PBS (Figure 3.20). Decreasing the LDAO concentration does not necessarily reduce this noise, as IpaD in 3% LDAO exhibited even a greater difference in molar ellipticity to IpaD in PBS than the IpaD in 10% LDAO (Figure 3.21). Furthermore, the drop in molar ellipticity is

potentially due to the buffer concentration interference with the CD signal for the protein. LDAO can also have adverse effects such as forming micelles around IpaD, which can affect the intensity of IpaD's natural CD spectra. While it is difficult to isolate the effect of LDAO on the CD signal from the physical effect of LDAO interactions with IpaD, additional studies have indicated that LDAO is partially denaturing IpaD during the desorption process. IpaD in 1X PBS exhibits a lower molar ellipticity than that of IpaD in 10% LDAO (Figure 3.20), where the characteristic 208 nm minimum peak appears at -2.0 and -1.6, respectively.

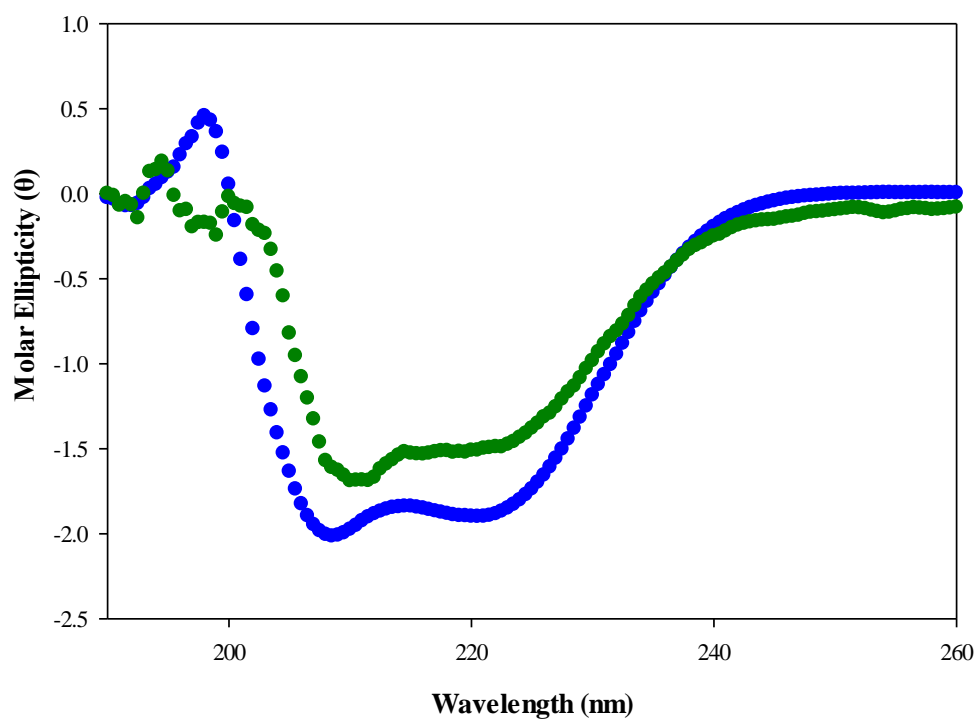


Figure 3.20. Comparison of IpaD structure in PBS (blue) and 10% LDAO (green)

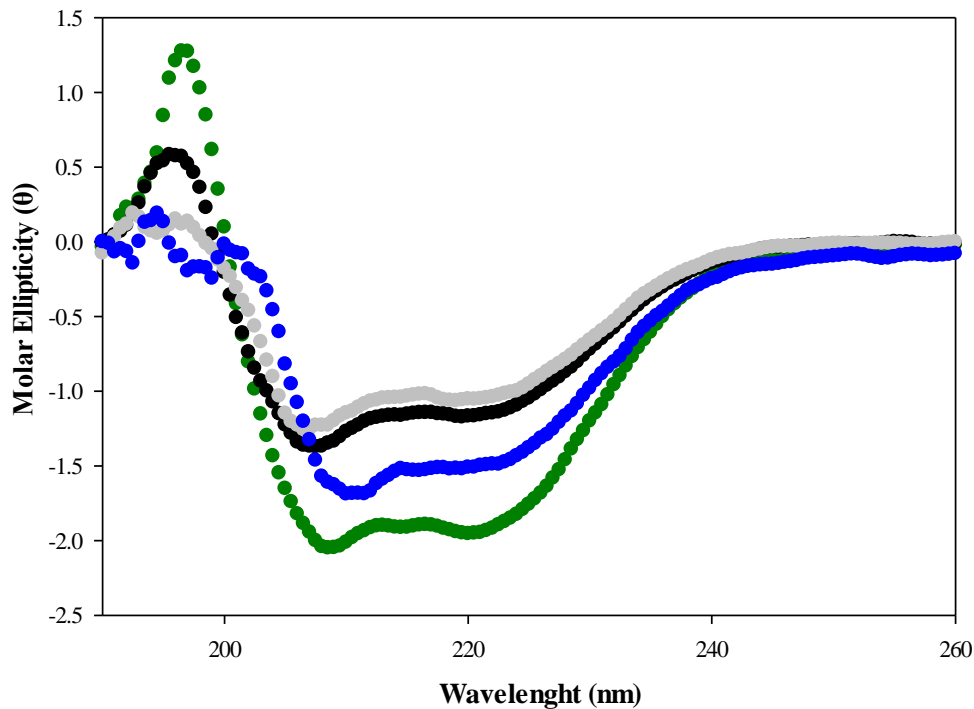


Figure 3.21. CD spectra for native IpaD in PBS (green), 10% LDAO (blue), 0.5% LDAO (black) and 3% LDAO (gray)

The CD samples for the blue and black spectra as shown in Figure 3.17 underwent the entire experimental process of adsorption onto silica sample SA4, washing, and desorption with 10% LDAO. The only difference was the sample shown in blue was heated before desorption and the sample shown in black was not heated. Both IpaD samples were exposed to potential structural changes from adsorption onto a solid surface and the unfavorable effects of LDAO. The significant overlay of the blue and black curve indicates that there was negligible secondary structure change due to heating IpaD on silica, which is evidence that silica sample SA4 successfully thermally stabilized IpaD during heating. The elimination of heating as a structural change while IpaD is attached to silica makes a strong case that adsorbed IpaD will maintain its secondary α -helical structure during vaccine transport under high temperature conditions. CD spectra for IpaD

adsorbed at room temperature for 6 days is provided in Figure 3.22, and it is evident that IpaD secondary structure is maintained even in a longer-term study.

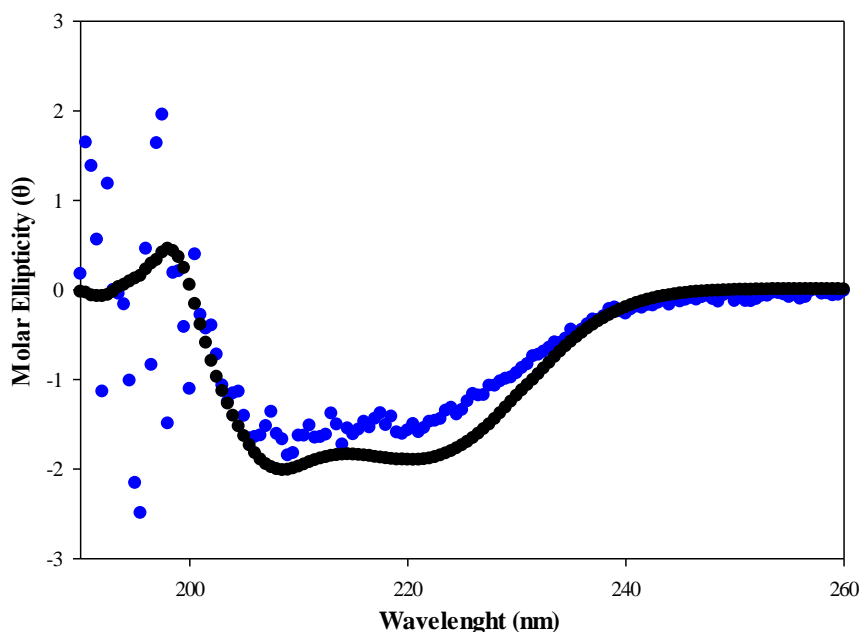


Figure 3.22. CD spectra for native IpaD in LDAO (black) and IpaD adsorbed in silica at room temperature for 6 days (blue)

To determine the effect of pore size on thermal stability, IpaD was adsorbed onto a larger pore sized silica (SA7) and heated as shown in Figure 3.23 . For silica SA7, multilayer adsorption is dominant. It is evident that in this case, the protein does not conserve its secondary structure to the same degree it does when adsorbed to SA4. Therefore, it is possible to conclude that the silica-protein bonds are stronger than protein-protein interactions and monolayer adsorption is preferable to achieve the highest degree of thermal stabilization.

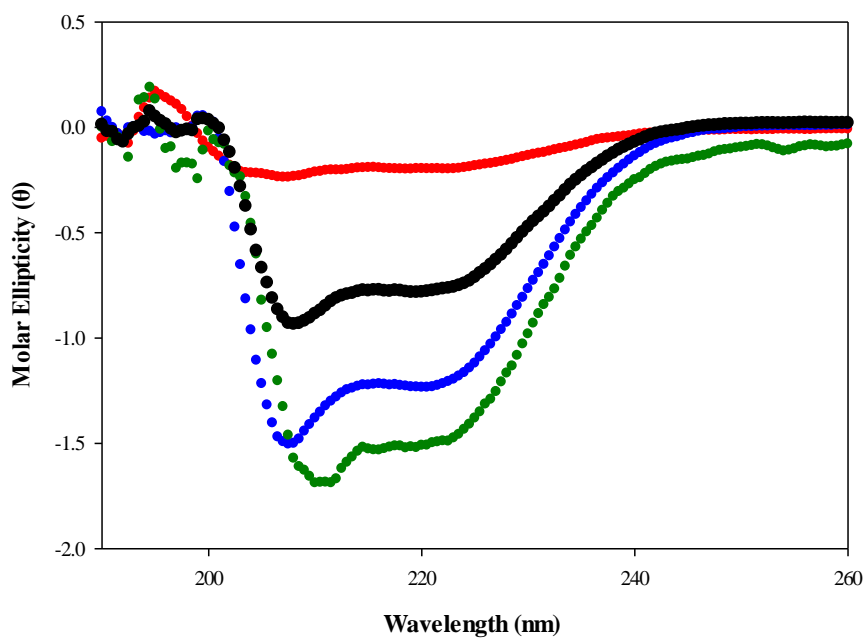


Figure 3.23. CD spectra for native unheated IpaD (green), native heated IpaD (red), IpaD removed from silica sample SA7 heated to 95 °C for 2 hours (black), and IpaD removed from silica sample SA4 (blue) heated to 95 °C for 2 hours

3.10 Effect of Silica Size on Equilibrium Constants

As shown in Table 3.4, pore size has a significant effect on the equilibrium constant values. For silicas between 15 to 25 nm (SA3-SA5) the K value is very large, indicating that the rate constant of adsorption is much greater than the rate constant of desorption. However, as the pore size increases, becoming significantly larger than size of the protein, the equilibrium constant drops. This is indication that adsorption in silicas with larger pores in comparison to the “just right” pore size range. These results are in good agreement with the results in Figure 3.23 whereas the pore size increases, protein thermal stability in adsorbed silica decreases.

Table 3.4. Effect of pore size on protein adsorption equilibrium constant

Silica	Average pore size (nm)	K value
SA3	15.0	18.44
SA4	17.7	30.94
SA5	24.2	33.21
SA6	30.2	2.45
SA7	36.6	3.83

Chapter 4: Case Study 2-Lactoferrin Thermal Stabilization via Adsorption and Desorption using Non-ionic Detergents

4.1 Introduction

Lactoferrin (Lf) is an iron-binding glycoprotein prominent in milk and other external fluids.¹⁹³ In addition to regulating iron adsorption and modulating immune responses, Lf has valuable antioxidant, anti-bacterial, anti-microbial, anti-viral, anti-inflammatory, and anti-cancer properties.¹⁹⁴ One of Lf's most popular applications is as a supplement for infant milk formula because non-iron-saturated Lf can deplete iron from bacteria, which reduces bacteria growth and decreases diarrhea and other intestinal issues in infants.¹⁹⁴

The unique properties of Lf can also be used as an adjuvant therapy for a range of metabolic and viral diseases. There is evidence that Lf plays a role in glucose metabolism and the regulation of intestinal glucose adsorption, so it may be beneficial to restore glucose transport in type 2 diabetes patients.¹⁹⁵ Lactoferrin may be used as an adjuvant therapeutic for gastrointestinal diseases, such as rotavirus, by regulating intestinal flora and decreasing both vomiting and diarrhea in infants and children.¹⁹⁶⁻¹⁹⁸ Lactoferrin can also be used to increase levels of T and B cells in immunocompromised patients.¹⁹⁹ The anti-bacterial and anti-viral activity of Lf has demonstrated positive results when used in combination with anti-bacterial drugs such as zidovudine for HIV,²⁰⁰ ribavirin for hepatitis C,²⁰¹ and cidofovir for cytomegalovirus.²⁰²

Lactoferrin has a molecular weight of 80 kDa and is composed of a single polypeptide chain of 680-700 amino acids folded into two symmetrical lobes.^{193, 203} Each lobe is made up of two α/β domains, consisting of a parallel β -sheet surrounded by α -helices.²⁰³ The two symmetrical lobes are connected by a short α -helical chain as shown in Figure 4.1. Compared with many proteins, Lf has a high thermal stability with a denaturing temperature above 75 °C.

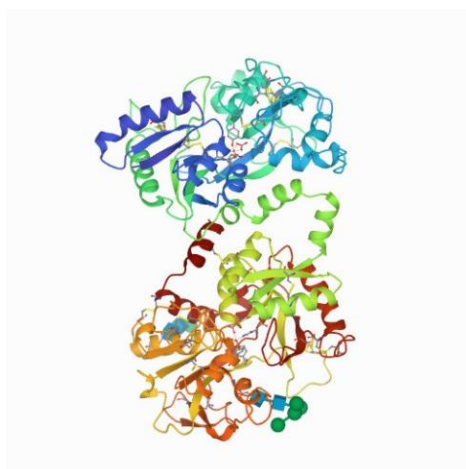


Figure 4.1. Three-dimensional structure of bovine lactoferrin¹⁸⁵

Over 20% of Lf is composed of glutamic acid and aspartic acid amino acids as the most abundant residues.²⁰⁴ These amino acids are able to form a hydrogen bond with its amine group, and two hydrogen bonds with the two carboxylic groups. In addition, 9% of Lf is made up of glutamine and asparagine amino acids and 7% is serine amino acid. Glutamine and asparagine can form two hydrogen bonds with the amide groups and serine can form hydrogen bonds via the hydroxymethyl groups. Since Lf is positively charged and the silica surface is negatively charged, electrostatic interactions will further stabilize the protein within the silica pores. Our working hypothesis is that hydrogen bonding between protein amino acid groups and the silica surface is the primary adsorption mechanism that stabilizes the protein structure and prevents denaturation (Figure 4.2).

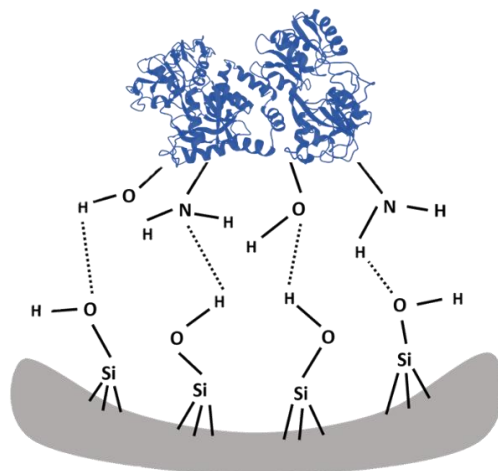


Figure 4.2. Proposed hydrogen bonds between Lf residues and mesoporous silica surface

One of the greatest challenges with protein adsorption onto silica for adaptation to clinical conditions is to desorb, release, and separate the protein from the stabilization support. Protein desorption is challenging, and only a few groups have successfully reported releasing proteins from the stabilization supports without damaging the protein structure.

The first case study demonstrated the proof-of-principle for adsorption onto mesoporous silica with Invasion Plasmid Antigen D (IpaD).⁴⁴ The research confirmed retention of IpaD's secondary structure when subjected to thermal stress. Ten percent *N,N*-dimethyldodecylamine *N*-oxide (LDAO) was used to desorb IpaD from the silica gel. LDAO is a strong surfactant with a dodecyl alkyl head and a zwitterionic tail that can effectively break the hydrogen bonds that attached IpaD to the silica surface. However, LDAO is a strong zwitterionic detergent and when used at high concentrations, it can lead to a loss in protein structure that was observed by Circular Dichroism (CD).⁴⁴ In order to transfer this methodology of biomolecule stabilization for clinical application, it is necessary to discover alternative desorbing agents. In this case study the thermal stability of Lf adsorbed onto silica was evaluated using clinically acceptable desorbing reagents including

polyoxyethylene sorbitol esters (e.g. Tween 20, Tween 40, Tween 80) and a poly(ethylene glycol) derivative (e.g. Triton X-100).

4.2 Adsorption Modeling

Lactoferrin adsorption onto porous silica is strongly influenced by the pore diameter of the silica (Figure 4.3). Lactoferrin's unit cell dimensions are 13.8 nm, 8.7 nm and 7.3 nm.¹⁸⁵ Therefore, there is very little adsorption observed for pore sizes less than 15 nm. Silicas with a pore diameter greater than 15 nm adsorb over 95% Lf.

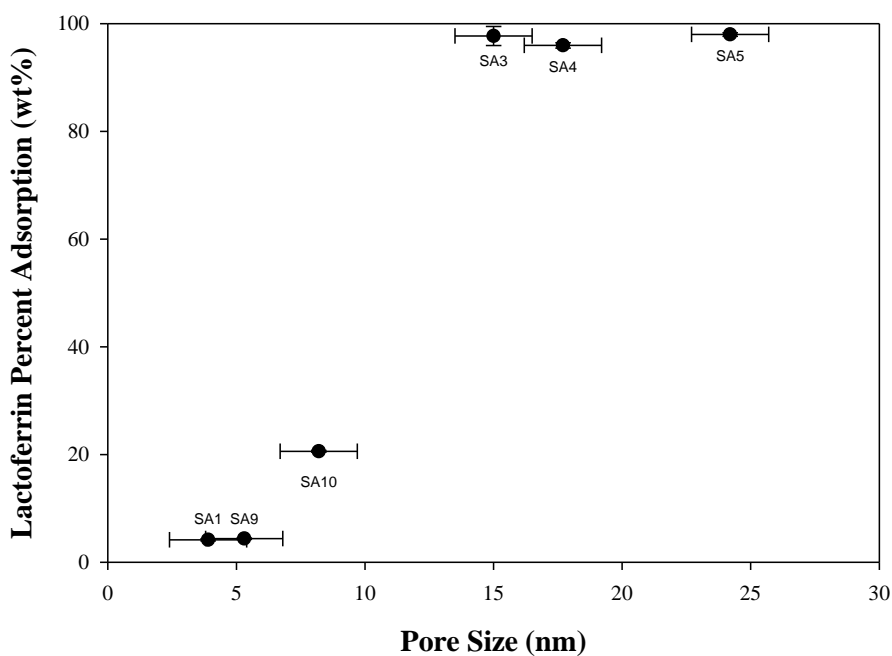


Figure 4.3. Percent of Lf adsorbed to mesoporous silica materials as a function of average pore diameter (nm)

The experimentally determined adsorption capacity for lactoferrin on the mesoporous silica was found using Equation 3.11. The Lf adsorption isotherm (Figure 4.4) was fit using the Langmuir adsorption model (Equation 3.10) in order to determine the maximum Lf adsorption onto the silica.

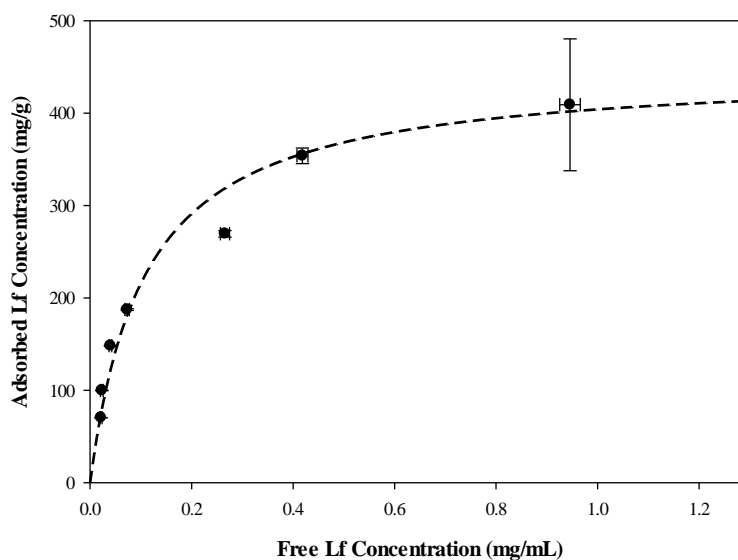


Figure 4.4. Adsorption isotherm of Lf on silica SA5 using the Langmuir model. A decreasing mass of the silica sample results in larger error bars at the highest Lf concentration.

Using the linearized form of the Langmuir model plot (Equation 3.12), the maximum monolayer coverage and equilibrium rate constant were determined to be 447 mg Lf/g silica and 9.3 mL/mg, respectively, as shown in Figure 4.5. In comparison to IpaD, the equilibrium rate constant for Lf on SA5 is significantly smaller than that of IpaD (9.3 mL/mg vs 33.21 mL/mg). This may be indication that protein size has an important effect on the strength of adsorption.

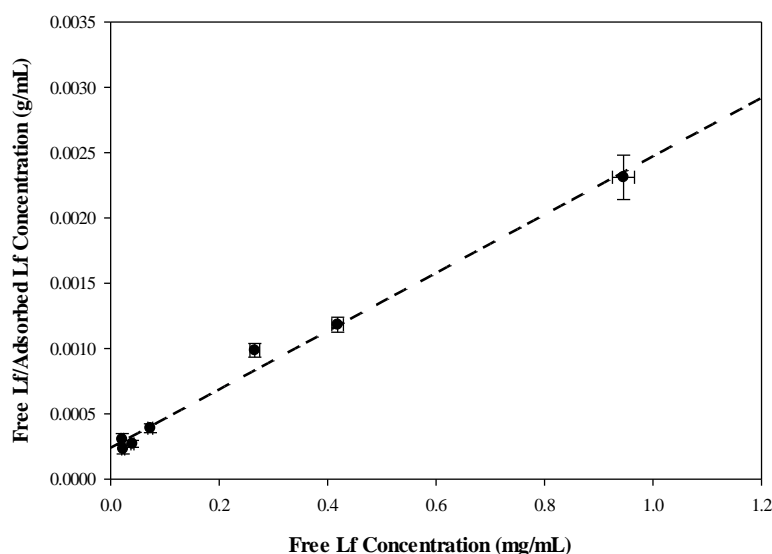


Figure 4.5. Linearized adsorption isotherm for Lf on silica SA5 using the Langmuir model ($R^2=0.99$)

The close fit ($R^2 = 0.99$) of the experimental adsorption data for Lf on the mesoporous silica (Figure 4.4 and Figure 4.5) using the Langmuir model suggests a monolayer adsorption mechanism. The maximum monolayer coverage (mg Lf/g silica) was converted to surface area (m^2 Lf/g silica) using a surface area for Lf of $120.06 \text{ nm}^2/\text{Lf molecule}$ (based on the two largest unit cell parameters of 8.7 and 13.8 nm) and a molecular weight of 80 kDa.

$$\frac{447 \text{ mg Lf}}{\text{g silica}} \times \frac{\text{mol Lf}}{8.0 \times 10^7 \text{ mg}} \times \frac{6.02 \times 10^{23} \text{ proteins}}{1 \text{ mol}} \times \frac{120 \text{ nm}^2}{\text{proteins}} \times \frac{(1 \text{ m})^2}{(1 \times 10^9 \text{ nm})^2} = \frac{404 \text{ m}^2 \text{ Lf}}{\text{g silica}} \quad (4.1)$$

The maximum monolayer coverage ($404 \pm 33.9 \text{ m}^2/\text{g}$) calculated using the Langmuir model is in good agreement with the accessible surface area ($\text{SA} = 370.7 \pm 3.3 \text{ m}^2/\text{g}$) measured using the nitrogen BJH method.⁴⁴

For a silica such as SA7, with a larger pore diameter ($\text{PD} = 36.3 \pm 1.5 \text{ nm}$), the maximum monolayer coverage calculated using the Langmuir model is significantly different than the BJH accessible surface area (Table 2). However, if the Lf unit cell volume is used instead of the Lf unit

cell surface area in Equation 4.1, it is possible to calculate the maximum coverage in terms of volume.

$$\frac{442 \text{ mg LpaD}}{\text{g silica}} \times \frac{\text{mol LpaD}}{8.0 \times 10^7 \text{ mg}} \times \frac{6.02 \times 10^{23} \text{ proteins}}{1 \text{ mol}} \times \frac{876.4 \text{ nm}^3}{\text{proteins}} \times \frac{(1 \text{ cm})^3}{(1 \times 10^7 \text{ nm})^3} = \frac{2.91 \text{ cm}^3 \text{ LpaD}}{\text{g silica}} \quad (4.2)$$

Since Lf and nitrogen BJH volume measurements are in good agreement, the adsorption is likely multilayer (i.e. bilayer) instead of monolayer in silicas with larger pore sizes.

Table 4.1. Nitrogen BJH surface area (N₂-SA) and pore volume (N₂-PV) compared with Lf surface area (Lf-SA) and pore volume (Lf-PV) calculated using the Langmuir model for silica sample SA7. Langmuir plots for SA6 are provided in Appendix E.

Silica Sample	N ₂ -SA(m ² /g)	Lf-SA (m ² /g)	N ₂ -PV (cm ³ /g)	Lf-PV (cm ³ /g)
SA7	286.1 ± 3.3	211.3 ± 46.8	2.87 ± 0.01	2.92 ± 0.18

The Langmuir isotherm of silica sample SA5 (PD = 24.2 ± 1.5 nm) was compared to the corresponding isotherm for silica sample SA1 (PD = 3.9 ± 1.5 nm). The adsorbed Lf concentration in SA1 is negligible in comparison to the adsorbed Lf concentration in SA5 (Figure 4.6). These results are expected, since the pore diameter of SA1 is smaller than Lf's external dimensions (largest two-unit cell parameters of 8.7 and 14.8 nm), preventing adsorption of Lf in SA1. It is important to note that if Lf was adhering to the surface of SA1, the adsorbed amount of Lf would be significantly higher. This is confirmation that Lf is primarily adsorbed (99+%) in the silica pores and not on the silica surface.

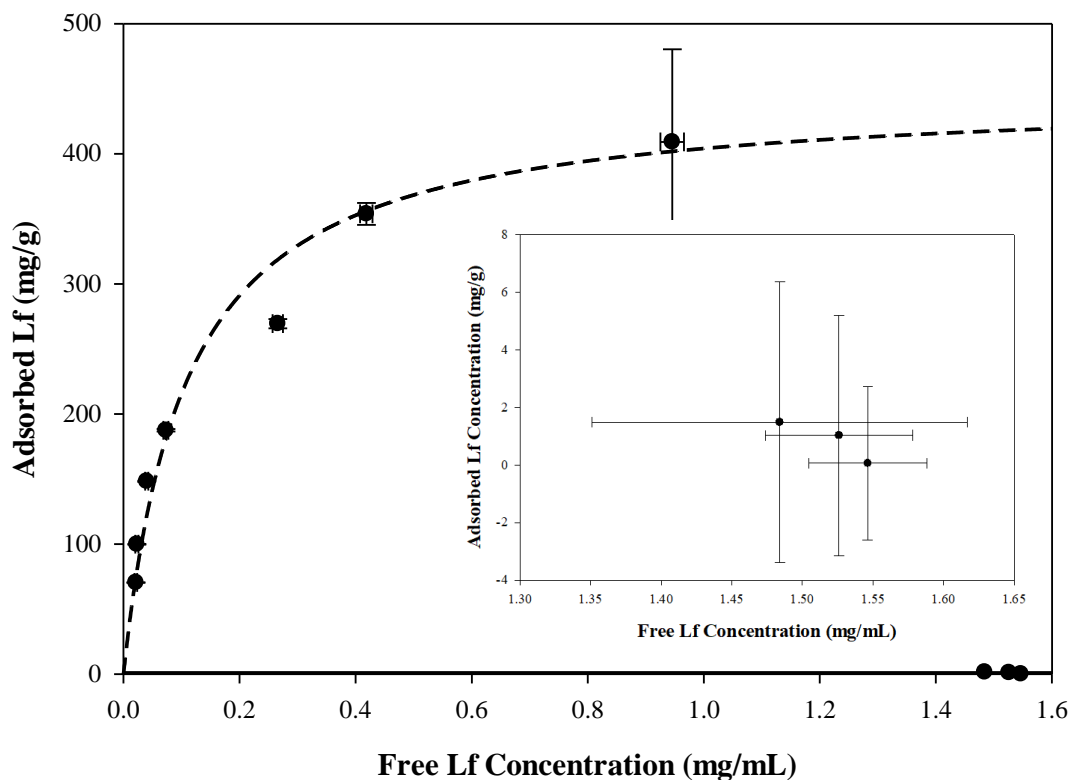


Figure 4.6. Adsorption isotherm for Lf on silica sample SA5 using Langmuir model. Inset is expanded view of silica sample SA1 for comparison.

Overall, the size of the silica pore relative to the size of the protein determines the kind of protein adsorption. For pore sizes smaller than the Lf's external dimensions (SA1), the protein cannot physically fit inside the silica pore, resulting in negligible adsorption. When the pore size is just right (i.e., Goldilocks Effect), monolayer protein coverage is achieved (SA5). Finally, for pore sizes significantly larger than Lf's dimensions, multilayer adsorption occurs. Figure 4.7 provides a schematic of the three types of protein-pore interactions.

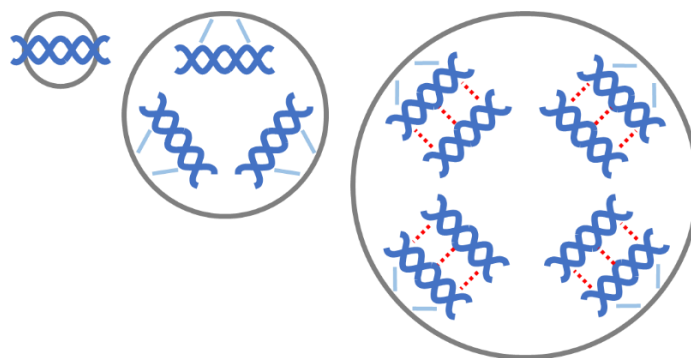


Figure 4.7. Comparison of the three types of pore interactions with Lf, (A) pore size is too small and Lf does not fit into the pore, (B) pore size is just right “Goldilocks Effect”, monolayer coverage, hydrogen bonds depicted by solid lines, (C) pore size is too large, multilayer coverage, van der Waals forces depicted by dotted lines.

The adsorption data (free protein concentration vs adsorbed protein concentration) was also fit to both the Freundlich and Temkin models. Comparing the Langmuir, Freundlich, and Temkin models (Figure 4.5, Figure 4.6, Figure 4.8 and Figure 4.9), it is evident that the Langmuir model is the best fit of the experimental data. The R^2 value for the Langmuir model is almost a perfect fit at $R^2 = 0.99$ compared with the Freundlich model ($R^2 = 0.93$). In the case of the Temkin model with a $R^2 = 0.98$ it is difficult to determine if adsorption is monolayer or multilayer; however, considering the good agreement in the calculated surface area using the linearized Langmuir model with the nitrogen BJH accessible surface area leads to the conclusion that the adsorption is monolayer.

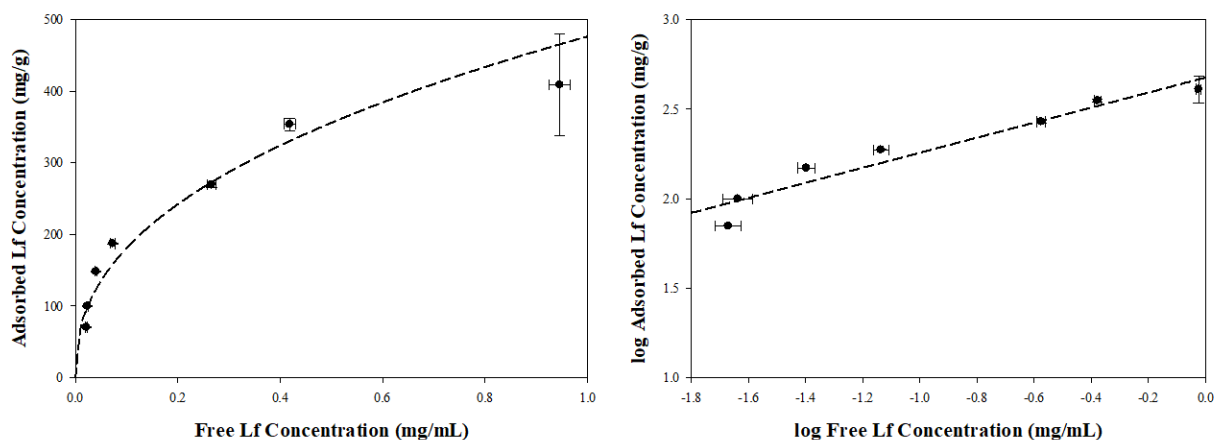


Figure 4.8. Freundlich adsorption isotherm (left); linearized isotherm for silica sample SA5 using the Freundlich Model ($R^2=0.93$) (right)

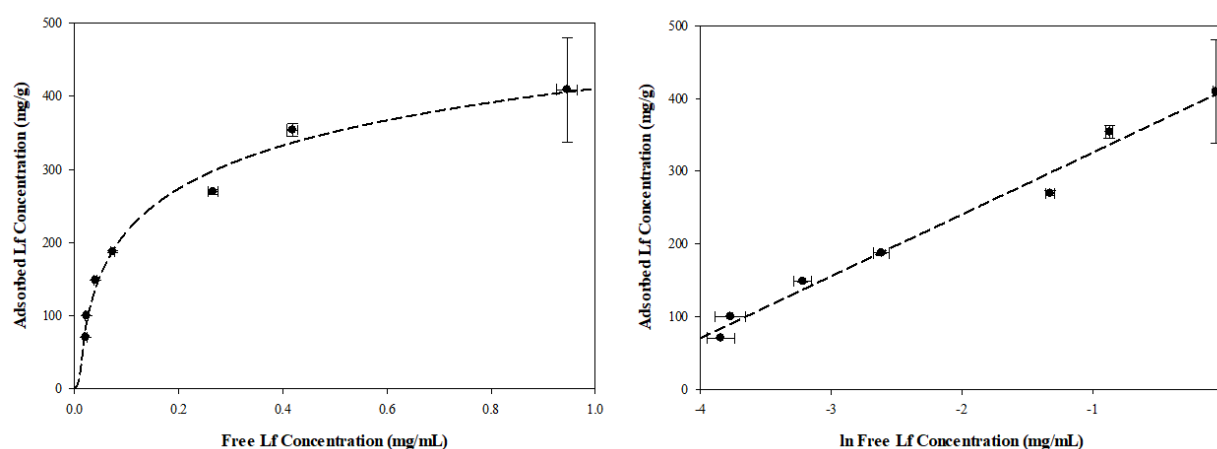


Figure 4.9 Temkin adsorption isotherm (left); linearized isotherm for silica SA5 using the Temkin Model ($R^2=0.98$) (right).

4.3 Lactoferrin Thermal Stability

To evaluate if adsorption onto mesoporous silica will protect the Lf protein from denaturing, samples were heated to 90 °C for 90 minutes and the protein desorbed from the silica using 3 vol% Tween 20. The Lf protein's secondary structure was analyzed using CD. A native, non-adsorbed Lf sample was used as a control. The CD results demonstrate that the secondary structure of the Lf adsorbed to the mesoporous silica was protected against heating and exhibits the same double

minima at 208 and 218 nm relative to the native, unheated Lf. This double minima with a “W” like shape indicates protein samples contain a substantial amount of α -helical chains.

Heated Lf adsorbed onto silica is able to retain its secondary α -helical structure while native Lf that was not adsorbed to silica denatured after heating and completely lost its secondary structure (Figure 4.10). The adsorption of the Lf onto mesoporous silica protected the protein from denaturing at elevated temperatures compared with the control. In addition, the Tween-20 was effective at desorbing the Lf protein, and the slight difference in molar ellipticity compared with the native Lf may be a result of adding the detergent resulting in a small concentration difference.

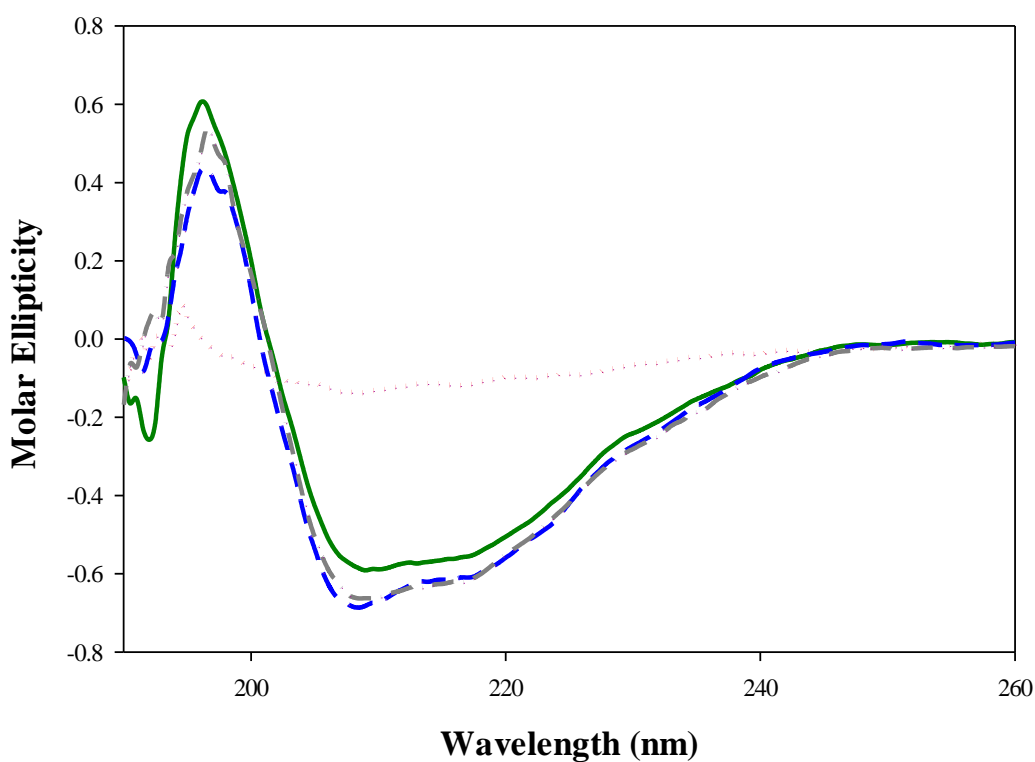


Figure 4.10. CD spectra for native unheated Lf (solid), native heated Lf (dotted), unheated Lf desorbed from silica SA5 (dashed-dotted), and heated Lf desorbed from silica SA5 (dashed). Heat treatment was at 90 °C for 90 min.

The small decrease in molar ellipticity at a wavelength of 195 nm in the Lf heated on silica versus the native Lf samples is most likely due to protein conformational changes during the adsorption

process rather than protein denaturing due to heating. The same trend was found for the Lf desorbed from silica without heating. It is well known that proteins may lose some of their secondary structure when adsorbed to a solid surface.^{189,190,191,192} The CD results for unheated Lf desorbed from silica (Figure 4.10, dashed-dotted line) and heated Lf desorbed from silica (Figure 4.10, dashed line) confirm that heating is not responsible for a significant loss of structure. The spectra for both these samples are nearly identical, demonstrating that the mesoporous silica can thermally stabilize Lf. In addition, the heat exposure is not responsible for the very small decrease in molar ellipticity and is likely a result of the adsorption and desorption process.

4.4 Desorption Detergents

A goal when selecting a detergent for protein desorption was to find candidates that were clinically viable and did not affect the protein structure. For this purpose, nonionic detergents were selected since the head groups are uncharged making them less harsh than ionic and zwitterionic detergents. Polyoxyethylene sorbitol esters (e.g. Tween 20, Tween 40, Tween 80) and a poly(ethylene glycol) derivative (e.g. Triton X-100) were evaluated as Lf desorption agents. A concentration of 3 vol% Tween 20 had the lowest Lf recovery (e.g. 66 wt%) and Tween 80 had the highest Lf recovery (e.g. 87 wt%) as shown in Figure 4.11. Triton X-100 can also be used at lower concentrations in clinical applications, and even at a concentration of 2 vol% it had the highest Lf recovery (e.g. 94 wt%) of all the desorbing agents studied. In addition, at lower concentrations such as at 1 vol% Tween 80 was consistently the best performing detergent. This is important to note in case a specific clinical application requires the choice of different detergents with lower concentrations to meet safety protocols.

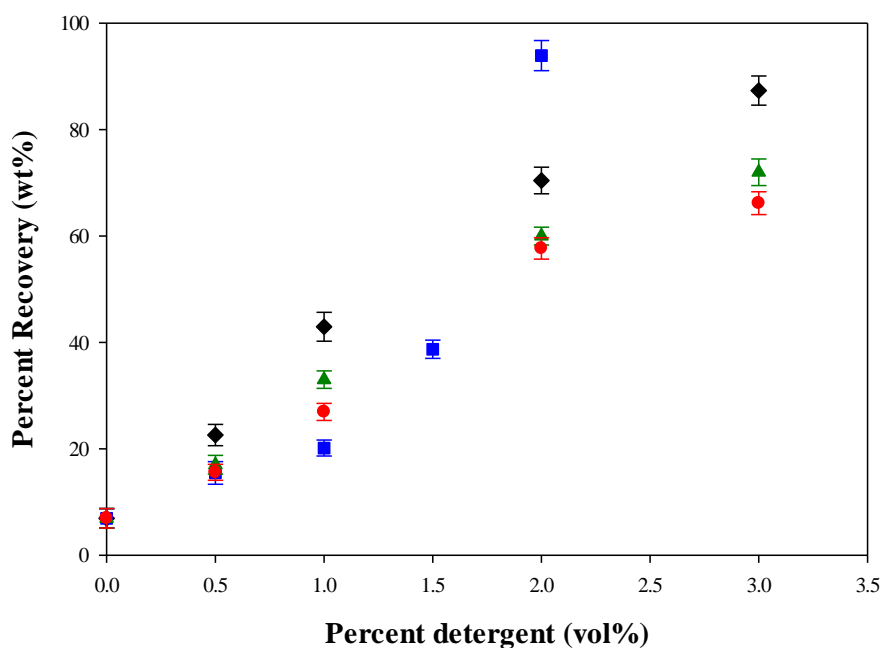


Figure 4.11. Recovery (wt%) of Lf from SA5 at various concentrations (0 to 3 vol%) for Tween 20 (circles), Tween 40 (triangles), Tween 80 (diamonds) and Triton X-100 (squares).

A trend for Lf desorption from mesoporous silica is the detergent with the highest hydrophobicity has the highest Lf recovery. The hydrophile-lipophile balance (HLB) is a measure of the hydrophobicity of a detergent. As the HLB decreases, the detergent's hydrophobicity increases. Triton X-100 is the most hydrophobic of the detergents (lowest HLB), while Tween 20 is the least hydrophobic of the detergents (highest HLB), Tween 80 is also more hydrophobic than Tween 40 which is more hydrophobic than Tween 20 as shown in Table 4.2. During desorption, the detergent monomers likely bind to the hydrophobic part of the protein, forming hydrophobic detergent-protein interactions; therefore, if the detergent is more hydrophobic, the hydrophobic interactions with the protein are stronger and desorption is more effective. This trend is consistent with the Tween detergent results shown in Figure 4.11 and for Triton X-100 concentrations at 2 vol%.

Table 4.2. Detergent hydrophile-lipophile balance values^{205, 206}

Detergent	HLB
Tween 20	16.7
Tween 40	15.7
Tween 80	15
Triton X-100	13.5

4.5 Lactoferrin Stability in Detergent Solutions

In order to select the optimal detergent for Lf desorption, it is necessary to ensure that the protein retains its secondary structure in the detergent solution. Lactoferrin was tested in 3 vol% Tween 20 and 3 vol% Tween 80 and maintains the same characteristic double minima as native Lf at 208 and 218 nm as shown in Figure 4.12. This indicates that Lf does not lose its conformational structure in 3 vol% Tween 20 and Tween 80. However, the double minima spectrum for Lf in 1 vol% Triton X-100 was not found as shown in Figure 4.12.

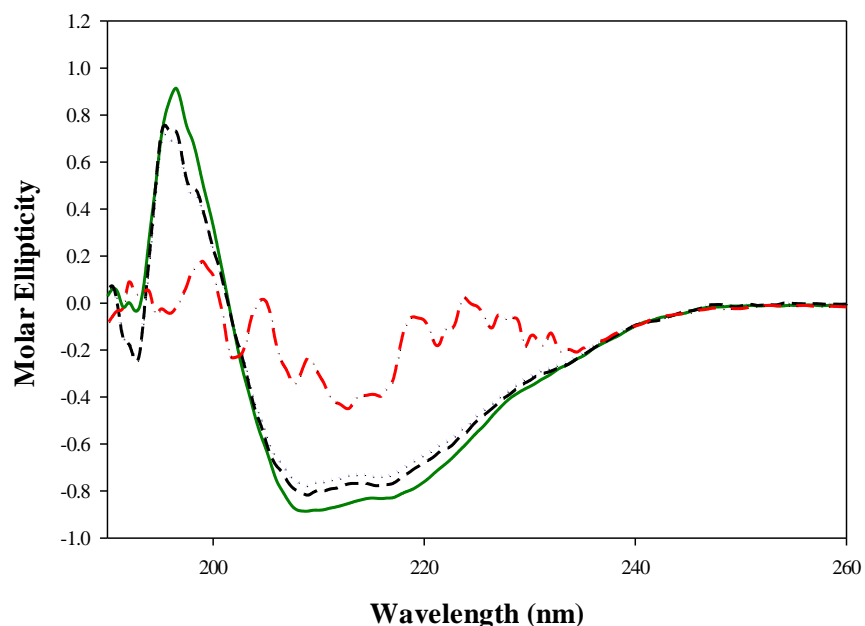


Figure 4.12. CD Spectra for native Lf in 1XPBS (solid), Lf in 3% Tween 80 (dashed), Lf in 3% Tween 20 (dotted), and Lf in 1% Triton X-100 (dashed-dotted).

It is unlikely that the Lf is unfolding in 1 vol% Triton X-100, and this result is likely due to issues in the CD spectrum that arise from strong UV absorbance of the detergent at the same wavelength range where Lf's UV absorbance is observed (Figure 4.13). Even though Triton X-100 yields an excellent protein recovery (94 wt%), interference in measuring the absorbance with Lf and the lack of another analytical technique to accurately measure Lf secondary structure in the presence of Triton X-100 led to the choice of Tween 80 as the optimal detergent. Tween 80 has almost as high of a protein recovery (87 wt% at 3 vol%) as Triton X-100 (94 wt% at 2 vol%), but it does not exhibit strong UV absorbance in the same range as Lf (Figure 4.13).

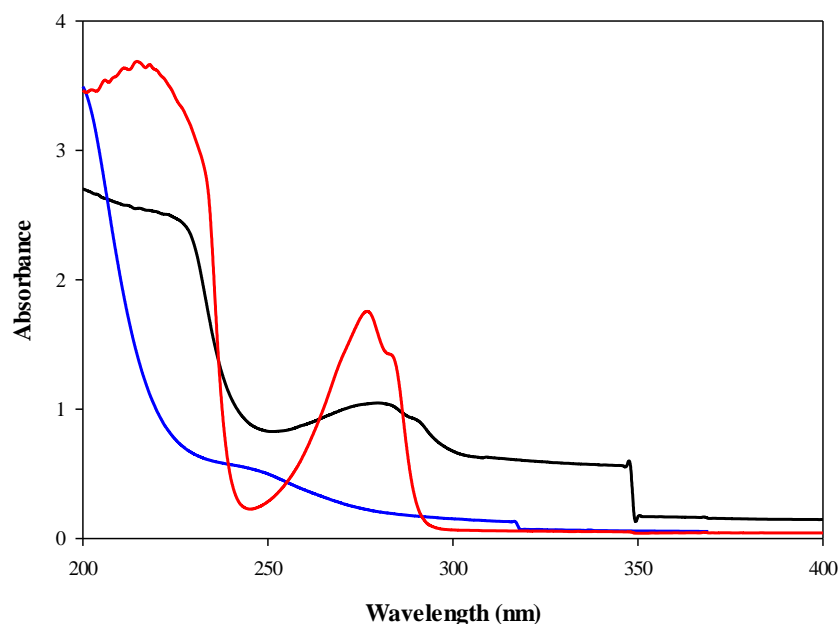


Figure 4.13. UV-Vis spectra for lactoferrin (black), Triton X-100 (red) and Tween 80 (blue)

4.6 Silica and Detergent Interactions

To develop an understanding of the desorption mechanism, it is necessary to study the silica-detergent interactions that play a role in the Lf protein removal from silica. The strong UV spectra for Triton X-100 made it a good choice for measuring its adsorption on silica samples of different pore sizes (i.e., no protein, just detergent adsorption). A concentration of 1 vol% Triton X-100 was chosen, since it is higher than the critical micelle concentration (0.22 mM^{207} or 0.005 vol%). As expected, as the pore size increased the adsorption increased as shown in Figure 4.14. At concentrations above the critical micelle concentration, detergent monomers and micelles are in equilibrium and adsorption in silica pores is limited by the size of the micelle (e.g. Triton X-100 micelle is approximately 10.5 nm at $20 \text{ }^\circ\text{C}$).²⁰⁸

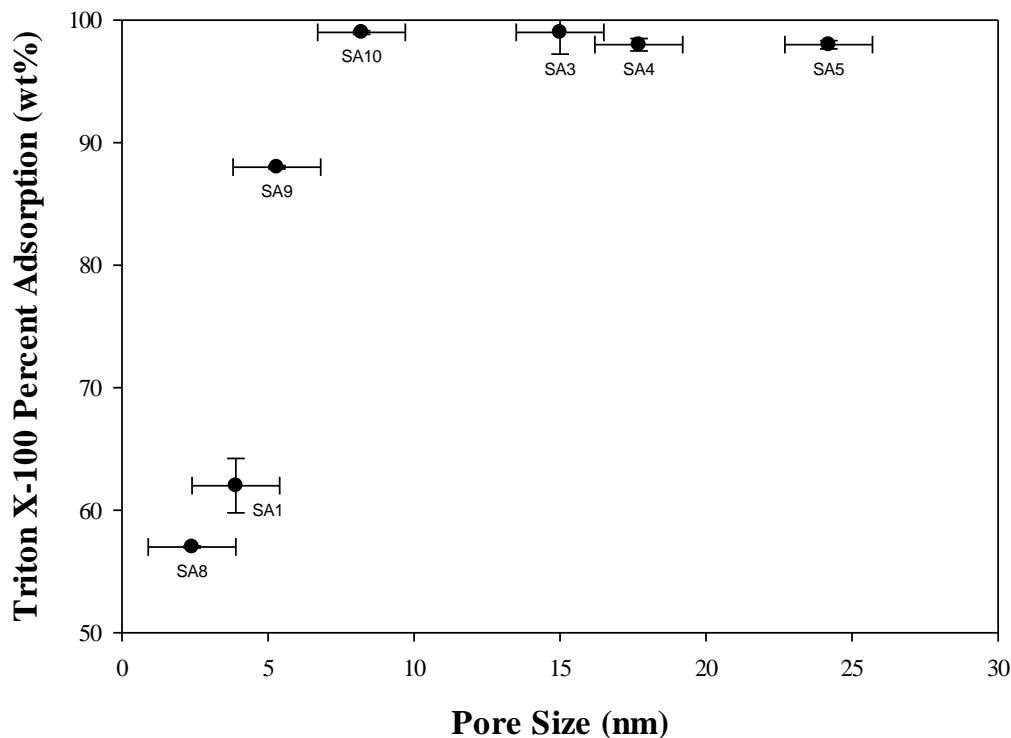


Figure 4.14. Triton X-100 (1.0 vol%) adsorption (wt%) on silicas SA1, SA3-SA5, SA8-10

Silicas with an average pore size/diameter smaller than 5 nm (SA1 and SA8) had an adsorption below 65 wt%. The adsorption is believed to be the result of detergent monomer, which is on the scale of a few nanometers, that can still fit into the silica pores as well as micelles that adhere to the surface. Silicas with a pore size between 5 and 10 nm (SA9 and SA10) show a higher degree of Triton X-100 adsorption, even though the pores are smaller than the size of the micelle. However, the pore size shown in Figure 4.14 is the average pore size and each silica sample has a pore size distribution. Silica samples SA9 and SA10 have an average pore size less than the micelle size, but they do have some pores that are large enough for micelle adsorption, which can account for the higher adsorption in these samples. The samples with pore sizes larger than 10 nm (SA3-SA5) achieve 98-100 wt% adsorption with pores large enough to adsorb the Triton X-100 micelles.

Hydrogen bonds are formed between the Triton X-100 and the silica surface due to the hydrophilic detergent heads of the monomers and exterior of the micelles. The strength of these bonds is likely greater than those of the Lf protein-silica hydrogen bonds that leads to the desorption of the protein. Similar to the hydrophilic interactions of the detergent with the silica, the monomer hydrophobic tails can also interact with the hydrophobic protein amino acids resulting in the release of the Lf from the silica.

To compare the strength of detergent-silica bonds with protein-silica bonds, a silica sample was pre-treated with 3% Tween 80 (for 24h) before adsorbing Lf. In this case, only 48% of Lf was adsorbed onto the SA5 in comparison to 96% adsorption when the silica is not pre-treated with detergent. This is further evidence that the detergent-silica bonds compete with the protein-silica bonds during the desorption process.

Chapter 5: Conclusions and Recommendations

5.1 Case Study 1 – IpaD sorption and thermal stabilization on mesoporous silica

In this case study, silicas have been found to thermally stabilize the IpaD protein. A strong correlation between the physiochemical properties (i.e. pore diameter, accessible surface area and pore volume) for seven silica samples with the adsorption uptake of IpaD has been shown. Silica samples with pore diameters greater than 5 nm were effective at adsorbing IpaD. The excellent fit of the Langmuir model to the experimental adsorption isotherm for silica samples SA3, SA4, and SA5 compared to the Freundlich and Temkin models indicates that IpaD adsorption is likely a monolayer adsorption mechanism. The surface areas of silica samples SA3, SA4, and SA5 were calculated from the maximum monolayer coverage from Langmuir isotherm modeling. The nitrogen surface areas calculated using BJH accessible surface area were 333.2 ± 3.3 , 319.3 ± 3.3 , and 370.7 ± 3.3 m²/g. The surface areas based on IpaD coverage were found to be 316.3 ± 8.9 , 316.6 ± 11.4 , and 371.9 ± 20.2 m²/g for SA3, SA4, SA5, respectively. The nitrogen accessible surface area and surface area calculated from the IpaD isotherm are significantly close for silica sample SA3, and identical for silica samples SA4 and SA5 within error. This provides further evidence of monolayer coverage of IpaD on these silicas. The adsorption modeling of larger pore sized silicas, SA6 and SA7, indicates multilayer adsorption. Furthermore, silica sample SA1 has an average pore diameter of 3.9 nm which is smaller than the external dimensions of IpaD, and SA1 exhibited low adsorption capacity compared to silica samples with a diameter larger than the dimensions of IpaD. From this observation, it is hypothesized that the interaction of IpaD with the silica is mostly inside the pores with minimal external surface interaction. The TEM characterization with gold nanoparticles demonstrated a nearly 1:1 expected ratio between sulfur in the cysteine amino acid of IpaD and AuNP. An EDX spectral scan for sulfur shows IpaD is

evenly distributed over the surface and pores of the silica. IpaD can be easily removed via washing from silicas with pores larger than 25 nm due to a weaker hydrogen bond network. CD spectroscopy results showed that IpaD adsorbed into mesoporous silica sample SA4 with a pore diameter of about 18 nm had remarkably high thermal stability, which was not the case for IpaD in the absence of silica. Therefore, silicas with the proper pore size have the capacity to protect an α -helical protein such as IpaD from thermal denaturation and could be used for replacing a cold-chain vaccine storage method.

5.2 Case Study 2 - Lf sorption and thermal stabilization on mesoporous silica

Mesoporous silicas have successfully been demonstrated to thermally stabilize lactoferrin and nonionic detergents have been found to effectively desorb the protein from the silica surface. An excellent correlation between the experimental adsorption isotherm and the Langmuir model for a mesoporous silica sample with pore size (24.2 ± 1.5 nm) suggests monolayer adsorption of Lf with unit cell dimensions of 8.7 x 14.8 nm. The surface area of the mesoporous silica calculated from the maximum monolayer coverage using the Langmuir modeling was 404 ± 33.9 m²/g and in good agreement with nitrogen BET surface area measurements of 370.7 ± 3.3 m²/g. This supports the claim of monolayer coverage for Lf on mesoporous silica with the proper pore size. The adsorption isotherms for mesoporous silica with pore size larger than 25 nm using the Freundlich and Temkin models suggests multilayer adsorption is occurring. In addition, for silica with a pore size smaller than 15 nm, significantly lower adsorption was observed in comparison to mesoporous silicas with a diameter larger than the dimensions of Lf. This suggests that Lf is adsorbed in the silica pores with minimal surface interaction. CD spectroscopy indicates that Lf adsorbed into mesoporous silica with just the right pore size (24.2 ± 1.5 nm) to achieve monolayer coverage had remarkably high thermal stability, which was not the case for native Lf in the absence of silica or larger pores

with multilayer coverage. In other words, mesoporous silica with just the right pore size, not too small and not too large (i.e., “Goldilocks Effect”), can protect the α -helices and β -sheets that make up Lf’s secondary structure from thermal denaturation. Lf desorption from mesoporous silica using different non-ionic detergents found that the higher the hydrophobicity the more effective the removal of Lf from the silica surface. Tween 80 and Triton X-100 were found to be good non-ionic detergents for recovering Lf at low concentrations. Tween 80 had no effect on the Lf secondary or tertiary structure, but Triton X-100 was inconclusive due to strong absorbance in the same UV range as Lf. The desorption mechanism is believed to be a result of disruption of hydrogen bonds between the Lf protein and silica pore wall.

5.3 Recommendations

It is recommended that additional protein characterization techniques be employed to better understand the effects of heating on the molecular interactions. Fluorescence studies can provide information on changes in tryptophan environment, nuclear magnetic resonance (NMR) can measure chemical shifts to provide useful information for protein structure and solid-state NMR can be exceptionally useful since it may be used when protein is still attached to silica (no need to desorb). Dynamic light scattering can be used to determine the protein hydrodynamic radius, which can be a useful parameter for correlating percent adsorption. Furthermore, it would be very valuable to quantify the CD data and obtain numerical values for the alpha-helical and beta-sheet content in each protein sample. It would also be recommended to perform adsorption isotherms for lactoferrin on all silicas and calculate equilibrium constants similar to Table 3.4.

Future studies should aim to also measure protein activity (i.e. iron binding activity for lactoferrin) before and after heating treatments in conjunction to secondary structure measurements. Finally,

the next step in this research would be to adsorb a vaccine (Flublok® Quadrivalent Vaccine) onto silica to improve its thermal stability.

The final goal in this research project is to design a syringe-like device where the silica-stabilized vaccine and desorbing agent can be transported safely in the same container. This device will use membranes to separate the different components and will be designed so that a doctor or nurse can administer the vaccines without any complicated training (Figure 5.1).

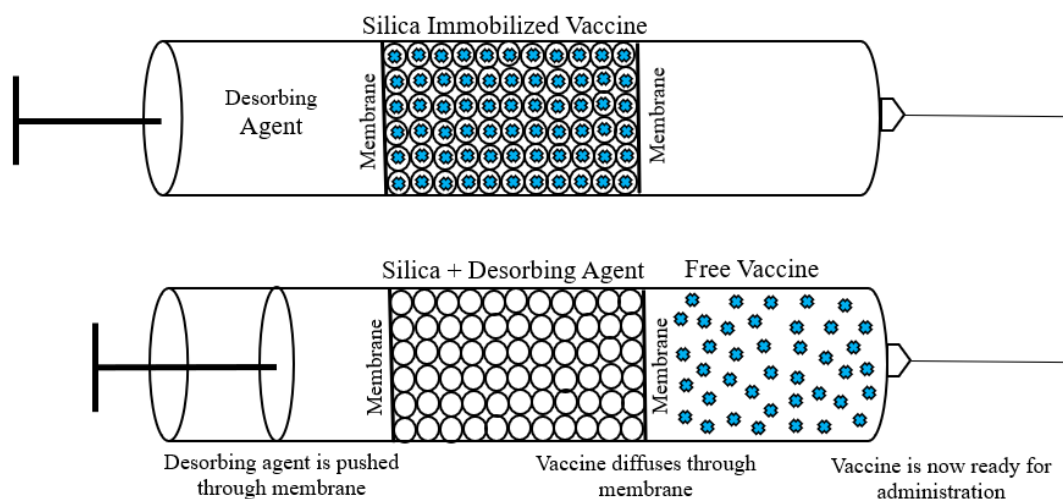


Figure 5.1. Proposed final product concept

References

1. Sumant, O. S. S. Protein Therapeutics Market by Product-Global Opportunity Analysis and Industry Forecast, 2017-2023. <https://www.alliedmarketresearch.com/protein-therapeutics-market> (accessed July 19).
2. Manjrekar, S. W., Trupti; Sumant, Onkar Enzymes Market Type, Source, Reaction Type and Application-Global Opportunity Analysis and Industry Forecast, 2020-2027. <https://www.alliedmarketresearch.com/enzymes-market> (accessed July 19).
3. Insights, F. B. Vaccines Market Size, Share & COVID-19 Impact Analysis Forecast, 2020-2027. (accessed July 19).
4. Report, M. S. Global Covid-19 vaccine market size to be worth USD 25 billion by 2024. (accessed July 19).
5. Ashok, A.; Brison, M.; Letaltec, Y., Improving cold chain systems: Challenges and solutions. *Vaccine* **2017**, *35* (17), 2217-2223.
6. WHO EPI Logistics. https://www.who.int/countries/eth/areas/immunization/epi_logistics/en/index1.html (accessed 6 July).
7. WHO/UNICEF Achieving immunization targets with the comprehensive effective vaccine management (EVM) framework. <https://apps.who.int/iris/bitstream/handle/10665/254717/WHO-IVB-16.09-eng.pdf;jsessionid=01B2497AA0D9C8C610F9F68A27BA4BD0?sequence=1> (accessed 6 July).
8. Brooks, A.; Habimana, D.; Huckerby, G., Making the leap into the next generation: A commentary on how Gavi, the Vaccine Alliance is supporting countries' supply chain transformations in 2016–2020. *Vaccine* **2017**, *35* (17), 2110-2114.
9. Karp, C. L.; Lans, D.; Esparza, J.; Edson, E. B.; Owen, K. E.; Wilson, C. B.; Heaton, P. M.; Levine, O. S.; Rao, R., Evaluating the value proposition for improving vaccine thermostability to increase vaccine impact in low and middle-income countries. *Vaccine* **2015**, *33* (30), 3471-3479.
10. Johannes, T. W.; Zhao, H., Directed evolution of enzymes and biosynthetic pathways. *Current opinion in microbiology* **2006**, *9* (3), 261-267.
11. Sanchez, S.; Demain, A. L., Enzymes and Bioconversions of Industrial, Pharmaceutical, and Biotechnological Significance. *Organic process research & development* **2011**, *15* (1), 224-230.
12. Lencki, R. W.; Arul, J.; Neufeld, R. J., Effect of subunit dissociation, denaturation, aggregation, coagulation, and decomposition on enzyme inactivation kinetics: II. Biphasic and grace period behavior. *Biotechnology and bioengineering* **1992**, *40* (11), 1427-1434.
13. Manning, M.; Chou, D.; Murphy, B.; Payne, R.; Katayama, D., Stability of Protein Pharmaceuticals: An Update. *An Official Journal of the American Association of Pharmaceutical Scientists* **2010**, *27* (4), 544-575.
14. Wang, W., Lyophilization and development of solid protein pharmaceuticals. *International journal of pharmaceutics* **2000**, *203*, 1-60.

15. Juan-Giner, A.; Alsalhani, A.; Panunzi, I.; Lambert, V.; Van Herp, M.; Gairola, S., Evaluation of the stability of measles vaccine out of the cold chain under extended controlled temperature conditions. *Vaccine* **2020**, *38* (11), 2473-2477.
16. Narayan, R.; Nayak, U. Y.; Raichur, A. M.; Garg, S., Mesoporous silica nanoparticles: A comprehensive review on synthesis and recent advances. *Pharmaceutics* **2018**, *10* (3), 118.
17. Teoli, D.; Parisi, L.; Realdon, N.; Guglielmi, M.; Rosato, A.; Morpurgo, M., Wet sol-gel derived silica for controlled release of proteins. *Journal of controlled release* **2006**, *116* (3), 295-303.
18. Jin, W.; Brennan, J. D., Properties and Applications of Proteins Encapsulated Within Sol-Gel-Derived Materials. *ChemInform* **2002**, *33* (42), 295-295.
19. Gill, I., Bio-doped nanocomposite polymers: Sol-gel bioencapsulates. *Chem. Mat.* **2001**, *13* (10), 3404-3421.
20. Keeling-Tucker, T.; Brennan, J. D., Fluorescent Probes as Reporters on the Local Structure and Dynamics in Sol-Gel-Derived Nanocomposite Materials. *Chemistry of materials* **2001**, *13* (10), 3331-3350.
21. Dickey, F. H., Specific Adsorption. *The Journal of Physical Chemistry* **1955**, *59* (8), 695-707.
22. Braun, S. G., Editorial. *Mechanical Systems and Signal Processing* **1990**, *4* (1), 1.
23. Ellerby, L. M.; Nishida, C. R.; Nishida, F.; Yamanaka, S. A.; Dunn, B.; Valentine, J. S.; Zink, J. I., Encapsulation of Proteins in Transparent Porous Silicate Glasses Prepared by the Sol-Gel Method. *Science* **1992**, *255* (5048), 1113-1115.
24. Eggers, D. K.; Valentine, J. S., Molecular confinement influences protein structure and enhances thermal protein stability. *Protein Science* **2001**, *10* (2), 250-261.
25. Brennan, J. D.; Benjamin, D.; Dibattista, E.; Gulcev, M. D., Using Sugar and Amino Acid Additives to Stabilize Enzymes within Sol-Gel Derived Silica. *Chemistry of materials* **2003**, *15* (3), 737-745.
26. Wahid, A. A.; Doekhie, A.; Sartbaeva, A.; van Den Elsen, J. M. H., Ensilication Improves the Thermal Stability of the Tuberculosis Antigen Ag85b and an Sbi-Ag85b Vaccine Conjugate. *Scientific reports* **2019**, *9* (1), 11409-11409.
27. Yun-Chu, C.; Tristan, S.; Robert, H. H.; Aswin, D.; Françoise, K.; Stephen, A. W.; Karen, J. E.; Jean Van Den, E.; Geoffrey, D. H.; Kevin, J. M.; Asel, S., Thermal stability, storage and release of proteins with tailored fit in silica. *Scientific Reports* **2017**, *7* (1).
28. Boylan, J.; Chauhan, R.; Koneru, K.; Bansal, M.; Kalbfleisch, T.; Potnis, C. S.; Hartline, K.; Keynton, R. S.; Gupta, G., Bio-CaRGOS: capture and release gels for optimized storage of hemoglobin. *RSC Adv.* **2021**, *11* (22), 13034-13039.
29. Doekhie, A.; Slade, M. N.; Cliff, L.; Weaver, L.; Castaing, R.; Paulin, J.; Chen, Y. C.; Edler, K. J.; Koumanov, F.; Marchbank, K. J.; Van Den Elsen, J. M. H.; Sartbaeva, A., Thermal resilience of ensilicated lysozyme via calorimetric and in vivo analysis. *RSC Adv.* **2020**, *10* (50), 29789-29796.

30. Doekhie, A.; Dattani, R.; Chen, Y.; Yang, Y.; Smith, A.; Silve, A. P.; Koumanov, F.; Wells, S. A.; Edler, K.; Marchbank, K.; van Den Elsen, J.; Sartbaeva, A., Ensilicated tetanus antigen retains immunogenicity: in vivo study and time-resolved SAXS characterization. *Sci Rep* **2020**, *10* (1).
31. Gessner, B. D.; Beller, M.; Middaugh, J. P.; Whitford, G., ACUTE FLUORIDE POISONING FROM A PUBLIC WATER-SYSTEM. *N. Engl. J. Med.* **1994**, *330* (2), 95-99.
32. Ronda, L.; Bruno, S.; Campanini, B.; Mozzarelli, A.; Abbruzzetti, S.; Viappiani, C.; Cupane, A.; Levantino, M.; Bettati, S., Immobilization of proteins in silica gel: biochemical and biophysical properties. *Current Organic Chemistry* **2015**, *19* (17), 1653-1668.
33. Puddu, V.; Perry, C. C., Peptide Adsorption on Silica Nanoparticles: Evidence of Hydrophobic Interactions. *ACS Nano* **2012**, *6* (7), 6356-6363.
34. Tang, F.; Li, L.; Chen, D., Mesoporous Silica Nanoparticles: Synthesis, Biocompatibility and Drug Delivery. Weinheim, 2012; Vol. 24, pp 1504-1534.
35. Wang, G.; Wang, H.; Zhou, H.; Nian, Q.; Song, Z.; Deng, Y.; Wang, X.; Zhu, S.; Li, X.; Qin, C.; Tang, R., Hydrated Silica Exterior Produced by Biomimetic Silicification Confers Viral Vaccine Heat-Resistance. *ACS Nano* **2015**, *9* (1), 799-808.
36. Zhao, D.; Huo, Q.; Feng, J.; Chmelka, B. F.; Stucky, G. D., Nonionic triblock and star diblock copolymer and oligomeric surfactant syntheses of highly ordered, hydrothermally stable, mesoporous silica structures. *Journal of the American Chemical Society* **1998**, *120* (24), 6024-6036.
37. Tortajada, M.; Ramón, D.; Beltrán, D.; Amoros, P., Hierarchical bimodal porous silicas and organosilicas for enzyme immobilization. *Journal of Materials Chemistry* **2005**, *15* (35-36), 3859-3868.
38. Bernal, C.; Sierra, L.; Mesa, M., Improvement of thermal stability of β -galactosidase from *Bacillus circulans* by multipoint covalent immobilization in hierarchical macro-mesoporous silica. *Journal of molecular catalysis. B, Enzymatic* **2012**, *84*, 166-172.
39. Bernal, C.; Urrutia, P.; Illanes, A.; Wilson, L., Hierarchical meso-macroporous silica grafted with glyoxyl groups: opportunities for covalent immobilization of enzymes. *New biotechnology* **2013**, *30* (5), 500-506.
40. Ferreira, L.; Ramos, M. A.; Dordick, J. S.; Gil, M. H., Influence of different silica derivatives in the immobilization and stabilization of a *Bacillus licheniformis* protease (Subtilisin Carlsberg). *Journal of molecular catalysis. B, Enzymatic* **2003**, *21* (4-6), 189-199.
41. Nwagu, T. N.; Okolo, B. N.; Aoyagi, H., Immobilization of raw starch digesting amylase on silica gel: A comparative study. *African Journal of Biotechnology* **2011**, *10* (71), 15989-15997.
42. Wang, S.; Su, P.; Ding, F.; Yang, Y., Immobilization of cellulase on polyamidoamine dendrimer-grafted silica. *Journal of Molecular Catalysis B: Enzymatic* **2013**, *89*, 35-40.
43. Sahare, P.; Ayala, M.; Vazquez-Duhalt, R.; Pal, U.; Loni, A.; Canham, L.; Osorio, I.; Agarwal, V., Enhancement of Peroxidase Stability Against Oxidative Self-Inactivation by Co-immobilization with a Redox-Active Protein in Mesoporous Silicon and Silica Microparticles. *Nanoscale Research Letters* **2016**, *11* (1), 1-10.

44. Montoya, N. A.; Barr, K. E.; Morales, S. V.; Umana, J. E.; Ny, C.; Roth, R. E.; Reyes, E. J.; Kirchhoff, B. C.; Hartman, E. R.; Higgins, L. L., Protein Stabilization and Delivery: A Case Study of Invasion Plasmid Antigen D Adsorbed on Porous Silica. *Langmuir* **2020**.
45. Tavares, A. P.; Rodríguez, O.; Fernández-Fernández, M.; Domínguez, A.; Moldes, D.; Sanromán, M. A.; Macedo, E. A., Immobilization of laccase on modified silica: stabilization, thermal inactivation and kinetic behaviour in 1-ethyl-3-methylimidazolium ethylsulfate ionic liquid. *Bioresource technology* **2013**, *131*, 405-412.
46. Bernal, C.; Illanes, A.; Wilson, L., Heterofunctional hydrophilic–hydrophobic porous silica as support for multipoint covalent immobilization of lipases: application to lactulose palmitate synthesis. *Langmuir* **2014**, *30* (12), 3557-3566.
47. Arroyo, M.; Sánchez-Montero, J. M. a.; Sinisterra, J. V., Thermal stabilization of immobilized lipase B from *Candida antarctica* on different supports: Effect of water activity on enzymatic activity in organic media. *Enzyme and microbial technology* **1999**, *24* (1-2), 3-12.
48. Blanco, R. M.; Terreros, P.; Fernández-Pérez, M.; Otero, C.; Díaz-González, G., Functionalization of mesoporous silica for lipase immobilization: Characterization of the support and the catalysts. *Journal of Molecular Catalysis B: Enzymatic* **2004**, *30* (2), 83-93.
49. Itoh, T.; Ishii, R.; Matsuura, S.-i.; Mizuguchi, J.; Hamakawa, S.; Hanaoka, T.-a.; Tsunoda, T.; Mizukami, F., Enhancement in thermal stability and resistance to denaturants of lipase encapsulated in mesoporous silica with alkyltrimethylammonium (CTAB). *Colloids and Surfaces B: Biointerfaces* **2010**, *75* (2), 478-482.
50. Urabe, Y.; Shiomi, T.; Itoh, T.; Kawai, A.; Tsunoda, T.; Mizukami, F.; Sakaguchi, K., Encapsulation of Hemoglobin in Mesoporous Silica (FSM)—Enhanced Thermal Stability and Resistance to Denaturants. *ChemBioChem* **2007**, *8* (6), 668-674.
51. Ispas, C.; Sokolov, I.; Andreescu, S., Enzyme-functionalized mesoporous silica for bioanalytical applications. *Analytical and bioanalytical chemistry* **2009**, *393* (2), 543-554.
52. Blanco, R. M.; Calvete, J. J.; Guisán, J., Immobilization-stabilization of enzymes; variables that control the intensity of the trypsin (amine)-agarose (aldehyde) multipoint attachment. *Enzyme and microbial technology* **1989**, *11* (6), 353-359.
53. Sahu, J.; Acharya, J.; Meikap, B., Optimization of production conditions for activated carbons from Tamarind wood by zinc chloride using response surface methodology. *Bioresource technology* **2010**, *101* (6), 1974-1982.
54. Brito, M. J. P.; Veloso, C. M.; Bonomo, R. C. F.; Fontan, R. d. C. I.; Santos, L. S.; Monteiro, K. A., Activated carbons preparation from yellow mombin fruit stones for lipase immobilization. *Fuel Processing Technology* **2017**, *156*, 421-428.
55. Horikawa, T.; Kitakaze, Y.; Sekida, T.; Hayashi, J. i.; Katoh, M., Characteristics and humidity control capacity of activated carbon from bamboo. *Bioresource technology* **2010**, *101* (11), 3964-3969.
56. Ramani, K.; Boopathy, R.; Vidya, C.; Kennedy, L. J.; Velan, M.; Sekaran, G., Immobilisation of *Pseudomonas gessardii* acidic lipase derived from beef tallow onto mesoporous activated carbon and its application on hydrolysis of olive oil. *Process biochemistry* **2010**, *45* (6), 986-992.

57. Ramani, K.; Karthikeyan, S.; Boopathy, R.; Kennedy, L. J.; Mandal, A.; Sekaran, G., Surface functionalized mesoporous activated carbon for the immobilization of acidic lipase and their application to hydrolysis of waste cooked oil: isotherm and kinetic studies. *Process biochemistry* **2012**, *47* (3), 435-445.
58. Kumar, A. G.; Swarnalatha, S.; Kamatchi, P.; Kirubakaran, R.; Perinbam, K.; Sekaran, G., Immobilization of proteolytic enzyme on highly porous activated carbon derived from rice bran. *Journal of Porous Materials* **2009**, *16* (4), 439-445.
59. Kumar, A. G.; Swarnalatha, S.; Kamatchi, P.; Sekaran, G., Immobilization of high catalytic acid protease on functionalized mesoporous activated carbon particles. *Biochemical engineering journal* **2009**, *43* (2), 185-190.
60. Wang, Y.; Guan, Y.; Yang, Y.; Yu, P.; Huang, Y., Enhancing the stability of immobilized catalase on activated carbon with gelatin encapsulation. *Journal of Applied Polymer Science* **2013**, *130* (3), 1498-1502.
61. Zhang, C.; Gong, L.; Mao, Q.; Han, P.; Lu, X.; Qu, J., Laccase immobilization and surface modification of activated carbon fibers by bio-inspired poly-dopamine. *RSC advances* **2018**, *8* (26), 14414-14421.
62. Thiyagarajan, P.; Selvam, K.; Sudhakar, C.; Selvankumar, T., Enhancement of adsorption of magenta dye by immobilized laccase on functionalized biosynthesized activated carbon nanotubes. *Water, Air, & Soil Pollution* **2020**, *231* (7), 1-9.
63. Rahman, M. B. A.; Basri, M.; Hussein, M. Z.; Rahman, R. N. Z. R. A.; Yan, Y. K.; Salleh, A. B., Activated carbon as support for lipase immobilization. *Eurasian Chemical-Technological Journal* **2003**, *5* (2), 115-119.
64. Noritomi, H.; Kai, R.; Iwai, D.; Tanaka, H.; Kamiya, R.; Tanaka, M.; Muneki, K.; Kato, S., Increase in thermal stability of proteins adsorbed on biomass charcoal powder prepared from plant biomass wastes. *Journal of Biomedical Science and Engineering* **2011**, *04* (11), 692-698.
65. Wang, Q.; Zhou, L.; Jiang, Y.; Gao, J., Improved stability of the carbon nanotubes–enzyme bioconjugates by biomimetic silicification. *Enzyme and microbial technology* **2011**, *49* (1), 11-16.
66. Mahesh, M.; Arivizhivendhan, K.; Maharaja, P.; Boopathy, R.; Hamsavathani, V.; Sekaran, G., Production, purification and immobilization of pectinase from *Aspergillus ibericus* onto functionalized nanoporous activated carbon (FNAC) and its application on treatment of pectin containing wastewater. *Journal of Molecular Catalysis B: Enzymatic* **2016**, *133*, 43-54.
67. Wang, J.; Liu, J.; Cepra, G., Thermal stabilization of enzymes immobilized within carbon paste electrodes. *Analytical chemistry* **1997**, *69* (15), 3124-3127.
68. Vinogradov, V. V.; Avnir, D., Exceptional thermal stability of therapeutical enzymes entrapped in alumina sol–gel matrices. *Journal of Materials Chemistry B* **2014**, *2* (19), 2868-2873.
69. Vinogradov, V. V.; Avnir, D., Exceptional thermal stability of industrially-important enzymes by entrapment within nano-boehmite derived alumina. *RSC advances* **2015**, *5* (15), 10862-10868.

70. Drozdov, A. S.; Shapovalova, O. E.; Ivanovski, V.; Avnir, D.; Vinogradov, V. V., Entrapment of enzymes within sol–gel-derived magnetite. *Chemistry of Materials* **2016**, *28* (7), 2248-2253.
71. Rutenberg, A.; Vinogradov, V. V.; Avnir, D., Synthesis and enhanced thermal stability of albumins@ alumina: towards injectable sol–gel materials. *Chemical Communications* **2013**, *49* (50), 5636-5638.
72. Costa, S. A.; Tzanov, T.; Paar, A.; Gudelj, M.; Gübitz, G. M.; Cavaco-Paulo, A., Immobilization of catalases from *Bacillus SF* on alumina for the treatment of textile bleaching effluents. *Enzyme and Microbial Technology* **2001**, *28* (9-10), 815-819.
73. Askaripour, H.; Vossoughi, M.; Khajeh, K.; Alemzadeh, I., Magnetite nanoparticle as a support for stabilization of chondroitinase ABCI. *Artificial cells, nanomedicine, and biotechnology* **2019**, *47* (1), 2721-2728.
74. Yildirim, D.; Baran, E.; Ates, S.; Yazici, B.; Tukul, S. S., Improvement of activity and stability of *Rhizomucor miehei* lipase by immobilization on nanoporous aluminium oxide and potassium sulfate microcrystals and their applications in the synthesis of aroma esters. *Biocatalysis and Biotransformation* **2019**, *37* (3), 210-223.
75. Hyndman, D.; Burrell, R.; Lever, G.; Flynn, T. G., Protein immobilization to alumina supports: II. Papain immobilization to alumina via organophosphate linkers. *Biotechnology and bioengineering* **1992**, *40* (11), 1328-1336.
76. Nagar, S.; Mittal, A.; Kumar, D.; Kumar, L.; Gupta, V. K., Immobilization of xylanase on glutaraldehyde activated aluminum oxide pellets for increasing digestibility of poultry feed. *Process Biochemistry* **2012**, *47* (9), 1402-1410.
77. Tadeballi, S.; Yim, J.; Cao, S.; Wang, Z.; Naik, R. R.; Singamaneni, S., Metal–organic framework encapsulation for the preservation and photothermal enhancement of enzyme activity. *Small* **2018**, *14* (7), 1702382.
78. Wang, C.; Sun, H.; Luan, J.; Jiang, Q.; Tadeballi, S.; Morrissey, J. J.; Kharasch, E. D.; Singamaneni, S., Metal–organic framework encapsulation for biospecimen preservation. *Chemistry of Materials* **2018**, *30* (4), 1291-1300.
79. Phipps, J.; Chen, H.; Donovan, C.; Dominguez, D.; Morgan, S.; Weidman, B.; Fan, C.; Beyzavi, M. H., Catalytic Activity, Stability, and Loading Trends of Alcohol Dehydrogenase Enzyme Encapsulated in a Metal–Organic Framework. *ACS applied materials & interfaces* **2020**, *12* (23), 26084-26094.
80. Atirođlu, V.; Atirođlu, A.; Özacar, M., Immobilization of α -amylase enzyme on a protein@ metal–organic framework nanocomposite: A new strategy to develop the reusability and stability of the enzyme. *Food Chemistry* **2021**, *349*, 129127.
81. Zhou, Z.; Gao, Z.; Shen, H.; Li, M.; He, W.; Su, P.; Song, J.; Yang, Y., Metal–Organic Framework in Situ Post-Encapsulating DNA–Enzyme Composites on a Magnetic Carrier with High Stability and Reusability. *ACS applied materials & interfaces* **2020**, *12* (6), 7510-7517.
82. Du, Y.; Gao, J.; Liu, H.; Zhou, L.; Ma, L.; He, Y.; Huang, Z.; Jiang, Y., Enzyme@ silica nanoflower@ metal-organic framework hybrids: A novel type of integrated nanobiocatalysts with improved stability. *Nano Research* **2018**, *11* (8), 4380-4389.

83. Tuan Kob, T.; Ismail, M.; Abdul Rahman, M.; Cordova, K. E.; Mohammad Latif, M., Unraveling the Structural Dynamics of an Enzyme Encapsulated within a Metal–Organic Framework. *The Journal of Physical Chemistry B* **2020**, *124* (18), 3678-3685.
84. Wu, X.; Yang, C.; Ge, J., Green synthesis of enzyme/metal-organic framework composites with high stability in protein denaturing solvents. *Bioresources and bioprocessing* **2017**, *4* (1), 1-8.
85. Peng, S.; Liu, J.; Qin, Y.; Wang, H.; Cao, B.; Lu, L.; Yu, X., Metal–Organic Framework Encapsulating Hemoglobin as a High-Stable and Long-Circulating Oxygen Carriers to Treat Hemorrhagic Shock. *ACS applied materials & interfaces* **2019**, *11* (39), 35604-35612.
86. Wang, C.; Sudlow, G.; Wang, Z.; Cao, S.; Jiang, Q.; Neiner, A.; Morrissey, J. J.; Kharasch, E. D.; Achilefu, S.; Singamaneni, S., Metal-Organic Framework Encapsulation Preserves the Bioactivity of Protein Therapeutics. *Advanced healthcare materials* **2018**, *7* (22), 1800950.
87. Kaur, H.; Mohanta, G. C.; Gupta, V.; Kukkar, D.; Tyagi, S., Synthesis and characterization of ZIF-8 nanoparticles for controlled release of 6-mercaptopurine drug. *Journal of Drug Delivery Science and Technology* **2017**, *41*, 106-112.
88. Roberts, J. J.; Martens, P. J., 9 - Engineering biosynthetic cell encapsulation systems. In *Biosynthetic Polymers for Medical Applications*, Poole-Warren, L.; Martens, P.; Green, R., Eds. Woodhead Publishing: 2016; pp 205-239.
89. Gustavsson, P.-E.; Son, P.-O., Chapter 6 - Monolithic Polysaccharide Materials. In *Journal of Chromatography Library*, Švec, F.; Tennikova, T. B.; Deyl, Z., Eds. Elsevier: 2003; Vol. 67, pp 121-141.
90. Nwagu, T. N.; Okolo, B. N.; Aoyagi, H., Stabilization of a raw starch digesting amylase from *Aspergillus carbonarius* via immobilization on activated and non-activated agarose gel. *World Journal of Microbiology and Biotechnology* **2012**, *28* (1), 335-345.
91. Tripathi, P.; Kumari, A.; Rath, P.; Kayastha, A. M., Immobilization of α -amylase from mung beans (*Vigna radiata*) on Amberlite MB 150 and chitosan beads: A comparative study. *Journal of Molecular Catalysis B: Enzymatic* **2007**, *49* (1-4), 69-74.
92. Guisán, J. M.; Bastida, A.; Cuesta, C.; Fernandez-Lufuente, R.; Rosell, C. M., Immobilization-stabilization of α -chymotrypsin by covalent attachment to aldehyde-agarose gels. *Biotechnology and Bioengineering* **1991**, *38* (10), 1144-1152.
93. Vieira, M. F.; Vieira, A. M. S.; Zanin, G. M.; Tardioli, P. W.; Mateo, C.; Guisán, J. M., β -Glucosidase immobilized and stabilized on agarose matrix functionalized with distinct reactive groups. *Journal of Molecular Catalysis B: Enzymatic* **2011**, *69* (1-2), 47-53.
94. Spagna, G.; Barbagallo, R. N.; Pifferi, P. G.; Blanco, R. M.; Guisan, J. M., Stabilization of a β -glucosidase from *Aspergillus niger* by binding to an amine agarose gel. *Journal of Molecular Catalysis B: Enzymatic* **2000**, *11* (2-3), 63-69.
95. Tardioli, P. W.; Pedroche, J.; Giordano, R. L.; Fernández-Lafuente, R.; Guisan, J. M., Hydrolysis of proteins by immobilized-stabilized alcalase-glyoxyl agarose. *Biotechnology progress* **2003**, *19* (2), 352-360.

96. Tavano, O. L.; Fernandez-Lafuente, R.; Goulart, A. J.; Monti, R., Optimization of the immobilization of sweet potato amylase using glutaraldehyde-agarose support. Characterization of the immobilized enzyme. *Process Biochemistry* **2013**, *48* (7), 1054-1058.
97. Megías, C.; Pedroche, J.; Yust, M. d. M.; Alaiz, M.; Girón-Calle, J.; Millán, F.; Vioque, J., Immobilization of angiotensin-converting enzyme on glyoxyl-agarose. *Journal of agricultural and food chemistry* **2006**, *54* (13), 4641-4645.
98. Siar, E.-H.; Arana-Peña, S.; Barbosa, O.; Zidoune, M. N.; Fernandez-Lafuente, R., Immobilization/stabilization of ficin extract on glutaraldehyde-activated agarose beads. Variables that control the final stability and activity in protein hydrolyses. *Catalysts* **2018**, *8* (4), 149.
99. Tardioli, P. W.; Vieira, M. F.; Vieira, A. M. S.; Zanin, G. M.; Betancor, L.; Mateo, C.; Fernández-Lorente, G.; Guisán, J. M., Immobilization–stabilization of glucoamylase: Chemical modification of the enzyme surface followed by covalent attachment on highly activated glyoxyl-agarose supports. *Process Biochemistry* **2011**, *46* (1), 409-412.
100. Xu, R.; Zhou, Q.; Li, F.; Zhang, B., Laccase immobilization on chitosan/poly (vinyl alcohol) composite nanofibrous membranes for 2, 4-dichlorophenol removal. *Chemical engineering journal* **2013**, *222*, 321-329.
101. Fernandez-Lopez, L.; Rueda, N.; Bartolome-Cabrero, R.; Rodriguez, M. D.; Albuquerque, T. L.; dos Santos, J. C.; Barbosa, O.; Fernandez-Lafuente, R., Improved immobilization and stabilization of lipase from *Rhizomucor miehei* on octyl-glyoxyl agarose beads by using CaCl₂. *Process Biochemistry* **2016**, *51* (1), 48-52.
102. Peirce, S.; Tacias-Pascacio, V. G.; Russo, M. E.; Marzocchella, A.; Virgen-Ortíz, J. J.; Fernandez-Lafuente, R., Stabilization of *Candida antarctica* lipase B (CALB) immobilized on octyl agarose by treatment with polyethyleneimine (PEI). *Molecules* **2016**, *21* (6), 751.
103. Rodrigues, D. S.; Mendes, A. A.; Adriano, W. S.; Gonçalves, L. R.; Giordano, R. L., Multipoint covalent immobilization of microbial lipase on chitosan and agarose activated by different methods. *Journal of Molecular Catalysis B: Enzymatic* **2008**, *51* (3-4), 100-109.
104. Fernandez-Lopez, L.; Pedrero, S. G.; Lopez-Carrobles, N.; Virgen-Ortíz, J. J.; Gorines, B. C.; Otero, C.; Fernandez-Lafuente, R., Physical crosslinking of lipase from *Rhizomucor miehei* immobilized on octyl agarose via coating with ionic polymers: Avoiding enzyme release from the support. *Process Biochemistry* **2017**, *54*, 81-88.
105. Rios, N. S.; Mendez-Sanchez, C.; Arana-Peña, S.; Rueda, N.; Ortiz, C.; Gonçalves, L. R.; Fernandez-Lafuente, R., Immobilization of lipase from *Pseudomonas fluorescens* on glyoxyl-octyl-agarose beads: Improved stability and reusability. *Biochimica et Biophysica Acta (BBA)-Proteins and Proteomics* **2019**, *1867* (9), 741-747.
106. Tiago, L.; Rueda, N.; dos Santos, J. C.; Barbosa, O.; Ortiz, C.; Binay, B.; Özdemir, E.; Gonçalves, L. R.; Fernandez-Lafuente, R., Easy stabilization of interfacially activated lipases using heterofunctional divinyl sulfone activated-octyl agarose beads. Modulation of the immobilized enzymes by altering their nanoenvironment. *Process Biochemistry* **2016**, *51* (7), 865-874.
107. Rodrigues, R. C.; Godoy, C. A.; Volpato, G.; Ayub, M. A.; Fernandez-Lafuente, R.; Guisan, J. M., Immobilization–stabilization of the lipase from *Thermomyces lanuginosus*: Critical role of chemical amination. *Process Biochemistry* **2009**, *44* (9), 963-968.

108. Fernández-Lafuente, R.; Rosell, C. M.; Alvaro, G.; Guisán, J., Additional stabilization of penicillin G acylase-agarose derivatives by controlled chemical modification with formaldehyde. *Enzyme and microbial technology* **1992**, *14* (6), 489-495.
109. Younus, H.; Owais, M.; Rao, D. N.; Saleemuddin, M., Stabilization of pancreatic ribonuclease A by immobilization on Sepharose-linked antibodies that recognize the labile region of the enzyme. *Biochimica et biophysica acta, Protein structure and molecular enzymology* **2001**, *1548* (1), 114-120.
110. Manrich, A.; Komesu, A.; Adriano, W. S.; Tardioli, P. W.; Giordano, R. L. C., Immobilization and stabilization of xylanase by multipoint covalent attachment on agarose and on chitosan supports. *Applied biochemistry and biotechnology* **2010**, *161* (1), 455-467.
111. Kumari, A.; Kayastha, A. M., Immobilization of soybean (Glycine max) α -amylase onto Chitosan and Amberlite MB-150 beads: Optimization and characterization. *Journal of Molecular Catalysis B: Enzymatic* **2011**, *69* (1-2), 8-14.
112. Dwevedi, A.; Kayastha, A. M., Optimal immobilization of β -galactosidase from Pea (PsBGAL) onto Sephadex and chitosan beads using response surface methodology and its applications. *Bioresource Technology* **2009**, *100* (10), 2667-2675.
113. Klein, M. P.; Nunes, M. R.; Rodrigues, R. C.; Benvenuti, E. V.; Costa, T. M.; Hertz, P. F.; Ninow, J. L., Effect of the support size on the properties of β -galactosidase immobilized on chitosan: advantages and disadvantages of macro and nanoparticles. *Biomacromolecules* **2012**, *13* (8), 2456-2464.
114. Nguyen, V. D.; Styevkó, G.; Madaras, E.; Haktanirlar, G.; Tran, A. T.; Bujna, E.; Dam, M. S.; Nguyen, Q. D., Immobilization of β -galactosidase on chitosan-coated magnetic nanoparticles and its application for synthesis of lactulose-based galactooligosaccharides. *Process Biochemistry* **2019**, *84*, 30-38.
115. Urrutia, P.; Bernal, C.; Wilson, L.; Illanes, A., Use of chitosan heterofunctionality for enzyme immobilization: β -galactosidase immobilization for galacto-oligosaccharide synthesis. *International journal of biological macromolecules* **2018**, *116*, 182-193.
116. dos Santos Kimberle, P.; Carolina, M.-S.; Ana, I. S. B.; Luciana, R. B. G., Modifying alcalase activity and stability by immobilization onto chitosan aiming at the production of bioactive peptides by hydrolysis of tilapia skin gelatin. *Process Biochemistry* **2020**, *97*, 27-36.
117. Wang, S.-n.; Zhang, C.-r.; Qi, B.-k.; Sui, X.-n.; Jiang, L.-z.; Li, Y.; Wang, Z.-j.; Feng, H.-x.; Wang, R.; Zhang, Q.-z., Immobilized alcalase alkaline protease on the magnetic chitosan nanoparticles used for soy protein isolate hydrolysis. *European Food Research and Technology* **2014**, *239* (6), 1051-1059.
118. Li, G.-y.; Li, Y.-j.; Huang, K.-l.; Zhong, M., Surface functionalization of chitosan-coated magnetic nanoparticles for covalent immobilization of yeast alcohol dehydrogenase from *Saccharomyces cerevisiae*. *Journal of magnetism and magnetic materials* **2010**, *322* (24), 3862-3868.
119. Zhou, J. Q.; Wang, J. W., Immobilization of alliinase with a water soluble-insoluble reversible N-succinyl-chitosan for alliin production. *Enzyme and Microbial Technology* **2009**, *45* (4), 299-304.

120. Çetinus, Ş. A.; Öztop, H. N., Immobilization of catalase on chitosan film. *Enzyme and microbial technology* **2000**, *26* (7), 497-501.
121. Çetinus, Ş. A.; Şahin, E.; Saraydin, D., Preparation of Cu (II) adsorbed chitosan beads for catalase immobilization. *Food Chemistry* **2009**, *114* (3), 962-969.
122. Kaushal, J.; Singh, G.; Arya, S. K., Immobilization of catalase onto chitosan and chitosan–bentonite complex: a comparative study. *Biotechnology Reports* **2018**, *18*, e00258.
123. Bayramoglu, G.; Arica, M. Y., Reversible immobilization of catalase on fibrous polymer grafted and metal chelated chitosan membrane. *Journal of Molecular Catalysis B: Enzymatic* **2010**, *62* (3-4), 297-304.
124. Çetinus, Ş. A.; Öztop, H. N., Immobilization of catalase into chemically crosslinked chitosan beads. *Enzyme and Microbial Technology* **2003**, *32* (7), 889-894.
125. Inanan, T., Research Conducted at Aksaray University Has Updated Our Knowledge about Nanostructures (Chitosan Co-polymeric Nanostructures for Catalase Immobilization). *Life Science Weekly* **2019**, 1061.
126. Çetinus, Ş. A.; Öztop, H. N.; Saraydin, D., Immobilization of catalase onto chitosan and cibacron blue F3GA attached chitosan beads. *Enzyme and microbial technology* **2007**, *41* (4), 447-454.
127. Zang, L.; Qiu, J.; Wu, X.; Zhang, W.; Sakai, E.; Wei, Y., Preparation of magnetic chitosan nanoparticles as support for cellulase immobilization. *Industrial & engineering chemistry research* **2014**, *53* (9), 3448-3454.
128. Wang, J.; Zhao, G.; Li, Y.; Liu, X.; Hou, P., Reversible immobilization of glucoamylase onto magnetic chitosan nanocarriers. *Applied microbiology and biotechnology* **2013**, *97* (2), 681-692.
129. Hsieh, H.-J.; Liu, P.-C.; Liao, W.-J., Immobilization of invertase via carbohydrate moiety on chitosan to enhance its thermal stability. *Biotechnology letters* **2000**, *22* (18), 1459-1464.
130. Valerio, S. G.; Alves, J. S.; Klein, M. P.; Rodrigues, R. C.; Hertz, P. F., High operational stability of invertase from *Saccharomyces cerevisiae* immobilized on chitosan nanoparticles. *Carbohydrate polymers* **2013**, *92* (1), 462-468.
131. Srivastava, B.; Singh, H.; Khatri, M.; Singh, G.; Arya, S. K., Immobilization of keratinase on chitosan grafted- β -cyclodextrin for the improvement of the enzyme properties and application of free keratinase in the textile industry. *International Journal of Biological Macromolecules* **2020**, *165*, 1099-1110.
132. Lin, J.; Fan, L.; Miao, R.; Le, X.; Chen, S.; Zhou, X., Enhancing catalytic performance of laccase via immobilization on chitosan/CeO₂ microspheres. *International journal of biological macromolecules* **2015**, *78*, 1-8.
133. Fang, H.; Huang, J.; Ding, L.; Li, M.; Chen, Z., Preparation of magnetic chitosan nanoparticles and immobilization of laccase. *Journal of Wuhan University of Technology-Mater. Sci. Ed.* **2009**, *24* (1), 42-47.
134. Hung, T.-C.; Giridhar, R.; Chiou, S.-H.; Wu, W.-T., Binary immobilization of *Candida rugosa* lipase on chitosan. *Journal of Molecular Catalysis B: Enzymatic* **2003**, *26* (1-2), 69-78.

135. Chiou, S.-H.; Wu, W.-T., Immobilization of *Candida rugosa* lipase on chitosan with activation of the hydroxyl groups. *Biomaterials* **2004**, *25* (2), 197-204.
136. Ye, P.; Xu, Z.-K.; Che, A.-F.; Wu, J.; Seta, P., Chitosan-tethered poly(acrylonitrile- co-maleic acid) hollow fiber membrane for lipase immobilization. *Biomaterials* **2005**, *26* (32), 6394-6403.
137. Urrutia, P.; Arrieta, R.; Alvarez, L.; Cardenas, C.; Mesa, M.; Wilson, L., Immobilization of lipases in hydrophobic chitosan for selective hydrolysis of fish oil: The impact of support functionalization on lipase activity, selectivity and stability. *International journal of biological macromolecules* **2018**, *108*, 674-686.
138. Silva, J.; Macedo, G.; Rodrigues, D.; Giordano, R.; Gonçalves, L., Immobilization of *Candida antarctica* lipase B by covalent attachment on chitosan-based hydrogels using different support activation strategies. *Biochemical Engineering Journal* **2012**, *60*, 16-24.
139. Huang, X.-J.; Ge, D.; Xu, Z.-K., Preparation and characterization of stable chitosan nanofibrous membrane for lipase immobilization. *European Polymer Journal* **2007**, *43* (9), 3710-3718.
140. Kuo, C.-H.; Liu, Y.-C.; Chang, C.-M. J.; Chen, J.-H.; Chang, C.; Shieh, C.-J., Optimum conditions for lipase immobilization on chitosan-coated Fe₃O₄ nanoparticles. *Carbohydrate Polymers* **2012**, *87* (4), 2538-2545.
141. Altun, G. D.; Cetinus, S. A., Immobilization of pepsin on chitosan beads. *Food chemistry* **2007**, *100* (3), 964-971.
142. Singh, A. N.; Singh, S.; Suthar, N.; Dubey, V. K., Glutaraldehyde-activated chitosan matrix for immobilization of a novel cysteine protease, procerain B. *Journal of agricultural and food chemistry* **2011**, *59* (11), 6256-6262.
143. Kamburov, M.; Lalov, I., Preparation of chitosan beads for trypsin immobilization. *Biotechnology & Biotechnological Equipment* **2012**, *26* (sup1), 156-163.
144. Manrich, A.; Galvão, C. M.; Jesus, C. D.; Giordano, R. C.; Giordano, R. L., Immobilization of trypsin on chitosan gels: Use of different activation protocols and comparison with other supports. *International Journal of Biological Macromolecules* **2008**, *43* (1), 54-61.
145. Kayastha, A. M.; Srivastava, P. K., Pigeonpea (*Cajanus cajan* L.) urease immobilized on glutaraldehyde-activated chitosan beads and its analytical applications. *Applied biochemistry and biotechnology* **2001**, *96* (1), 41-53.
146. Kumar, S.; Dwevedi, A.; Kayastha, A. M., Immobilization of soybean (*Glycine max*) urease on alginate and chitosan beads showing improved stability: Analytical applications. *Journal of Molecular Catalysis B: Enzymatic* **2009**, *58* (1-4), 138-145.
147. Mai, T. H. A., Biochemical studies on the immobilized lactase in the combined alginate–carboxymethyl cellulose gel. *Biochemical Engineering Journal* **2013**, *74*, 81-87.
148. Hung, C.-P.; Lo, H.-F.; Hsu, W.-H.; Chen, S.-C.; Lin, L.-L., Immobilization of *Escherichia coli* novablue γ -glutamyltranspeptidase in Ca-alginate-k-carrageenan beads. *Applied biochemistry and biotechnology* **2008**, *150* (2), 157-170.

149. Quiroga, E.; Illanes, C. O.; Ochoa, N. A.; Barberis, S., Performance improvement of araujiain, a cystein phytoprotease, by immobilization within calcium alginate beads. *Process Biochemistry* **2011**, *46* (4), 1029-1034.
150. Ortega, N.; Perez-Mateos, M.; Pilar, M. a. C.; Busto, M. a. D., Neutrase immobilization on alginate– glutaraldehyde beads by covalent attachment. *Journal of agricultural and food chemistry* **2009**, *57* (1), 109-115.
151. Taqieddin, E.; Amiji, M., Enzyme immobilization in novel alginate–chitosan core-shell microcapsules. *Biomaterials* **2004**, *25* (10), 1937-1945.
152. Li, G.-y.; Li, Y.-j., Immobilization of *Saccharomyces cerevisiae* alcohol dehydrogenase on hybrid alginate–chitosan beads. *International Journal of Biological Macromolecules* **2010**, *47* (1), 21-26.
153. Panescu, P. H.; Ko, J. H.; Maynard, H. D., Scalable Trehalose-Functionalized Hydrogel Synthesis for High-Temperature Protection of Enzymes. *Macromolecular Materials and Engineering* **2019**, *304* (6), 1800782.
154. Lee, J.; Ko, J. H.; Mansfield, K. M.; Nauka, P. C.; Bat, E.; Maynard, H. D., Glucose-Responsive Trehalose Hydrogel for Insulin Stabilization and Delivery. *Macromolecular bioscience* **2018**, *18* (5), 1700372.
155. Lee, J.; Ko, J. H.; Lin, E.-W.; Wallace, P.; Ruch, F.; Maynard, H. D., Trehalose hydrogels for stabilization of enzymes to heat. *Polym Chem* **2015**, *6* (18), 3443-3448.
156. Gómez, L.; Ramírez, H. L.; Villalonga, M. L.; Hernández, J.; Villalonga, R., Immobilization of chitosan-modified invertase on alginate-coated chitin support via polyelectrolyte complex formation. *Enzyme and Microbial Technology* **2006**, *38* (1-2), 22-27.
157. Gomez, L.; Ramírez, H. L.; Neira-Carrillo, A.; Villalonga, R., Polyelectrolyte complex formation mediated immobilization of chitosan-invertase neoglycoconjugate on pectin-coated chitin. *Bioprocess and Biosystems Engineering* **2006**, *28* (6), 387-395.
158. Meis, C. M.; Salzman, E. E.; Maikawa, C. L.; Smith, A. A.; Mann, J. L.; Grosskopf, A. K.; Appel, E. A., Self-Assembled, Dilution-Responsive Hydrogels for Enhanced Thermal Stability of Insulin Biopharmaceuticals. *ACS Biomaterials Science & Engineering* **2020**.
159. Wang, Y.; Hsieh, Y. L., Enzyme immobilization to ultra-fine cellulose fibers via amphiphilic polyethylene glycol spacers. *Journal of Polymer Science Part A: Polymer Chemistry* **2004**, *42* (17), 4289-4299.
160. Lee, J.; Ko, J. H.; Mansfield, K. M.; Nauka, P. C.; Bat, E.; Maynard, H. D., Glucose-Responsive Trehalose Hydrogel for Insulin Stabilization and Delivery. *Macromolecular Bioscience* **2018**, *18* (5), n/a-n/a.
161. Li, X.; Wang, X.; Ye, G.; Xia, W.; Wang, X., Polystyrene-based diazonium salt as adhesive: A new approach for enzyme immobilization on polymeric supports. *Polymer* **2010**, *51* (4), 860-867.
162. Sridhar, B. V.; Janczy, J. R.; Hatlevik, Ø.; Wolfson, G.; Anseth, K. S.; Tibbitt, M. W., Thermal Stabilization of Biologics with Photoresponsive Hydrogels. *Biomacromolecules* **2018**, *19* (3), 740-747.

163. Santos, J. C.; Nunes, G. F.; Moreira, A. B.; Perez, V. H.; de Castro, H. F., Characterization of *Candida rugosa* lipase immobilized on poly (N-methylolacrylamide) and its application in butyl butyrate synthesis. *Chemical Engineering & Technology: Industrial Chemistry-Plant Equipment-Process Engineering-Biotechnology* **2007**, *30* (9), 1255-1261.
164. Yadavalli, N. S.; Borodinov, N.; Choudhury, C. K.; Quiñones-Ruiz, T.; Laradji, A. M.; Tu, S.; Lednev, I. K.; Kuksenok, O.; Luzinov, I.; Minko, S., Thermal stabilization of enzymes with molecular brushes. *ACS Catalysis* **2017**, *7* (12), 8675-8684.
165. Dessouki, A. M.; Issa, G. I.; Atia, K. S., Pullulanase immobilization on natural and synthetic polymers. *Journal of Chemical Technology & Biotechnology* **2001**, *76* (7), 700-706.
166. Marquart, M. E.; Picking, W. L.; Picking, W. D., Structural Analysis of Invasion Plasmid Antigen D (Ipad) from *Shigella flexneri*. *Biochemical and Biophysical Research Communications* **1995**, *214* (3), 963-970.
167. Webb, P. A.; Orr, C., *Analytical methods in fine particle technology*. Micromeritics Instrument Corp: 1997.
168. Gasteiger, E.; Hoogland, C.; Gattiker, A.; Duvaud, S.; Wilkins, M. R.; Appel, R. D.; Bairoch, A., *Protein Identification and Analysis Tools on the ExPASy Server*. 2005.
169. Bastús, N. G.; Comenge, J.; Puentes, V. c., Kinetically Controlled Seeded Growth Synthesis of Citrate-Stabilized Gold Nanoparticles of up to 200 nm: Size Focusing versus Ostwald Ripening. *Langmuir* **2011**, *27* (17), 11098-11105.
170. Espina, M.; Olive, A. J.; Kenjale, R.; Moore, D. S.; Ausar, S. F.; Kaminski, R. W.; Oaks, E. V.; Middaugh, C. R.; Picking, W. D.; Picking, W. L., IpaD Localizes to the Tip of the Type III Secretion System Needle of *Shigella flexneri*. *Infection and Immunity* **2006**, *74* (8), 4391.
171. Kotloff, K.; Winickoff, J. P.; Ivanoff, B.; Clemens, J. D.; Swerdlow, D. L.; Sansonetti, P.; Adak, G.; Levine, M. M., Global burden of *Shigella* infections: implications for vaccine development and implementation of control strategies. *Bull. World Health Organ.* **1999**, *77* (8), 651-666.
172. Dupont, H. L.; Levine, M. M.; Hornick, R. B.; Formal, S. B., Inoculum size in shigellosis and implications for expected mode of transmission. *The Journal of infectious diseases* **1989**, *159* (6), 1126.
173. Zhang, L., Investigation of the structure and function of type III secretion needle and tip proteins. Picking, W. D.; De Guzman, R.; Kuczera, K.; Middaugh, R.; Richter, M., Eds. ProQuest Dissertations Publishing: 2009.
174. Espina, M.; Ausar, S. F.; Middaugh, C. R.; Picking, W. D.; Picking, W. L., Spectroscopic and calorimetric analyses of invasion plasmid antigen D (IpaD) from *Shigella flexneri* reveal the presence of two structural domains. *Biochemistry* **2006**, *45* (30), 9219-9227.
175. Epler, C. R.; Dickenson, N. E.; Olive, A. J.; Picking, W. L.; Picking, W. D., Liposomes Recruit IpaC to the *Shigella flexneri* Type III Secretion Apparatus Needle as a Final Step in Secretion Induction. *Infection and Immunity* **2009**, *77* (7), 2754.
176. Martinez-Becerra, F.; Kissmann, J.; Diaz-Mcnair, J.; Choudhari, S.; Quick, A.; Mellado-Sanchez, G.; Clements, J. D.; Pasetti, M.; Picking, W., Broadly Protective *Shigella* Vaccine Based on Type III Secretion Apparatus Proteins. *Infect. Immun.* **2012**, *80* (3), 1222-1231.

177. Kotloff, K. L.; Losonsky, G. A.; Nataro, J. P.; Wasserman, S. S.; Hale, T. L.; Taylor, D. N.; Newland, J. W.; Sadoff, J. C.; Formal, S. B.; Levine, M. M., Evaluation of the safety, immunogenicity, and efficacy in healthy adults of four doses of live oral hybrid *Escherichia coli*-*Shigella flexneri* 2a vaccine strain EcSf2a-2. *Vaccine* **1995**, *13* (5), 495-502.
178. Barnoy, S.; Jeong, K. I.; Helm, R. F.; Suvarnapunya, A. E.; Ranallo, R. T.; Tzipori, S.; Venkatesan, M. M., Characterization of WRSs2 and WRSs3, new second-generation virG(icsA)-based *Shigella sonnei* vaccine candidates with the potential for reduced reactogenicity. *Vaccine* **2010**, *28* (6), 1642-1654.
179. Cohen, D.; Ashkenazi, S.; Green, M.; Lerman, Y.; Slepon, R.; Robin, G.; Orr, N.; Taylor, D. N.; Sadoff, J. C.; Chu, C.; Shiloach, J.; Schneerson, R.; Robbins, J. B., Safety and immunogenicity of investigational *Shigella* conjugate vaccines in Israeli volunteers. *Infection and Immunity* **1996**, *64* (10), 4074.
180. Katz, D. E.; Coster, T. S.; Wolf, M. K.; Trespalacios, F. C.; Cohen, D.; Robins, G.; Hartman, A. B.; Venkatesan, M. M.; Taylor, D. N.; Hale, T. L., Two Studies Evaluating the Safety and Immunogenicity of a Live, Attenuated *Shigella flexneri* 2a Vaccine (SC602) and Excretion of Vaccine Organisms in North American Volunteers. *Infection and Immunity* **2004**, *72* (2), 923.
181. Cam, P. D.; Pal, T.; Lindberg, A. A., Immune response against lipopolysaccharide and invasion plasmid-coded antigens of shigellae in Vietnamese and Swedish dysenteric patients. *Journal of Clinical Microbiology* **1993**, *31* (2), 454.
182. Samandari, T.; Kotloff, K. L.; Losonsky, G. A.; Picking, W. D.; Sansonetti, P. J.; Levine, M. M.; Sztein, M. B., Production of IFN-gamma and IL-10 to *Shigella* invasins by mononuclear cells from volunteers orally inoculated with a Shiga toxin-deleted *Shigella dysenteriae* type 1 strain. *Journal of immunology (Baltimore, Md. : 1950)* **2000**, *164* (4), 2221.
183. Johnson, S.; Roversi, P.; Espina, M.; Olive, A. J.; Deane, J. E.; Birket, S.; Field, T.; Picking, W. D.; Blocker, A. J.; Galyov, E. E.; Picking, W. L.; Lea, S. M., Self-chaperoning of the Type III Secretion System Needle Tip Proteins IpaD and BipD. *American Society for Biochemistry and Molecular Biology*: 2007.
184. Rawlings, J. B. a., Chemical reactor analysis and design fundamentals. Second edition. ed.; Ekerdt, J. G. a., Ed. Madison, Wisconsin : Nob Hill Publishing: 2012.
185. Berman, H. M.; Westbrook, J.; Feng, Z.; Gilliland, G.; Bhat, T. N.; Weissig, H.; Shindyalov, I. N.; Bourne, P. E., The Protein Data Bank. *Nucleic Acids Research* **2000**, *28* (1), 235-242.
186. Saha, K.; Agasti, S. S.; Kim, C.; Li, X.; Rotello, V. M., Gold Nanoparticles in Chemical and Biological Sensing. *Chemical Reviews* **2012**, *112* (5), 2739-2779.
187. Carabineiro, S. A. C., Applications of Gold Nanoparticles in Nanomedicine: Recent Advances in Vaccines. *Molecules (Basel, Switzerland)* **2017**, *22* (5).
188. Kocherbitov, V.; Veryazov, V.; Söderman, O., Hydration of trimethylamine- N-oxide and of dimethyldodecylamine- N-oxide: An ab initio study. *Journal of Molecular Structure: THEOCHEM* **2007**, *808* (1), 111-118.

189. Nakanishi, K.; Sakiyama, T.; Imamura, K., On the adsorption of proteins on solid surfaces, a common but very complicated phenomenon. 2001; Vol. 91, pp 233-244.
190. Karlsson, M.; Martensson, L.; Jonsson, B.; Carlsson, U., Adsorption of human carbonic anhydrase II variants to silica nanoparticles occur stepwise: Binding is followed by successive conformational changes to a molten-globule-like state. *Langmuir* **2000**, *16* (22), 8470-8479.
191. Vertegel, A. A.; Siegel, R. W.; Dordick, J. S., Silica nanoparticle size influences the structure and enzymatic activity of adsorbed lysozyme. *Langmuir : the ACS journal of surfaces and colloids* **2004**, *20* (16), 6800-6807.
192. Billsten, P.; Wahlgren, M.; Arnebrant, T.; McGuire, J.; Elwing, H., Structural Changes of T4 Lysozyme upon Adsorption to Silica Nanoparticles Measured by Circular Dichroism. *Journal of Colloid And Interface Science* **1995**, *175* (1), 77-82.
193. González-Chávez, S. A.; Arévalo-Gallegos, S.; Rascón-Cruz, Q., Lactoferrin: structure, function and applications. *International journal of antimicrobial agents* **2009**, *33* (4), 301. e1-301. e8.
194. Hao, L.; Shan, Q.; Wei, J.; Ma, F.; Sun, P., Lactoferrin: major physiological functions and applications. *Current Protein and Peptide Science* **2019**, *20* (2), 139-144.
195. Mayeur, S.; Spahis, S.; Pouliot, Y.; Levy, E., Lactoferrin, a pleiotropic protein in health and disease. *Antioxidants & redox signaling* **2016**, *24* (14), 813-836.
196. Ochoa, T. J.; Chea-Woo, E.; Campos, M.; Pecho, I.; Prada, A.; McMahan, R. J.; Cleary, T. G., Impact of lactoferrin supplementation on growth and prevalence of *Giardia* colonization in children. *Clinical infectious diseases* **2008**, *46* (12), 1881-1883.
197. King Jr, J. C.; Cummings, G. E.; Guo, N.; Trivedi, L.; Readmond, B. X.; Keane, V.; Feigelman, S.; de Waard, R., A double-blind, placebo-controlled, pilot study of bovine lactoferrin supplementation in bottle-fed infants. *Journal of pediatric gastroenterology and nutrition* **2007**, *44* (2), 245-251.
198. Ochoa, T. J.; Pezo, A.; Cruz, K.; Chea-Woo, E.; Cleary, T. G., Clinical studies of lactoferrin in children. *Biochemistry and Cell Biology* **2012**, *90* (3), 457-467.
199. Yen, C.-C.; Shen, C.-J.; Hsu, W.-H.; Chang, Y.-H.; Lin, H.-T.; Chen, H.-L.; Chen, C.-M., Lactoferrin: an iron-binding antimicrobial protein against *Escherichia coli* infection. *Biometals* **2011**, *24* (4), 585-594.
200. Viani, R. M.; Gutteberg, T. J.; Lathey, J. L.; Spector, S. A., Lactoferrin inhibits HIV-1 replication in vitro and exhibits synergy when combined with zidovudine. *Aids* **1999**, *13* (10), 1273.
201. Kaito, M.; Iwasa, M.; Fujita, N.; Kobayashi, Y.; Kojima, Y.; Ikoma, J.; Imoto, I.; Adachi, Y.; Hamano, H.; Yamauchi, K., Effect of lactoferrin in patients with chronic hepatitis C: combination therapy with interferon and ribavirin. *Journal of gastroenterology and hepatology* **2007**, *22* (11), 1894-1897.
202. Van der Strate, B.; Beljaars, L.; Molema, G.; Harmsen, M.; Meijer, D., Antiviral activities of lactoferrin. *Antiviral research* **2001**, *52* (3), 225-239.

203. Baker, E.; Baker, H., Lactoferrin. *Cellular and Molecular Life Sciences* **2005**, *62* (22), 2531-2539.
204. Castellino, F. J.; Fish, W. W.; Mann, K. G., Structural studies on bovine lactoferrin. *Journal of Biological Chemistry* **1970**, *245* (17), 4269-4275.
205. Dinarvand, R.; Moghadam, S.; Sheikhi, A.; Atyabi, F., Effect of surfactant HLB and different formulation variables on the properties of poly-D, L-lactide microspheres of naltrexone prepared by double emulsion technique. *Journal of microencapsulation* **2005**, *22* (2), 139-151.
206. Das, A.; Mitra, R. K., Formulation and characterization of a biocompatible microemulsion composed of mixed surfactants: lecithin and Triton X-100. *Colloid and Polymer Science* **2014**, *292* (3), 635-644.
207. Tiller, G. E.; Mueller, T. J.; Dockter, M. E.; Struve, W. G., Hydrogenation of Triton X-100 eliminates its fluorescence and ultraviolet light absorption while preserving its detergent properties. *Analytical biochemistry* **1984**, *141* (1), 262-266.
208. Paradies, H. H., Shape and size of a nonionic surfactant micelle. Triton X-100 in aqueous solution. *The Journal of Physical Chemistry* **1980**, *84* (6), 599-607.

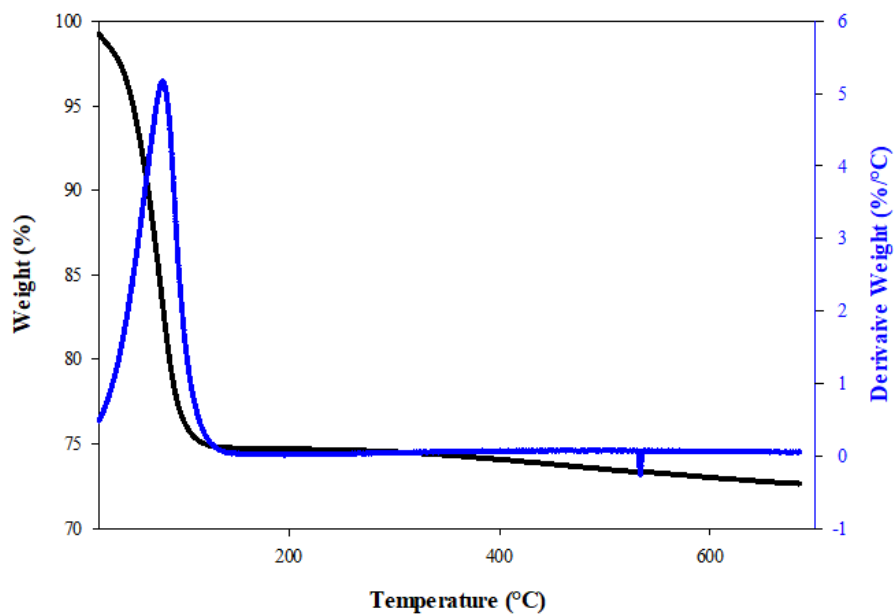
Appendix A: TGA Curves of Silica Samples and FTIR of Native IpaD in PBS

Figure A.1. TGA curves of weight % (black) and derivative weight (blue) for silica sample SA1

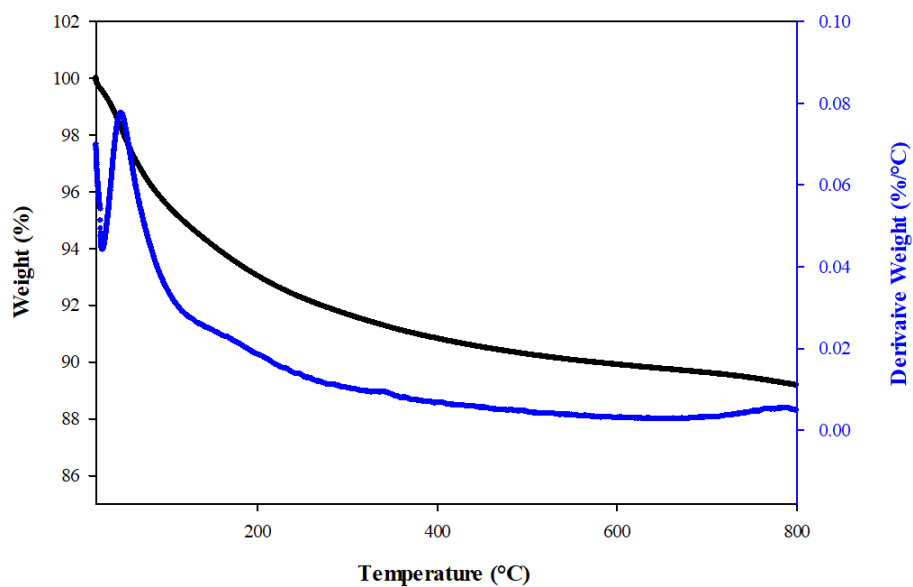


Figure A.2. TGA curves of weight % (black) and derivative weight (blue) for silica sample SA2

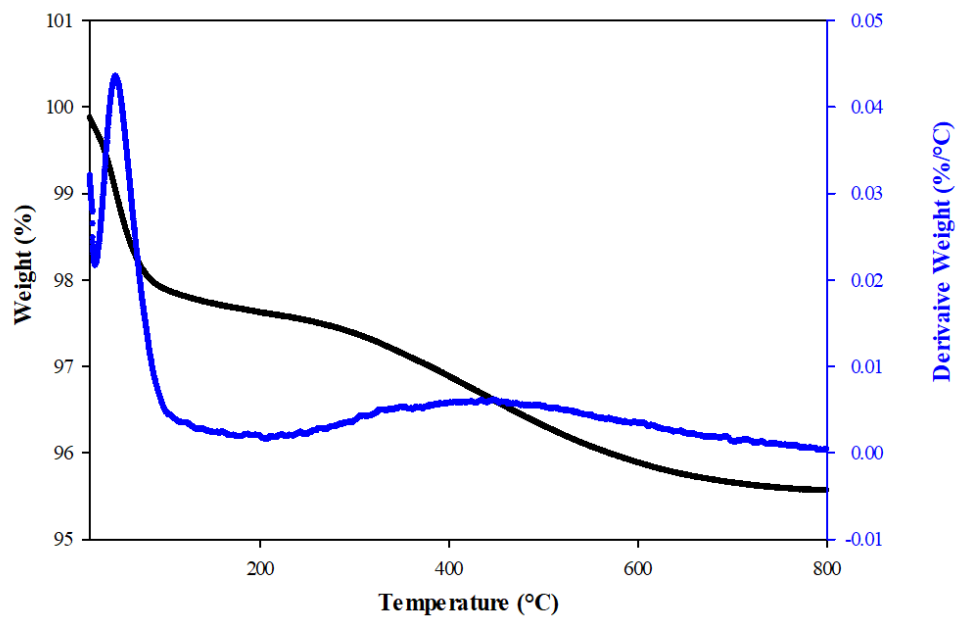


Figure A.3. TGA curves of weight % (black) and derivative weight (blue) for silica sample SA3

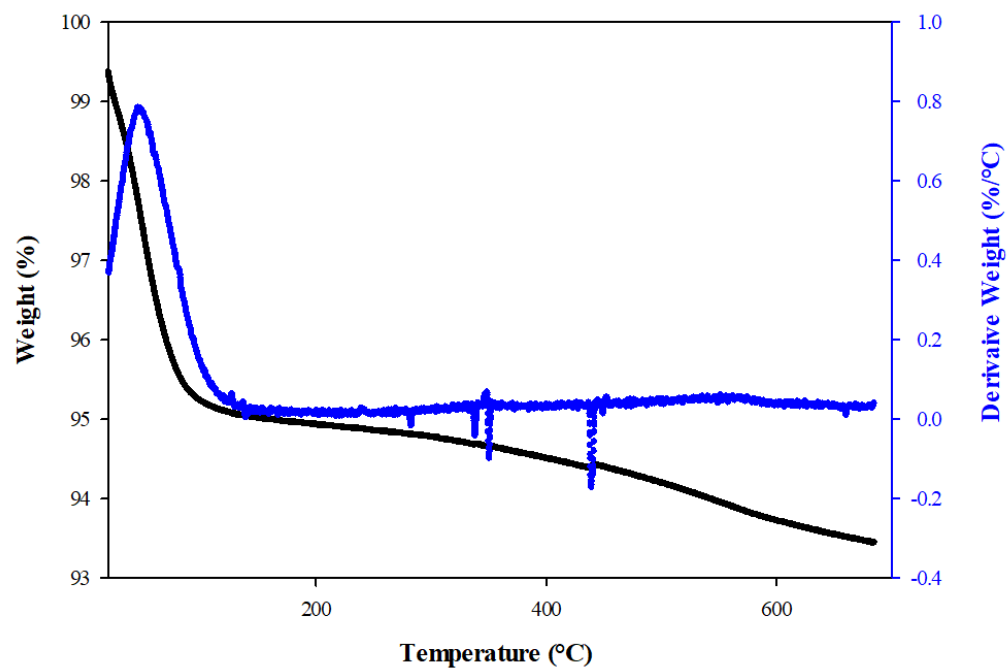


Figure A.4. TGA curves of weight % (black) and derivative weight (blue) for silica sample SA4

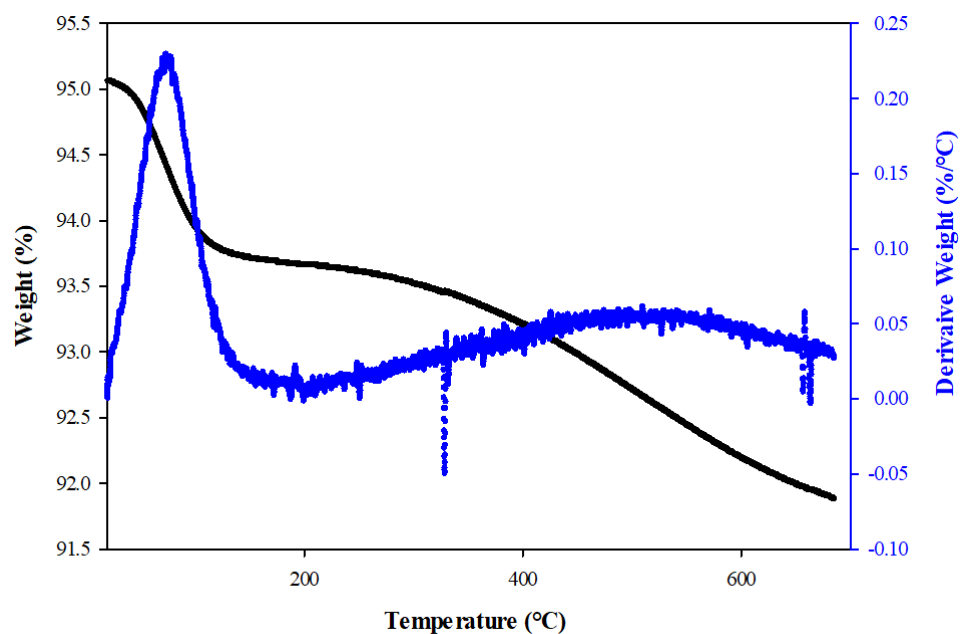


Figure A.5. TGA curves of weight % (black) and derivative weight (blue) for silica sample SA5

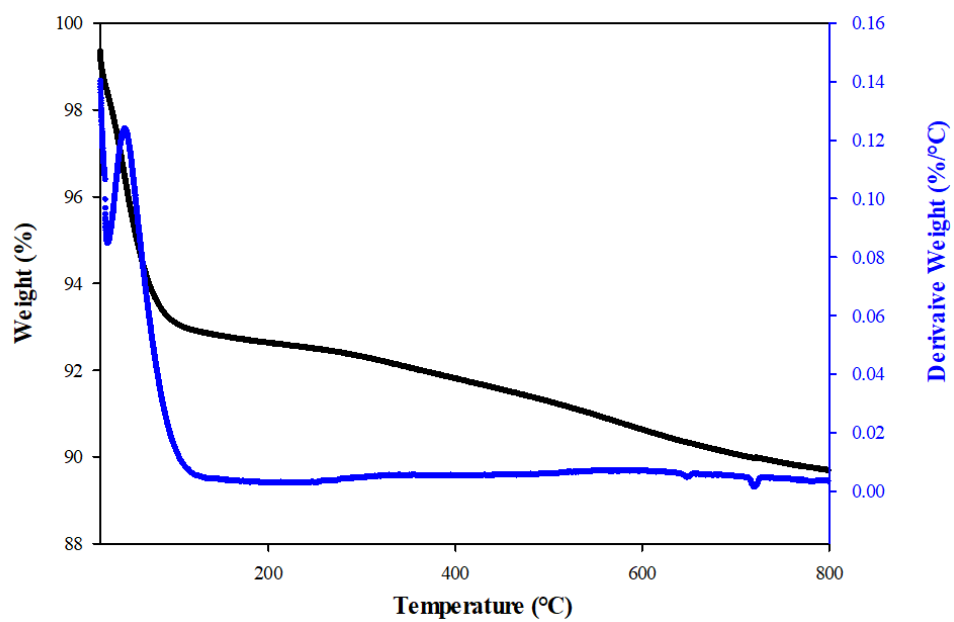


Figure A.6. TGA curves of weight % (black) and derivative weight (blue) for silica sample SA6

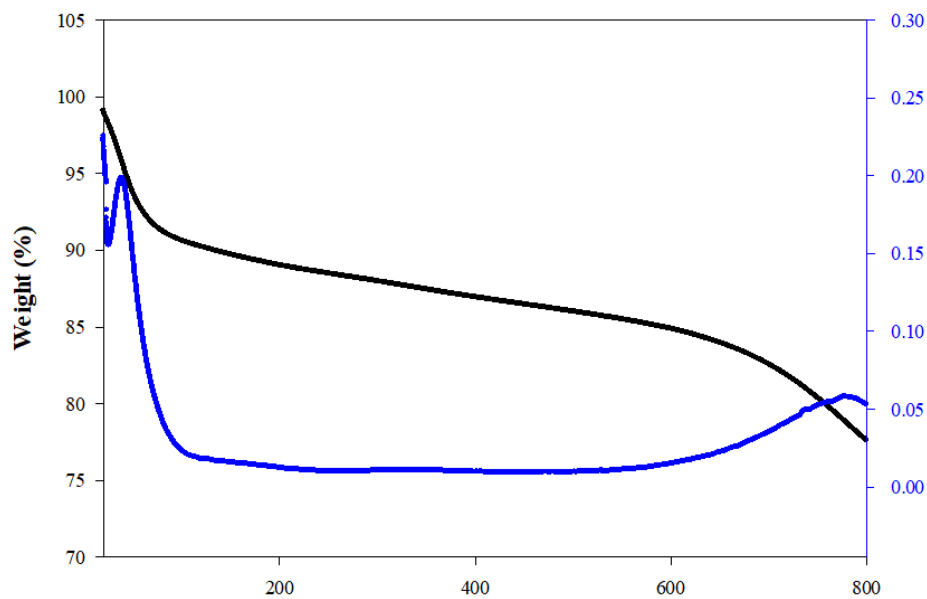


Figure A.7. TGA curves of weight % (black) and derivative weight (blue) for silica sample SA7

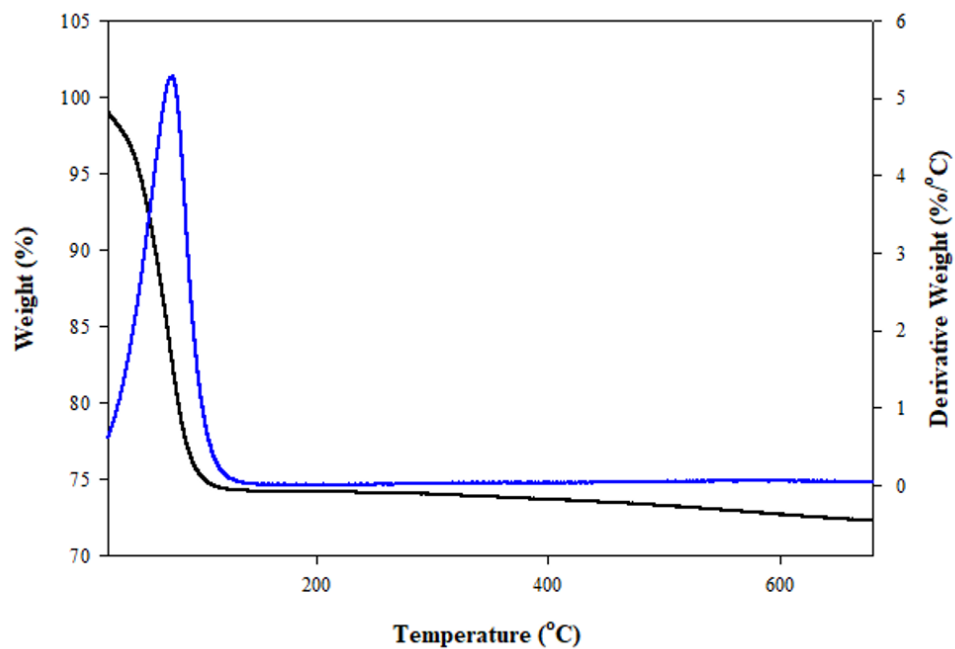


Figure A.8. TGA curves of weight % (black) and derivative weight (blue) for silica sample SA8

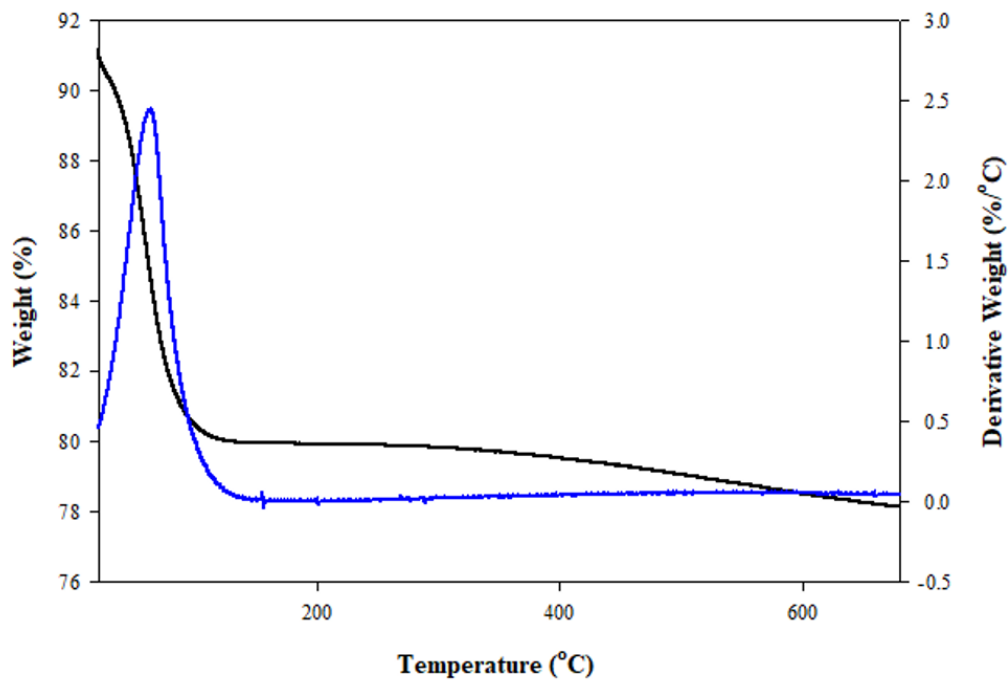


Figure A.9. TGA curves of weight % (black) and derivative weight (blue) for silica sample SA9

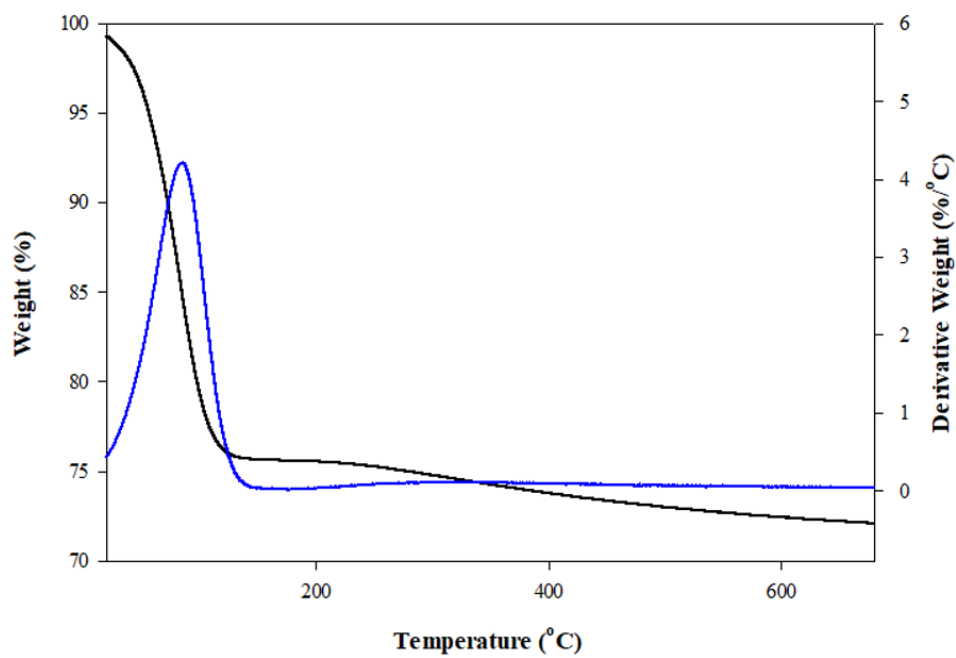


Figure A.10. TGA curves of weight % (black) and derivative weight (blue) for silica sample SA10

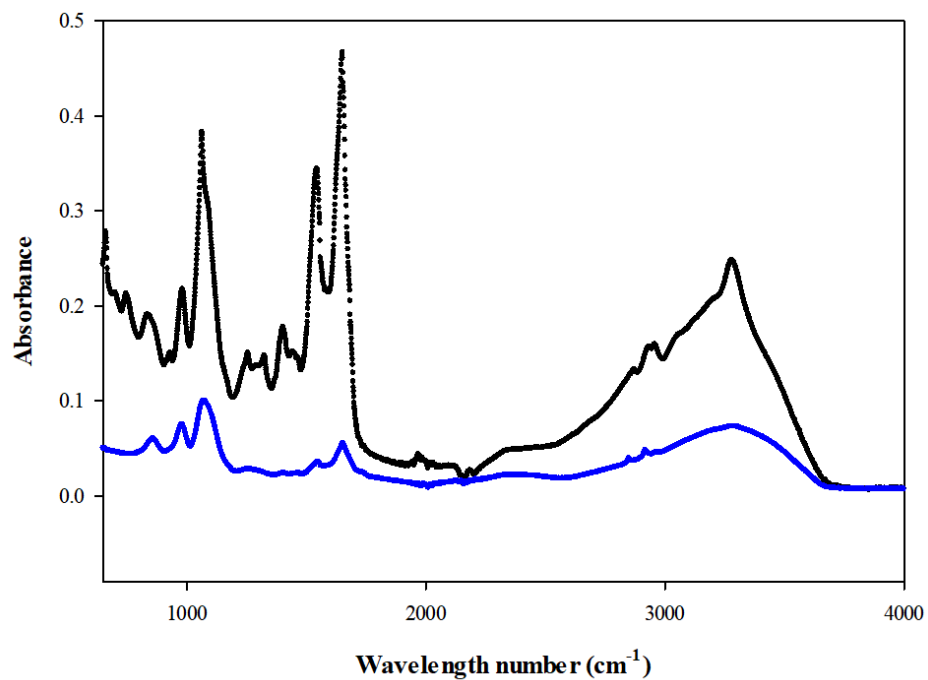
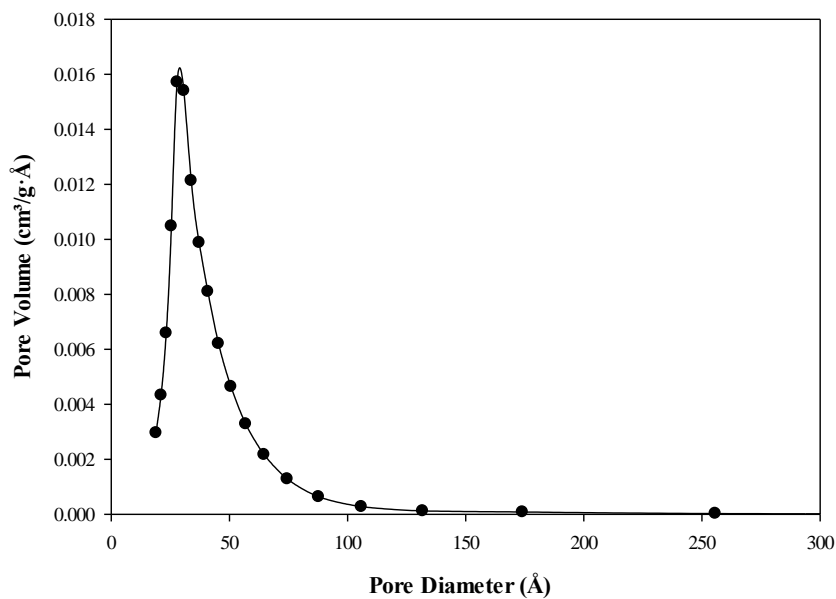
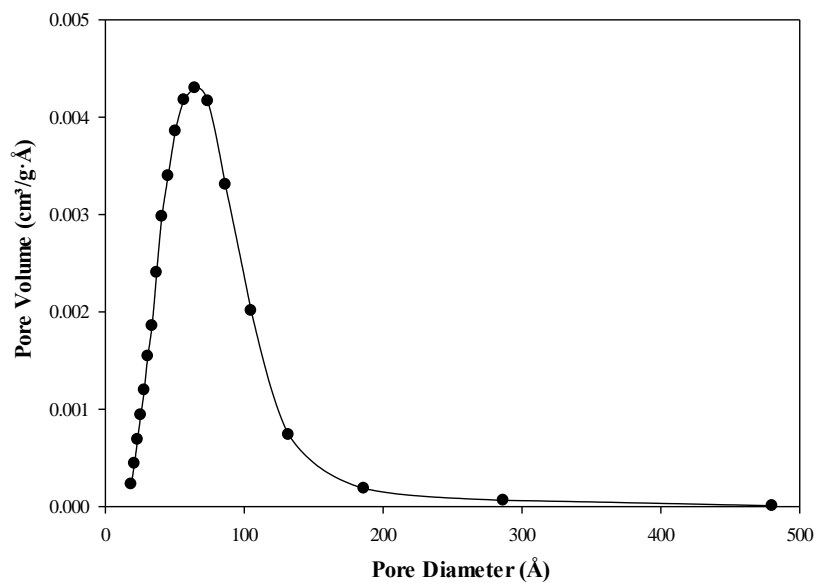


Figure A.11. FTIR spectra for IpaD dissolved in PBS (black) and PBS (blue). The most notable peak can be observed at 1653 cm⁻¹ corresponding to the alpha helix content in the protein.

Appendix B: Pore size distributions of silica samples**Figure B.1.** Pore size distribution for silica sample SA1**Figure B.2.** Pore size distribution for silica sample SA2

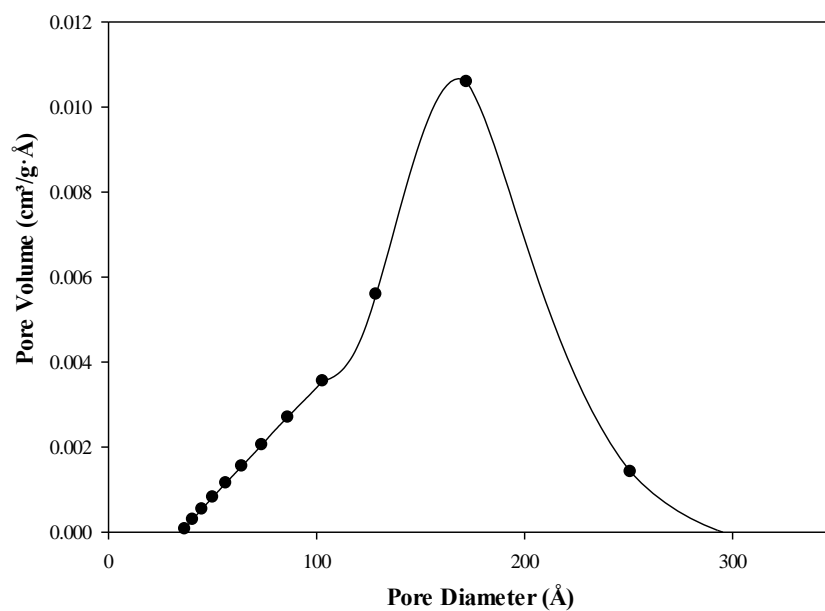


Figure B.3. Pore size distribution for silica sample SA3

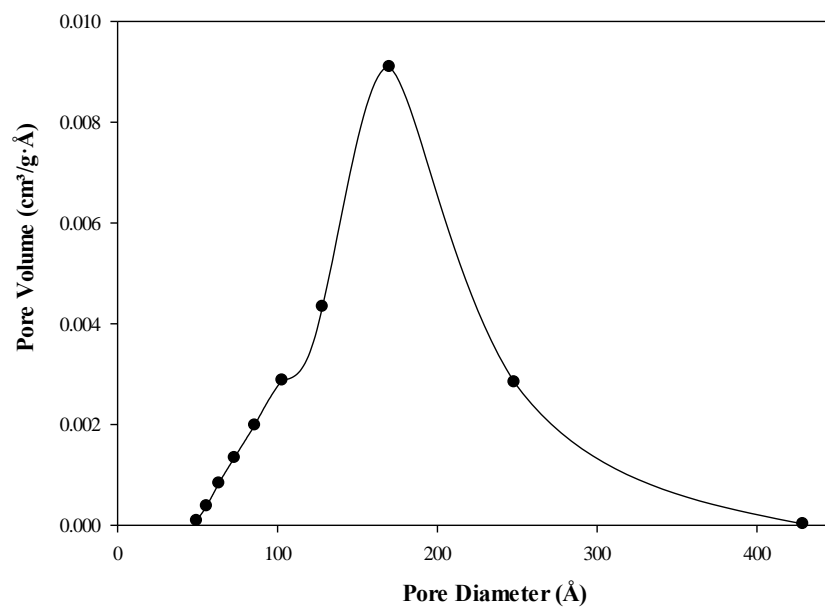


Figure B.4. Pore size distribution for silica sample SA4

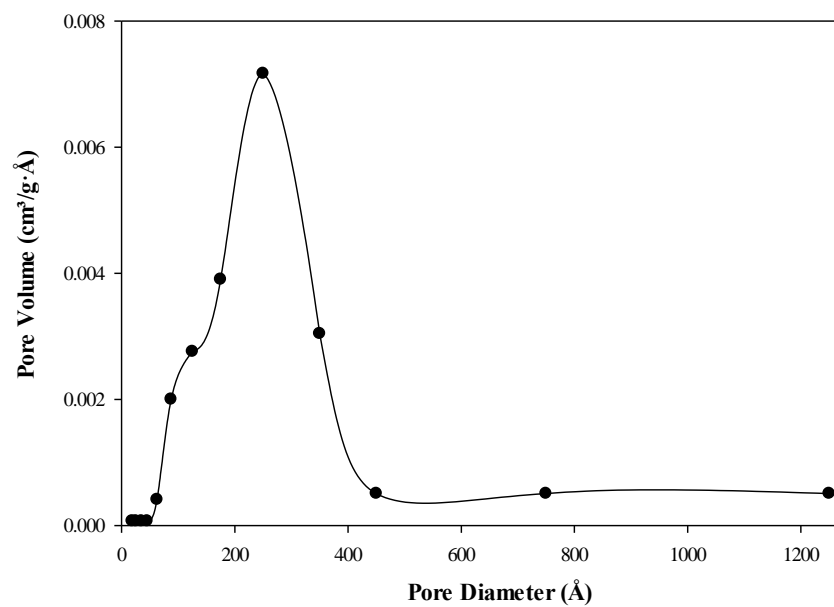


Figure B.5. Pore size distribution for silica sample SA5

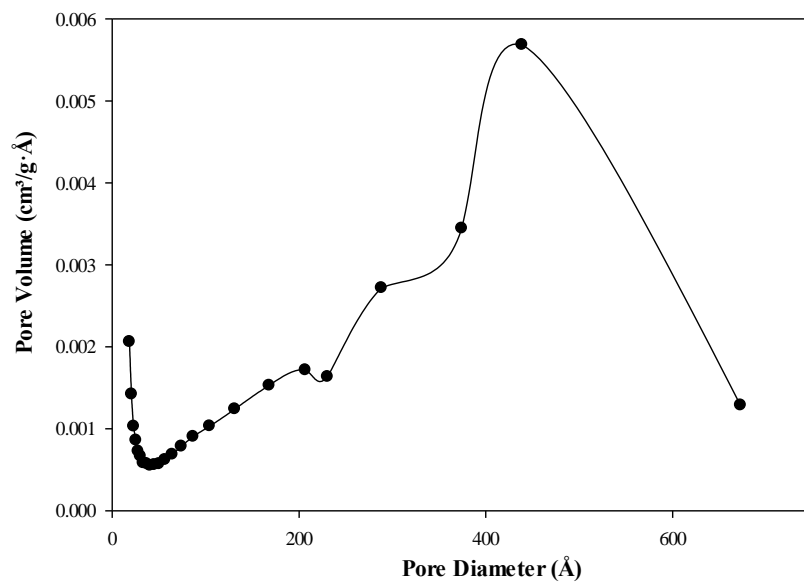


Figure B.6. Pore size distribution for silica sample SA6

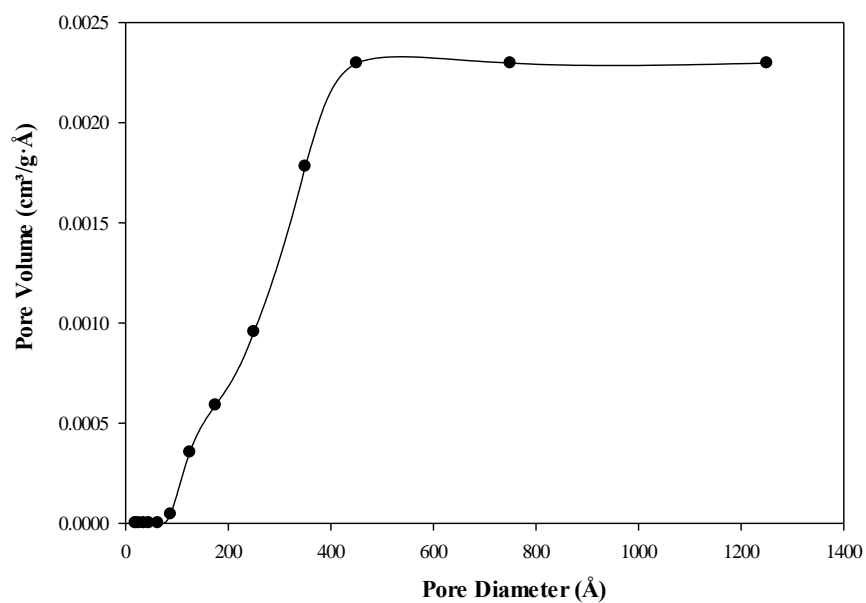


Figure B.7. Pore size distribution for silica sample SA7

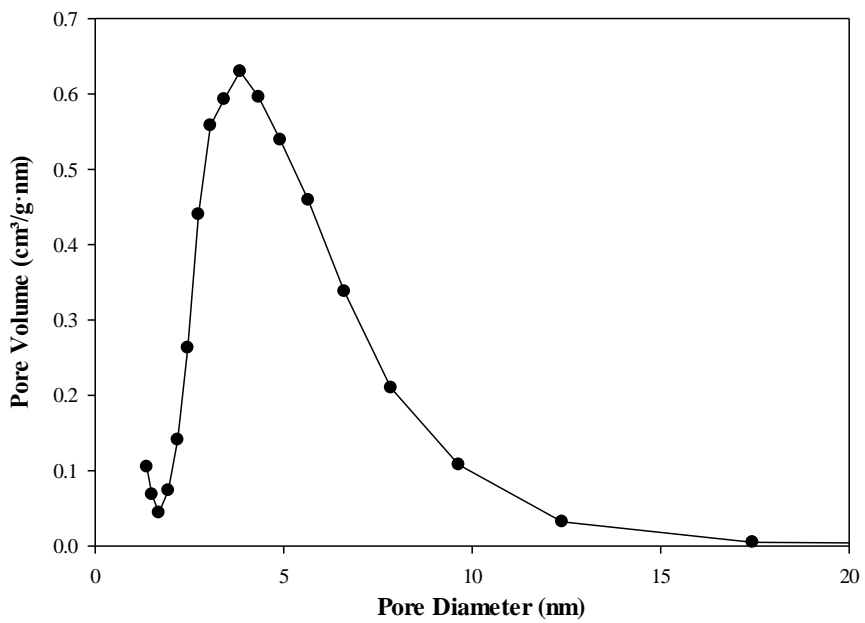


Figure B.8. Pore size distribution for silica sample SA8

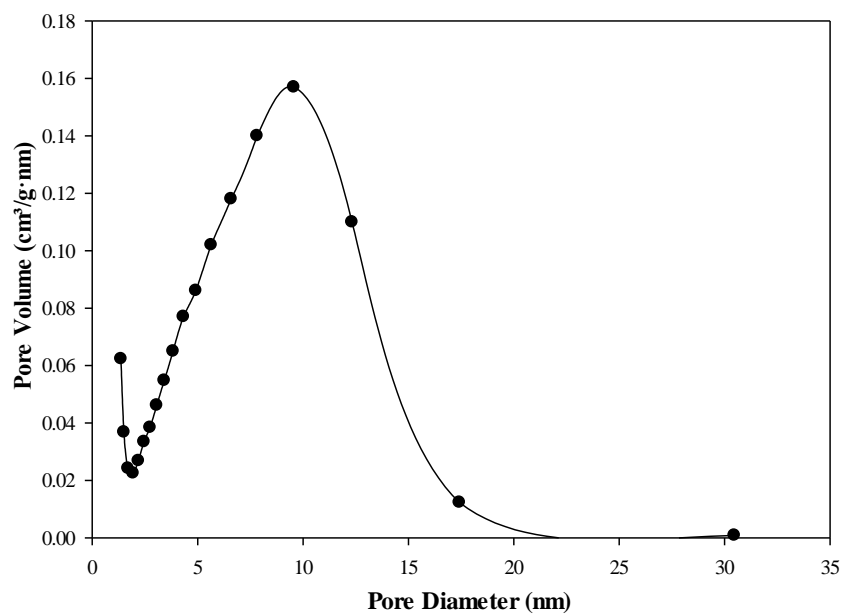


Figure B.9. Pore size distribution for silica sample SA9

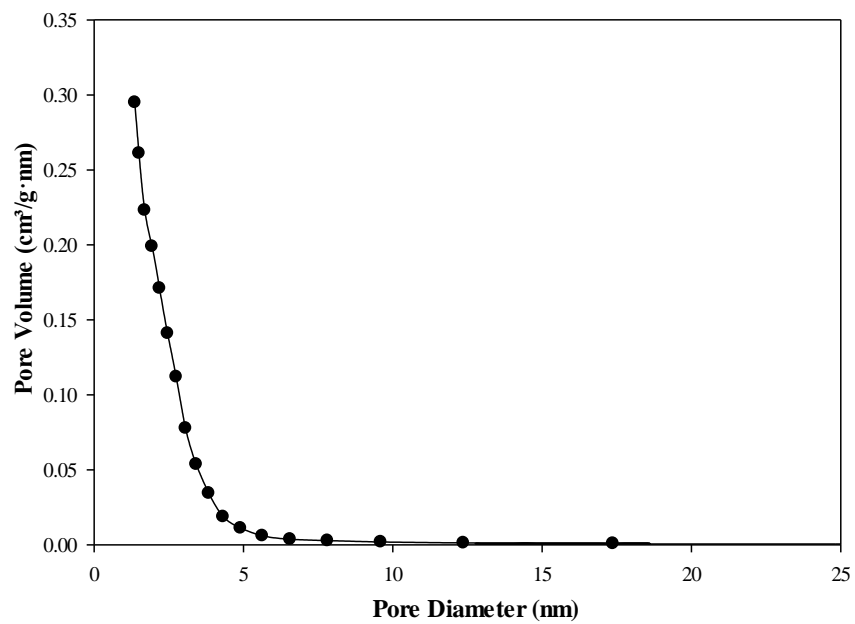


Figure B.10. Pore size distribution for silica sample SA10

Appendix C: Error Calculation on Adsorption Isotherms

The equation for adsorption capacity (q) can be written as:

$$q = \frac{c_i V \left(1 - \frac{c_f}{c_i}\right)}{s} \quad (\text{C.1})$$

Where

$$\text{Percent adsorption} = \left(1 - \frac{c_f}{c_i}\right) \times 100 \quad (\text{C.2})$$

Propagating the uncertainty for q:

$$U_q = \sqrt{\left(\frac{\delta q}{\delta s} U_s\right)^2 + \left(\frac{\delta q}{\delta c_i} U_{c_i}\right)^2 + \left(\frac{\delta q}{\delta V} U_V\right)^2 + \left(\frac{\delta q}{\delta c_f} U_{c_f}\right)^2} \quad (\text{C.3})$$

The partial derivatives are calculated as follows:

$$\frac{\delta q}{\delta s} = \frac{-c_i V (1 - c_f)}{s^2} \quad (\text{C.4})$$

$$\frac{\delta q}{\delta c_i} = \frac{V (1 - c_f)}{s} \quad (\text{C.5})$$

$$\frac{\delta q}{\delta V} = \frac{c_i (1 - c_f)}{s} \quad (\text{C.6})$$

$$\frac{\delta q}{\delta c_f} = -\frac{c_i V}{s} \quad (\text{C.7})$$

The errors for U_s and U_V are due exclusively to instrumental error of the Mettler Toledo scale which is equal to ± 0.0001 g. However, for U_{c_i} and U_{c_f} both random and systematic error are accounted for, including the random and systematic error in the blanks for these measurements.

Let U_x represent the random error, and U_y represent the systematic error. By definition of random error:

$$U_x = \frac{k_c SSD}{\sqrt{n}} \quad (\text{C.8})$$

Where SSD is the sample standard deviation and n is the number of points. The coverage factor k_c is calculated in excel:

$$k_c = T.INV.2T(0.05, DOF) \text{ for 95\% confidence} \quad (\text{C.9})$$

Where

$$DOF = n - \#of \text{ parameters} \quad (\text{C.10})$$

The nanodrop has a systemic error of:

$$U_y = 0.02C \quad (\text{C.11})$$

Where C refers to either C_i , C_f or C_B (blank). U_x and U_y were calculated for C_i , C_f and C_B .

$$U_{conc,C_i} = \sqrt{U_x^2 + U_y^2} \quad (\text{C.12})$$

$$U_{conc,C_f} = \sqrt{U_x^2 + U_y^2} \quad (\text{C.13})$$

$$U_{conc,C_B} = \sqrt{U_x^2 + U_y^2} \quad (\text{C.14})$$

Finally,

$$U_{C_i} = \sqrt{U_{conc,C_i}^2 + U_{conc,C_B}^2} \quad (\text{C.15})$$

$$U_{C_f} = \sqrt{U_{conc,C_f}^2 + U_{conc,C_B}^2} \quad (\text{C.16})$$

Appendix D: IpaD Adsorption Isotherms

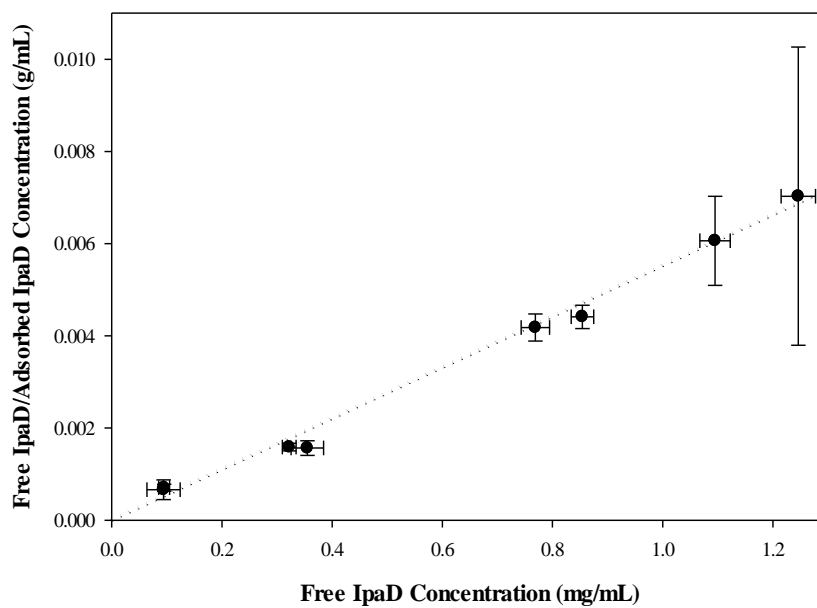


Figure D.1. Linearized adsorption isotherm for silica sample SA4 using the Langmuir model ($R^2=0.992$)

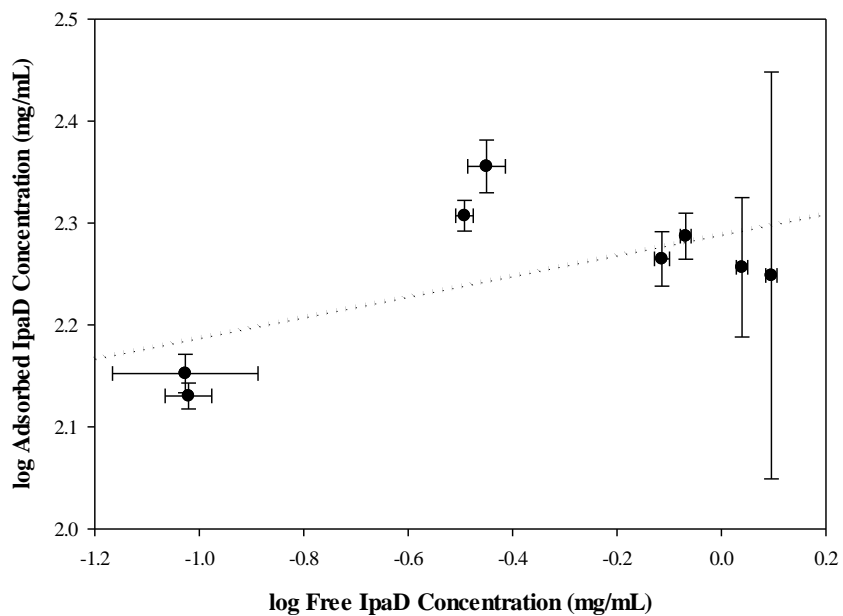


Figure D.2. Linearized isotherm for silica sample SA4 using the Freundlich Model ($R^2=0.365$)

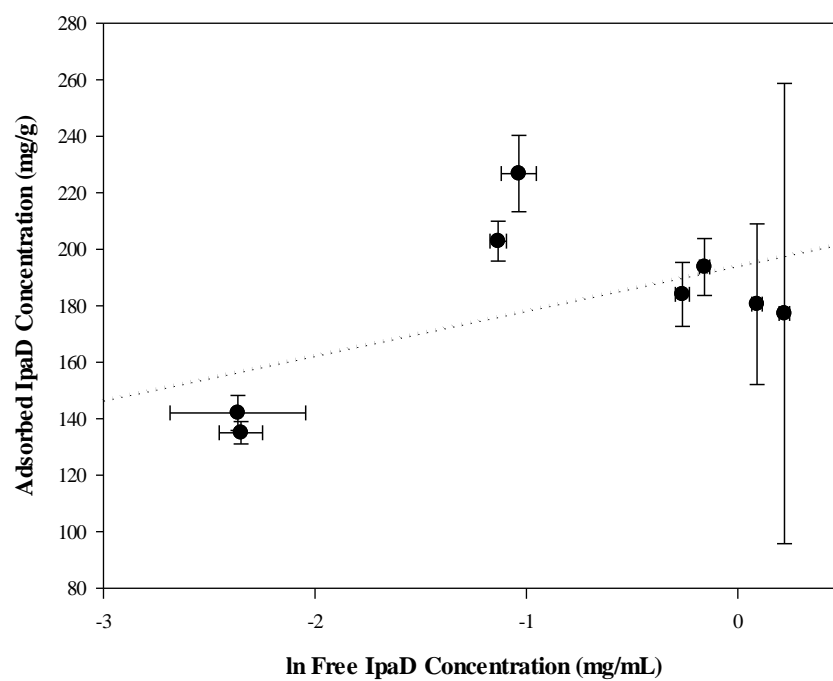


Figure D.3. Linearized isotherm for silica sample SA4 using the Temkin Model ($R^2=0.297$)

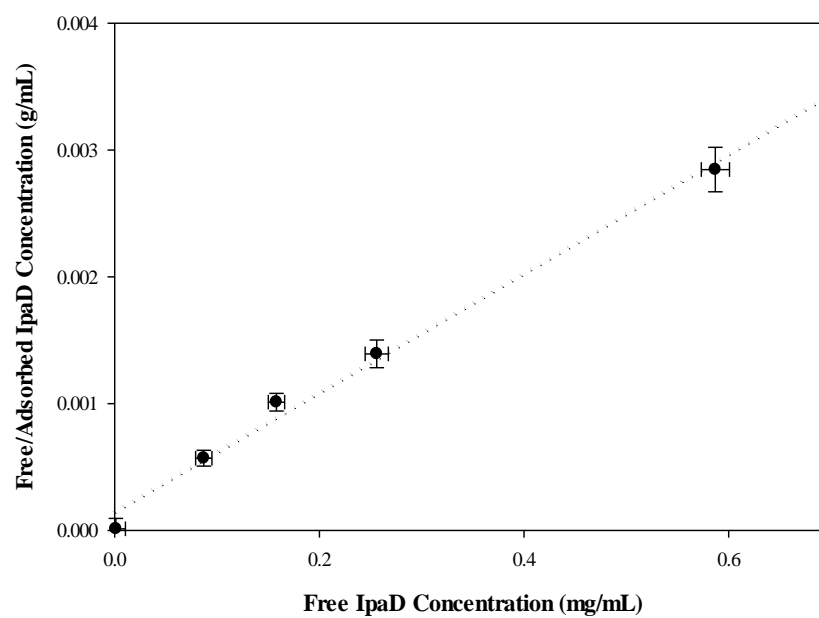


Figure D.4. Linearized adsorption isotherm for silica sample SA5 using the Langmuir model ($R^2=0.991$)

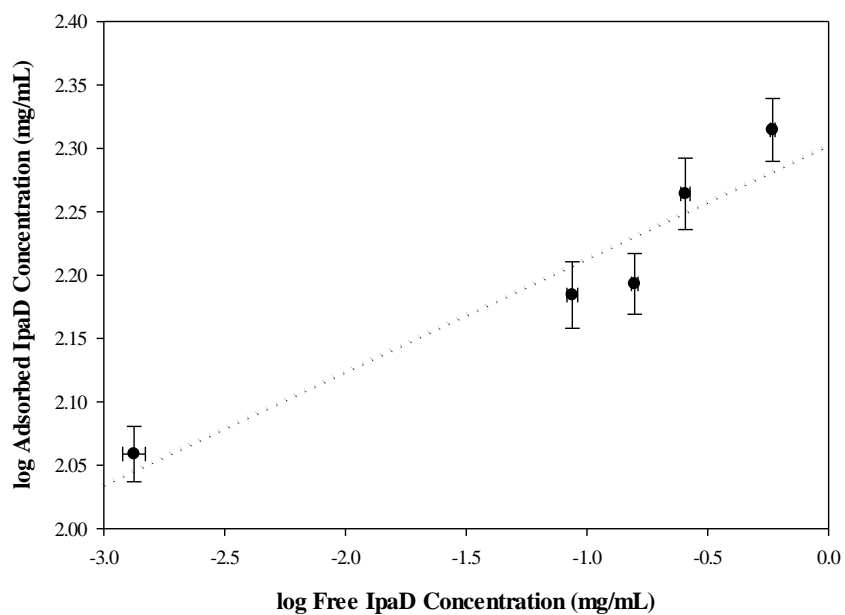


Figure D.5. Linearized isotherm for silica sample SA5 using the Freundlich Model ($R^2=0.908$)

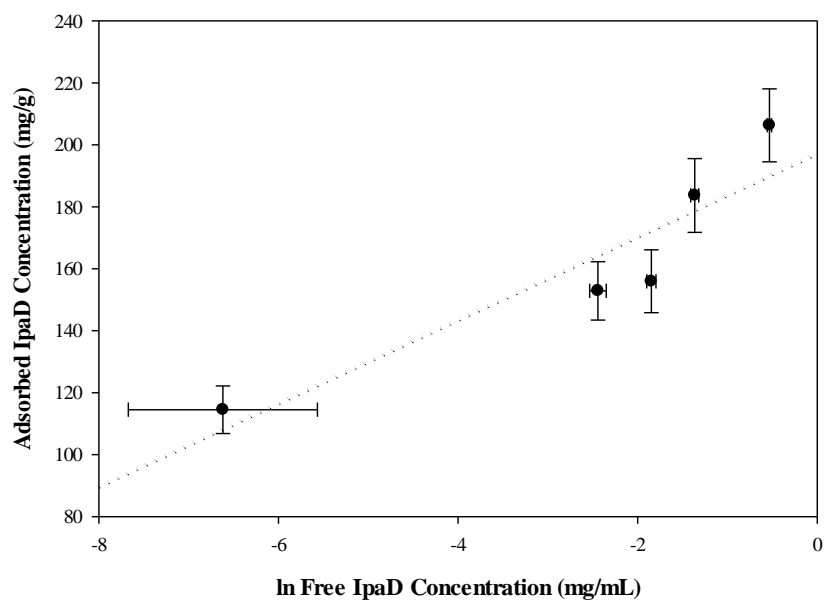


Figure D.6. Linearized isotherm for silica sample SA5 using the Temkin Model ($R^2=0.845$)

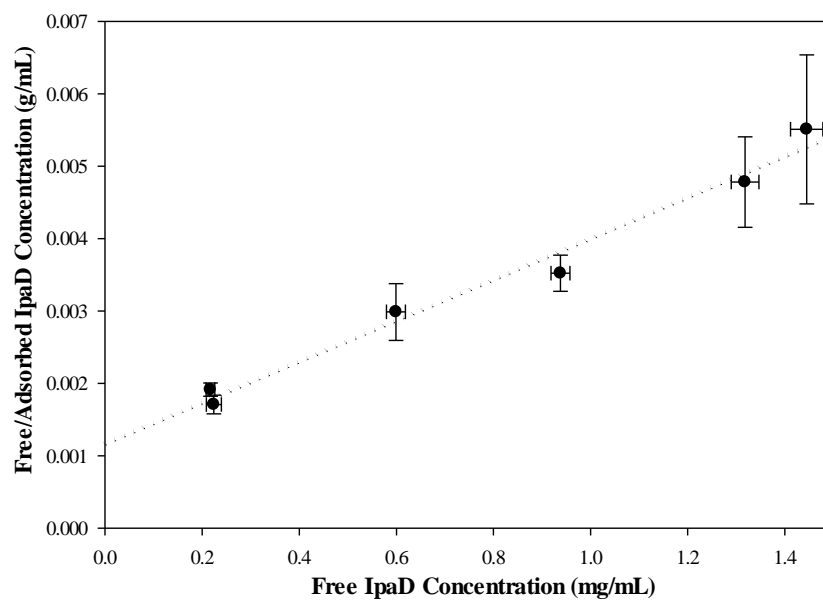


Figure D.7. Linearized adsorption isotherm for silica sample SA6 using the Langmuir model ($R^2=0.982$)

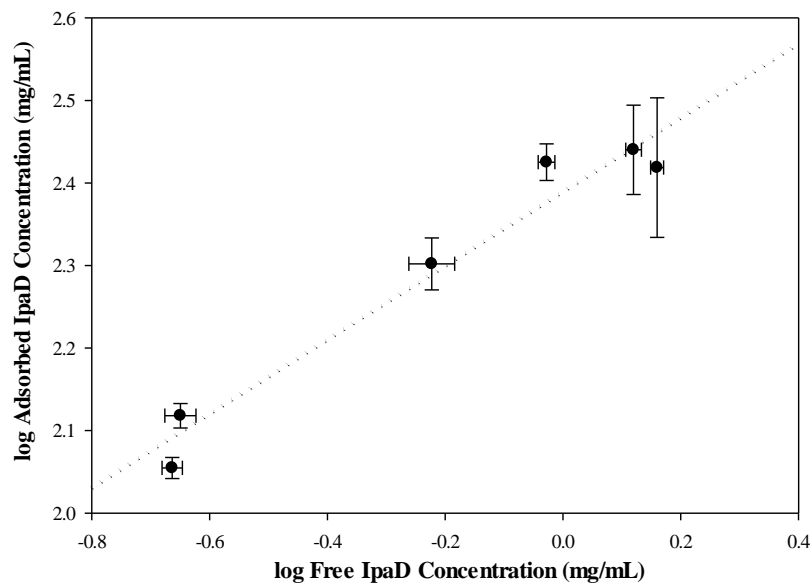


Figure D.8. Linearized isotherm for silica sample SA6 using the Freundlich Model ($R^2=0.975$)

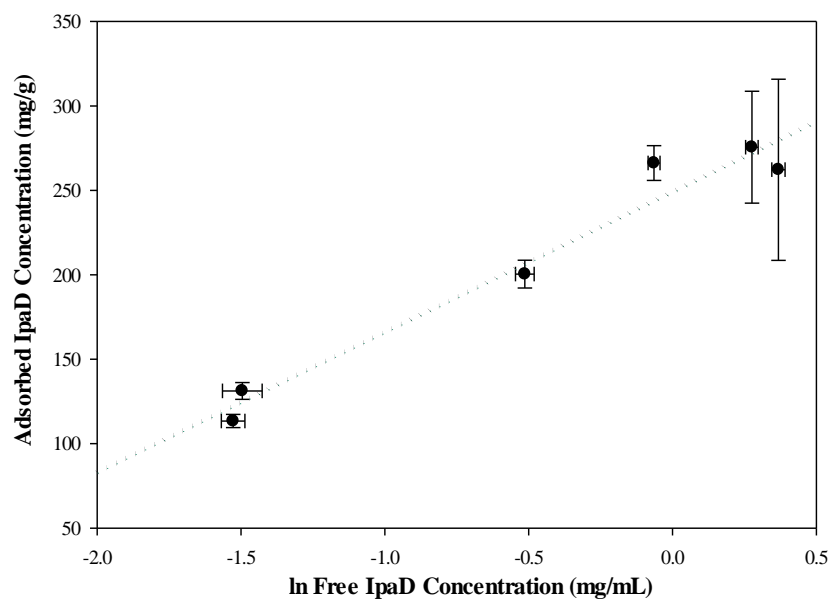


Figure D.9. Linearized isotherm for silica sample SA6 using the Temkin Model ($R^2=0.973$)

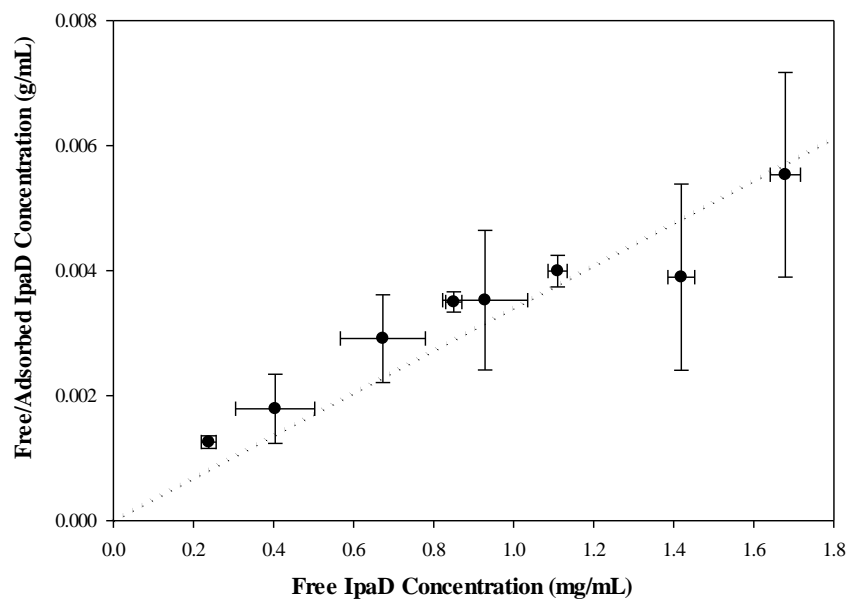


Figure D.10. Linearized adsorption isotherm for silica sample SA7 using the Langmuir model ($R^2=0.824$)

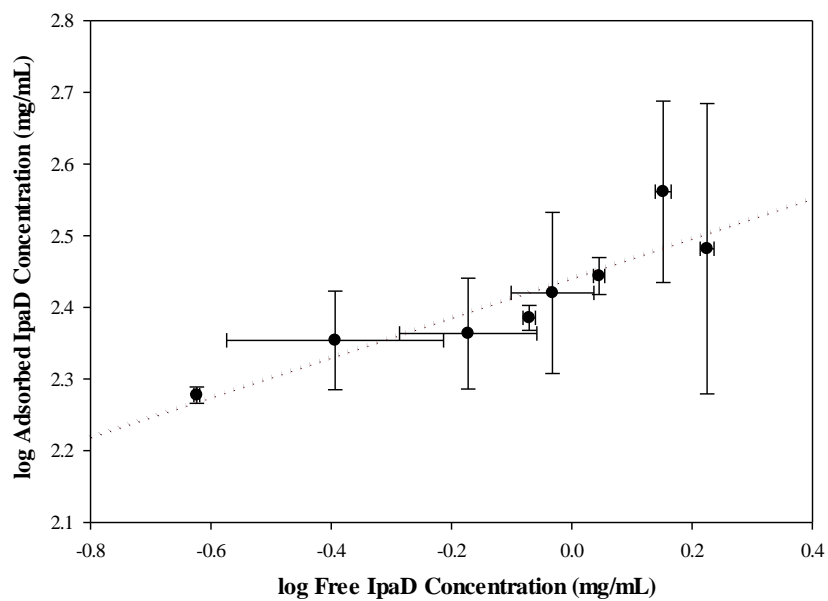


Figure D.11. Linearized isotherm for silica sample SA7 using the Freundlich Model ($R^2=0.821$)

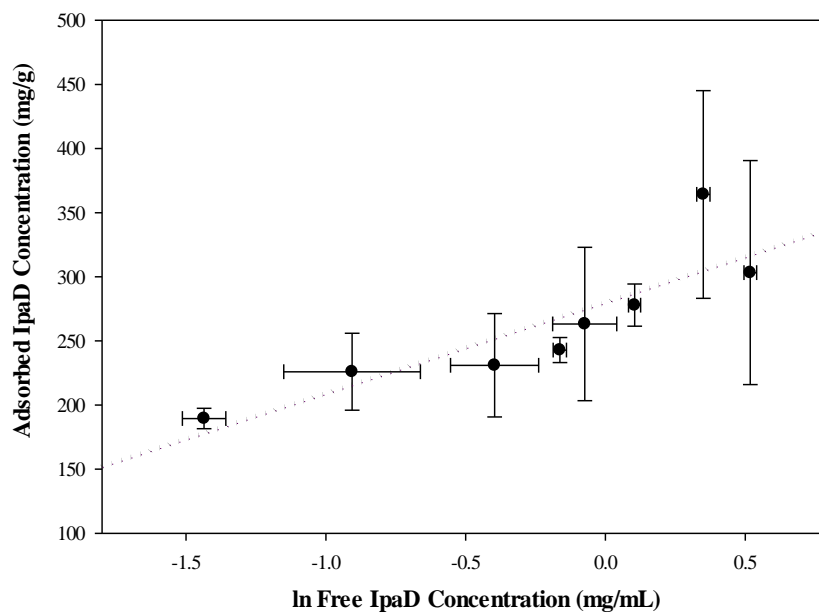


Figure D. 12. Linearized isotherm for silica sample SA7 using the Temkin Model ($R^2=0.750$)

Appendix E: Lf Adsorption Isotherms

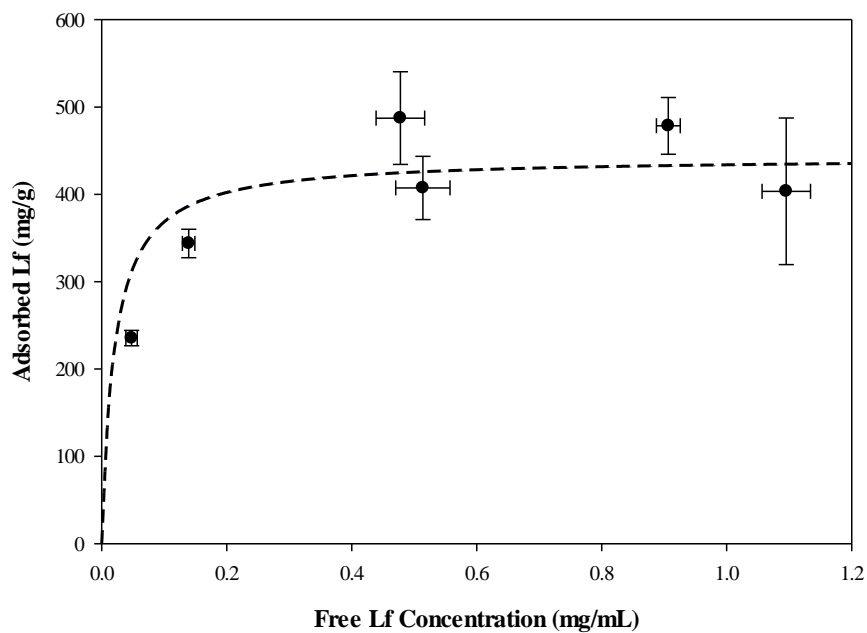


Figure E.1. Adsorption isotherm of Lf on silica SA7 using the Langmuir model

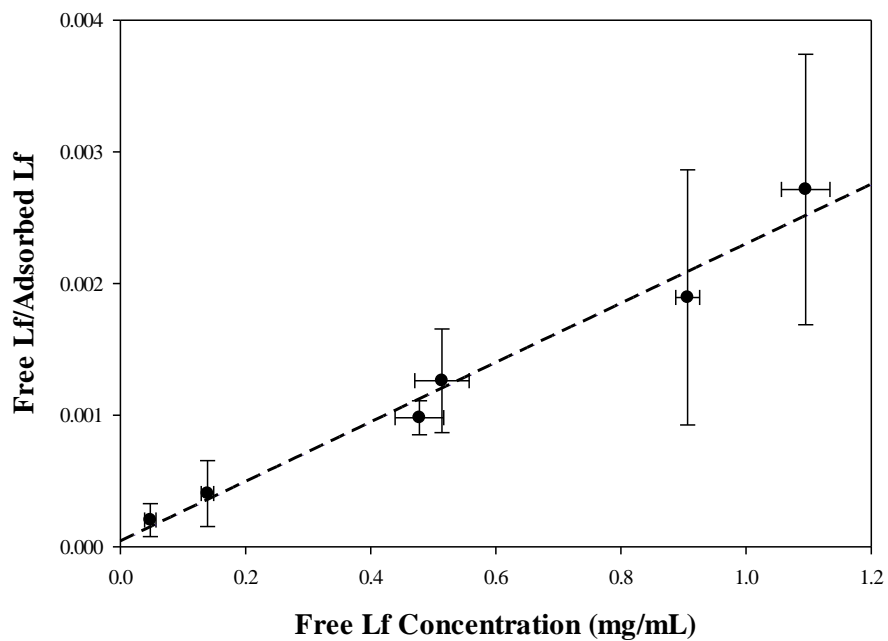


Figure E.2. Linearized adsorption isotherm for silica sample SA7 using the Langmuir model ($R^2=0.98$)